The Thesis Committee for Sandeep Kalyanapuram Krishnan
Certifies that this is the approved version of the following thesis:

Assessment of Numerical Differentiation Methods for Kinematic Orbit Solutions of the GRACE Mission

APPROVED BY

SUPERVISING COMMITTEE:

Supervisor: Srinivas V. Bettadpur

John C. Ries

Assessment of Numerical Differentiation Methods for Kinematic Orbit Solutions of the GRACE Mission

by

Sandeep Kalyanapuram Krishnan, B.S.As.E.

THESIS

Presented to the Faculty of the Graduate School of
The University of Texas at Austin
in Partial Fulfillment
of the Requirements
for the Degree of

MASTER OF SCIENCE IN ENGINEERING

THE UNIVERSITY OF TEXAS AT AUSTIN
December 2012

For my family...

Acknowledgments

First and foremost, I would like to thank Dr. Srinivas Bettadpur for serving as my advisor and Dr. Byron Tapley for allowing me the opportunity to become a graduate research assistant at the Center for Space Research. It has been a great opportunity and experience. I would also like to express my gratitude to Dr. John Ries for serving as my second reader. In addition, much of this work would not have been possible without the help of many of the other members of the CSR staff.

Next, I would like thank my fellow graduate students and friends, specifically my office-mates at CSR: Suyog Benegelrao, Alex Pini, Chris McCullough, and Carly Sakumura for their help and camaraderie. I wish you guys all the best in your future endeavors. Finally, I would not be anywhere today without the support of my entire family. To my father, mother, and sister, I appreciate all of your encouragement. I would especially like to thank my sister for helping me edit this report.

Assessment of Numerical Differentiation Methods for Kinematic Orbit Solutions of the GRACE Mission

by

Sandeep Kalyanapuram Krishnan, M.S.E.
The University of Texas at Austin, 2012
SUPERVISOR: Srinivas V. Bettadpur

The historical method of precise orbit determination is a dynamic approach. However, with the improvement of GPS tracking data and associated tracking networks, two newer methods have been developed: reduced-dynamic and kinematic. In addition to orbit determination, alternative methods of gravity field recovery have been developed using kinematic orbits which do not rely on any force modeling. However, one significant drawback of kinematic orbits is that they lack any velocity or acceleration information. These have to be derived numerically. Based on the results of this thesis, the Savitzky-Golay filter, without using a remove-restore procedure, is recommended for deriving kinematic velocities of the GRACE mission. In addition, the numerical differentiation methods are tested to see how well accurately they represent the satellite's acceleration for all three orbit types. Finally, with the kinematic orbits properly reconstructed, the results can also be compared to dynamic and reduced-dynamic orbits through K-Band Ranging residuals.

Table of Contents

List of Tables

List of Figures

Chapter 1

Introduction

1.1 Orbit Determination

1.1.1 Historical Background

Orbit determination (OD) is defined as computing an object's location in space and predicting its future motion. It has been an important topic for astronomers, mathematicians and physicists for centuries, who were concerned with the motion of celestial bodies. Kepler, Gauss, Legendre, Lagrange, and Newton contributed significantly to the development and the progress of orbit determination techniques using concepts of celestial mechanics. In 1957 the launch of the first artificial satellite, Sputnik I, shifted the focus to orbit determination of artificial satellites.

1.1.2 Definition

Satellite orbit determination problem is defined as computing the state vector, position and velocity vectors, of a satellite's center of mass at a specified epoch [1]. This is based on the ability to express a satellite's motion relative to the center of mass of a celestial body by a set of differential equations. Given the state vector at an initial time, the equations of motion can be integrated to determine the state of the satellite at any other time. However, errors accu-

mulate due to mismodeling, computational limits, and numerical integration methods (i.e., round-off and truncation errors). These errors cause the actual motion to deviate from the predicted motion. Therefore, the satellite must be tracked or observed from tracking stations. With these observations of the actual motion, a better estimate of the trajectory can be determined through the method of differential corrections. The exact trajectory can never be known known since any observation will be subject to errors.

The process of observation and estimation must be repeated continuously as the satellite's motion evolves. Since a satellite's orbit is complicated and constantly changing, a large number of observations are used to determine the orbit. Such problems are over-determined in that they utilize more observations than the number required. Over the years, the invention of the digital computer and new algorithms have enabled numerical approaches to solve these problems.

The focus of this study is on the precise orbit determination (POD) of Low Earth Orbit (LEO) satellites, with particular reference to applications in geodetic research such as gravity field recovery. It should be noted that only the translational motion of the artificial satellite is of importance in this context; the rotational motion of the satellites is outside the scope of this thesis.

1.1.3 Modern Precise Orbit Determination

There are many applications for precise orbit determination. They are needed for geolocation of remote sensing observations, precise metrology (i.e., radar or laser altimetry), and trajectory analysis, where perturbations can be used for gravity field determination. During the past two decades numerous LEO satellite have been launched for scientific purposes at altitudes ranging from 400 km to 1300 km. These missions have benefited from on-board space-grade Global Positioning System (GPS) receivers, and the measurements obtained from GPS satellites are used as observations for POD. GPS receivers are now considered the primary tracking system for orbit determination in many satellite missions where precise orbits are required. The benefits of GPS, such as 3-dimensional position and timing accuracy, coverage, and availability of GPS measurements, make it more preferable than other tracking systems such as Doppler-based methods (i.e., DORIS and TDRS) and Satellite Laser Ranging (SLR) for LEO applications. To meet the science objectives of these missions, POD must be guaranteed, though the required accuracy may vary for different applications.

There are three main processing strategies for orbit determination: 1) dynamic, 2) kinematic and 3) reduced-dynamic. The kinematic and reduced-dynamic approaches have been developed to utilize GPS tracking and were validated on TOPEX/Poseidon, which was the first mission to demonstrate the ability of GPS to determine and track a spacecraft's location [2]. The primary POD technique for satellites in medium to high Earth orbits is the dynamic

approach. Typically, the altitudes of these satellites range from 6,000 to 20,000 km. Their orbits are smooth enough to use only low degree/order harmonics to model gravitational effects; moreover, the atmospheric drag effect is negligible at these altitudes. But in the LEO case the kinematic, dynamic, and reduced-dynamic methods are used. In general, no method is clearly superior for all cases. On the one hand, the quality of space borne GPS receivers has improved considerably, but on the other hand there has been significant progress in the modeling aspects of POD.

In dynamic POD, all forces acting on the satellite are computed and numerically integrated to estimate the initial state vector and other unknown dynamic parameters. This technique has been applied to many successful satellite missions and has become the mainstream POD approach. The limitations of this technique are dynamic model errors such as inaccurate representations of the geopotential or atmospheric drag [3]. Thus, accurate force modeling is a critical and complicated issue with this method. With the continuous, high precision GPS tracking data, dynamic model parameters, such as geopotential parameters, can be estimated in addition to the satellite's state. The dense tracking data also allows for the frequent estimation of empirical parameters which help reduce the effect of unmodeled or mismodeled dynamic forces. Other tracking system measurements, such as those from SLR and DORIS, are restricted to a dynamic OD strategy because of their discontinuous tracking and one-dimensional observability [2].

The kinematic approach is a geometric method based on the Precise

Point Positioning (PPP) GPS data processing technique. For LEO applications, it relies on an initial nominal dynamic or reduced-dynamic orbit as well as post-processed precise orbits and clocks for the GPS constellation. PPP combines results from a single receiver with location and and time information from satellites and clocks to compute a position fix [4]. The kinematic method uses only GPS measurements to determine a time series of positions of the satellite on an epoch-by-epoch basis. This process is independent of the satellite's altitude or background force model. The orbit quality is strongly dependent on the GPS signal quality (i.e., geometry and continuity). Kinematic solutions are more sensitive to geometrical factors, such as the direction of the GPS satellites and the GPS orbit accuracy [3]. Since there is no connection between adjacent position estimates, there is no direct information about the satellite's velocity or acceleration. The derivation of accurate kinematic velocities and accelerations is a main topic in this study and is discussed in detail in later chapters.

Finally, the reduced-dynamic approach uses both geometric and dynamic information and weighs their relative strength. It introduces kinematic components to the dynamic force models by estimating empirical accelerations in the form of process noise parameters. Dynamic parameters are estimated first, then the state vector is re-estimated along with the stochastic process noise, which is usually modeled as a first order Gauss-Markov process [5]. The process noise model absorbs dynamic modeling errors.

1.2 Gravity Field Recovery

1.2.1 Historical Background

A common approximation for the Earth is a perfectly round sphere of uniform density. This would produce a gravitational field of uniform magnitude at all points on its surface. However, as Isaac Newton first proposed, the Earth is actually an oblate spheroid, with a significant bulge at the equator and flattened at the poles. In addition, the Earth is not a perfectly oblate spheroid, because mass is distributed unevenly within the planet. Its shape, orientation, and mass distribution shift due to perturbing effects. Some of these effects include the movement of tectonic plates, bodies of water, the atmosphere, ice sheets, and solid-body tides. Therefore, scientists realized that by gaining a better understanding of the Earth's gravity field they could gain a better understanding of these physical processes as well.

Terrestrial measurements were the basis for the understanding and the knowledge of gravity until the late 1960s. However, the lack of spatial coverage and homogeneity significantly affected the accuracy of these gravity field models. The launch of Sputnik changed the field of orbit determination by introducing satellite tracking data as a means of improving gravity field models. This idea is based on the non-uniformity of the Earth's gravity field perturbing the motion of an orbiting satellite. Therefore, by accurately measuring the position of the satellite as it flies over the Earth's surface, the gravitational forces acting on the satellite can be estimated.

A gravity model refers to a set of coefficients of the orthogonal basis

functions that approximate the shape of the Earth's gravity field. These coefficients are those of the Legendre polynomial and trigonometric functions in a spherical harmonic expansion that describes the three dimensional surface potential above the Earth.

There are several noteworthy gravity models that have been developed over the years. The size of the gravity fields, which are determined by the number of coefficients in the model, have increased over time based on the improvements in observation data and computational methods. NASA/GSFC (Goddard Space Flight Center) developed the earliest, widely used series of gravity models called Goddard Earth Model (GEM). These were derived from laser range data, Doppler range data, satellite radar altimetry and surface gravity data [6]. This series was followed by the Joint Gravity Model (JGM), which was created by NASA/GSFC in conjunction with The University of Texas at Austin/Center for Space Research (UT/CSR). In addition, UT/CSR independently developed a series of gravity field models called Texas Earth Gravity (TEG). TEG-3, complete to degree and order 70, was released in 1997. It was the first model to include GPS data which came from the receiver on-board TOPEX/Poseidon [7].

Satellite tracking greatly improved gravity models by using data from the orbits of many different satellites, with different inclinations, over a long period of time. However, none of these satellites were designed for gravity field recovery. Nearly all of the satellites used for these early models had orbits with an inclination that was less than 70 degrees, leaving the poles untreated and

not providing the global coverage needed [8]. In addition, other limitations of these early models include the altitude of the satellites, observation coverage, and uncertainties in the surface force models. While data coverage improved due to the development of GPS, the other limitations remained. The solutions derived from satellite tracking data cover spatial scales from 500 to 40000 km. However, they were reliable only down to a resolution of about 1000 to 1500 km. This is the main reason why it was combined with surface gravimetric and altimetric data. Depending on the coverage area, this resulted in higher resolution, but not necessarily higher precision. These combined models, e.g. EGM-96, reached 50 km resolution, but only over areas with enough surface data. [9]

1.2.2 Gravity Mapping Missions

It was for these and related reasons that scientists proposed launching dedicated gravity field recovery missions that make use of the satellite-to-satellite tracking (SST) or satellite gravity gradiometry (SGG) concepts. The basic notion behind the SST approach is to accurately measure the range between two orbiting satellites. By doing so, many of the observability problems of the single satellite configuration are resolved, and a much higher resolution gravity field model can be obtained. The SGG method relies on a single satellite measuring the Earth's gravity gradient, i.e. small variations in the gravitational acceleration, using a gradiometer. Three dedicated gravity recovery missions were launched within the past fifteen years. Each of these missions

were designed to observe different regions of the gravity signal spectrum using variations of the SST and SGG concepts.

The first mission was CHAllenging Minisatellite Payload (CHAMP), which launched in July of 2000. The satellite entered into an almost circular, near polar orbit with an initial altitude of 454 km. The design lifetime of the satellite system was 5 years, though it completed an extended mission and re-entered the Earth's atmosphere in September 2010. In order to estimate gravity field parameters, it was equipped with a space-grade GPS receiver enabling high-low Satellite-to-Satellite Tracking (hl-SST). The attitude and the non-gravitational accelerations are measured by a star camera and a three-axis accelerometer, respectively. Because hl-SST data is sensitive to long and medium wavelength (below degree 60-70) gravity field perturbations, CHAMP significantly improved the accuracy of the gravity field models at these wavelengths. Nevertheless, CHAMP was not able to accurately retrieve the time-variable gravity field.

The second mission is the Gravity Recovery and Climate Experiment (GRACE) which will be discussed in detail in the next section.

The last of these three missions, the Gravity Field and steady-state Ocean Circulation Explorer (GOCE), launched in March 2009. GOCE flies at an extremely low orbit altitude of 250 km. It is dedicated to modeling the Earth's static gravity field and geoid with high accuracy and spatial resolution measurements taken using SGG. The SGG system consists of three pairs of highly sensitive accelerometers centered at the satellite's center of mass. Thus,

the gradients of gravitational accelerations in all three spatial directions are measured, which can be used to derive all the elements of the matrix of second derivatives of the gravitational potential. The purpose of GOCE is to measure gravity signals at shorter spatial scales and detect fine density differences in the crust and oceans of the Earth. Since GOCE is at such a low altitude, it is equipped with a drag-free control system to compensate atmospheric drag and other non-gravitational forces. It also carries a high-quality GPS receiver to provide accurate hl-SST data.

1.3 GRACE Mission

The GRACE mission was launched in March 2002. It is a joint mission by NASA and the German Aerospace Center, DLR. Dr. Byron Tapley of UT/CSR is the Principal Investigator, and Dr. Christoph Reigber of GeoForschungsZentrum (GFZ) was the original Co-Principal Investigator of the mission. Project management and systems engineering activities are carried out by the Jet Propulsion Laboratory (JPL). The ground based tracking and operations of GRACE is handled by the German Space Operations Center (GSOC) with the observation data processed by JPL, UT/CSR and GFZ.

The mission consists of two co-orbiting satellites in a near polar and near circular orbits separated by an along track distance around 220 km. The satellites were injected in the orbit at the altitude of about 500 km. The primary goal of GRACE is to obtain accurate global models for the mean and time variable portions of the Earth's gravity field. As the satellites move over

an area with an anomalous mass concentration, they are first pulled forward as they approach the mass anomaly, then backwards as they pass it. The 220 km separation means that the two satellites accelerate and decelerate at different times, leading to a change in the inter-satellite range. Thus, the gravity signal of that mass anomaly is captured in this signal.

The fundamental measurement for gravity recovery is the inter-satellite range change, which is provided by a K-Band Ranging system (KBR) that determines the change in the range to a precision of a few microns. In order to measure this range and its derivatives precisely, the GRACE satellites use a dual one-way microwave ranging system. Identical transmission and reception sub-systems are present on each satellite and transmit the carrier signal to the other satellite. The received signals of both the satellites are down-linked to the ground stations and then combined. To maximize the data quality, the satellite attitudes are maintained so that the K-Band antennas are continuously pointed at each other. This requires precise attitude control and a one degree pitch on both satellites at the nominal 220 km separation. The attitude is determined with two star cameras on each satellite, and controlled by cold gas thrusters and magnetorquer rods. Each GRACE satellite carries a BlackJack receiver on-board to enable POD. The BlackJack receiver is an advanced code-less, dual-frequency flight GPS receiver developed by JPL [10]. These receivers have up to 16 channels: up to 12 for POD and the remaining 4 for occultation measurements. The average number of GPS satellites actually tracked is usually about 10. Non-gravitational affects, such as drag and other

surface forces, are measured with a SuperSTAR accelerometer. The general concept of GRACE is illustrated in Figure 1.1. [10],[11]

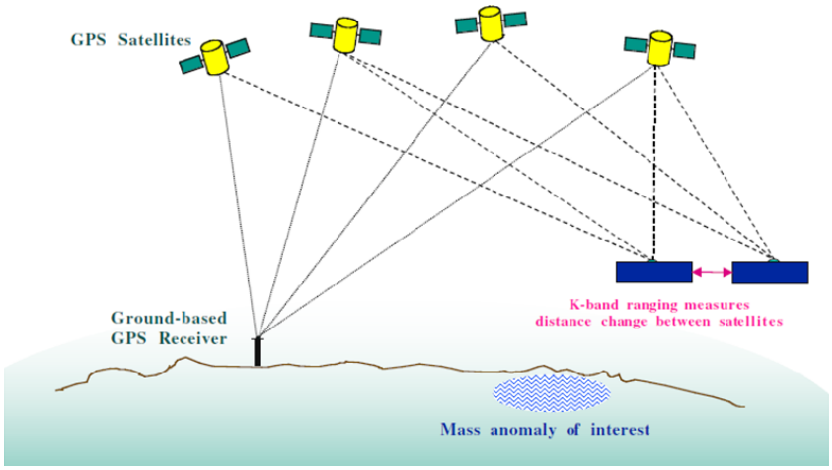

Figure 1.1: GRACE Mission Concept [Image Courtesy of CSR]

The determination of gravity from the satellite range changes is an iterative process of improving an existing gravity field model. The range changes measured by GRACE are due to variations in the gravity, plus the effect of other forces on each of the satellites like drag, radiation pressure and thruster firings. The expected range changes are predicted using the current best gravity model and measurements of the non-gravitational forces from the SuperSTAR accelerometer. In principle, if the non-gravitational forces from the accelerometer are accurately measured on the satellite, then the residuals between the measured and the predicted range changes will only be due to the omissions and errors in the initial gravity field model. These residuals can be used for differential corrections of the gravity model. Two forms of the grav-

ity models are created, a long-term mean field and a short-term time variable field.

Since both the gravity field and orbits are simultaneously estimated, the orbit determination accuracy was not specified as an *a priori* requirement for GRACE, but rather as a guideline for subsystem design. This requirement states that orbit error for each satellite relative to an Earth fixed frame is 10 mm in orbit plane (including radial and along-track components) and 50 mm perpendicular to orbit plane (cross-track) in the root mean square sense [12].

GRACE has increased the accuracy of the estimate of the Earth's gravitational potential model to unprecedented levels. The monthly gravity models generated by GRACE are up to 1,000 time more accurate at the longer wavelengths than existing solutions. In addition to many other climate applications, GRACE data has been used to improve the understanding of global ocean circulation. It should be noted that early results from GOCE show that it produces higher resolution maps of the constant part of the Earth's gravity field than GRACE (i.e. the higher degree terms) [13] However, GRACE is able to monitor temporal variations, allowing scientists to track changes in Earth's gravity due to changes in the water cycle.

1.4 Motivation

Due to the heavy demands posed on computational resources in the case of classical numerical integration techniques, alternative methods of gravity recovery have been developed. These are not alternatives to GRACE; these are

alternative approaches to gravity field recovery using high-low satellite tracking to LEO satellites. They rely on satellite positions as pseudo-observables. CHAMP kinematic positions and accelerometer data have been used to produce gravity field models with a quality comparable to the official releases using an alternative approach by means of the energy integral method [14]. Several other methods are also being explored. These include formulating a boundary value problem in the form of an integral equation of Fredholm type and an acceleration approach based directly on Newton's equation of motion [15]. The results from these methods are promising. The problem is formulated such that the effects of the errors in the initial conditions of the satellite state and linearization errors associated with conventional techniques are mitigated. [15]

Kinematic positions are used instead of dynamic and reduced-dynamic orbits which may be biased towards the *a priori* gravity field model used for POD. However, it has been shown that in unconstrained dynamic estimation, there is no bias. The bias comes when constraints are implemented. Numerical analysis reveals that the knowledge of precise satellite velocity and acceleration information limits the resolution of these alternative methods. Therefore, the possibility of deriving highly accurate (and correlated) kinematic velocity and acceleration vectors has to be more closely investigated [16]. This is a major question addressed in this study: which numerical differentiation method is best for kinematically determined positions.

A major issue for POD is determining an accurate estimate of the orbit

error in the results. Since there is no direct measure of the absolute 3-D orbit error, several different performance tests are needed. Tracking data post-fit residual performance is an important performance metric. Both dependent (i.e., the GPS data used in the orbit solution) and independent data residual performance are normally assessed. In this study, independent SLR and KBR data residuals are used. Note that high-elevation SLR residuals provide a direct measurement of absolute radial orbit error. Another important means of characterizing orbit error is to compare independently computed ephemerides. This is why it is also important to analyze the differences between kinematic, dynamic, and reduced-dynamic orbits. Note that the orbits compared should be as close to equal quality as possible, otherwise the less accurate orbit dominates the difference. Such comparisons provides an opportunity to evaluate long-term systematic orbit effects and relative error caused by modeling differences such as gravity and tides. [9]

While the dynamic, reduced-dynamic, and kinematic methods have been extensively validated, it may be that kinematic orbits contain more information about the shorter wavelength gravity terms, due to the limitations of the background gravity model [17]. With plenty of new geodetic missions equipped with high-accuracy GPS receivers such as GOCE and SWARM, kinematic orbit analysis methods of gravity recovery have gained further relevance [15].

1.5 Thesis Organization

Chapter 2 discusses the key concepts of dynamic, reduced-dynamic, and kinematic orbit determination as well as the processing environments for the orbits used in this thesis. A complete description of orbit determination is provided in Appendix B along with a brief discussion of GPS in Appendix A since it is enables both reduced-dynamic and kinematic orbit determination. Chapter 3 provides context for how well the velocities should be recovered by examining the spectral relationship between velocity variance and gravity potential. Chapter 4 covers the various numerical differentiation methods used in this study. Chapter 5 provides the validation of these methods using dynamic and reduced-dynamic orbits. Chapter 6 presents the numerical kinematic velocity and acceleration results. Chapter 7 compares the three trajectory types to the KBR data as an external validation step. Finally, conclusions and future work are discussed in Chapter 8.

Chapter 2

Precise Orbit Determination Techniques

In this chapter, the processing environments for the dynamic, reduced-dynamic, and kinematic orbit data used in this study is discussed. The focus is on the background models and a high level discussion of the concepts for each method. For a complete description of the fundamentals of orbit determination please refer to Appendix B.

2.1 Dynamic Orbit Determination

The dynamic orbits analyzed in this study were created at UT/CSR as part of the GRACE RL05 processing. The Multi-Satellite Orbit Determination Program (MSODP) [3] was used to produce these solutions. This program was derived from legacy software, UTOPIA (University of Texas Orbit Processor), which was used for single satellite orbit determination. MSODP was originally developed to support GPS-based POD for the T/P mission, but was later modified to handle a general mix of multiple high and low satellites. It utilizes a traditional dynamic approach which relies on accurate force models and the adjustment of force model parameters. For numerical integration and estimation, the fixed multi-step Krogh-Shampine-Gordon (with the Cowell for-

mulation) and batch least-squares algorithms are used, respectively. The orbit accuracy depends on the quality of the force models, the parameterization, arc length and the accuracy of the tracking data [18]. The strategies used in GRACE dynamic POD processing at UT/CSR are discussed in this section.

First, the force models and reference frame definitions are shown in Tables 2.1 and 2.2. Most of the conventions follow those given in IERS Conventions. Note that the background gravity model is the mean field GIF48. This is an interim mean gravity field model created from a combination of the 66-month time-series of UT/CSR RL04 products spanning from 2003 through 2011 [19]. For further information processing standards, models, and parameters, please consult [19].

Table 2.1: GRACE POD Force Models

Force Model	Source
Mean Geopotential	GIF48 (360 x 360)
Atmosphere and Ocean Variability	AOD1B RL05
Solid Earth Tides	IERS-2010
Ocean Tides	GOT4.8 and FES2004
Ocean Pole Tides	Desai 2002
N-Body Perturbations	DE-405 Planetary Ephemerides
General Relativistic Perturbations	IERS-2010

Table 2.2: GRACE Reference Frame Models

Reference Frame	Source
Inertial Reference Frame	J2000.0
Earth-fixed Reference Frame	IGS2008
Precession and Nutation	IAU2000A
Sidereal Rotation	IERS-2003, IERS C04, and IERS 1996
Polar Motion	IERS C04 and IERS-1996
Ground Station Coordinates	IGS2008

The primary observations are GPS double-differenced carrier phase-converted pseudorange measurements. This differential technique requires the use of two receivers visible simultaneously from the same set of GPS satellites. One of the receivers is chosen to be on-board the GRACE satellite, and the second one is chosen to be at a known location on the Earth's surface (i.e., at a ground station). This type of formation of double difference (DD) combination is called High-Low combination. Figure 2.1 illustrates this type of DD combination. The High-Low technique was used on the T/P mission with very accurate results [5].

The GPS measurements are created in a pre-processing step before being used in MSODP. Raw measurements are made on-board with the BlackJack receivers and are downlinked to ground stations. This data is calibrated and time-tagged at JPL before being distributed to the science operations centers. UT/CSR receives the GPS data files and converts them to Receiver Independent Exchange (RINEX) format, which includes the phase differences between the L1 and L2 carrier signals received from a GPS satellite and the

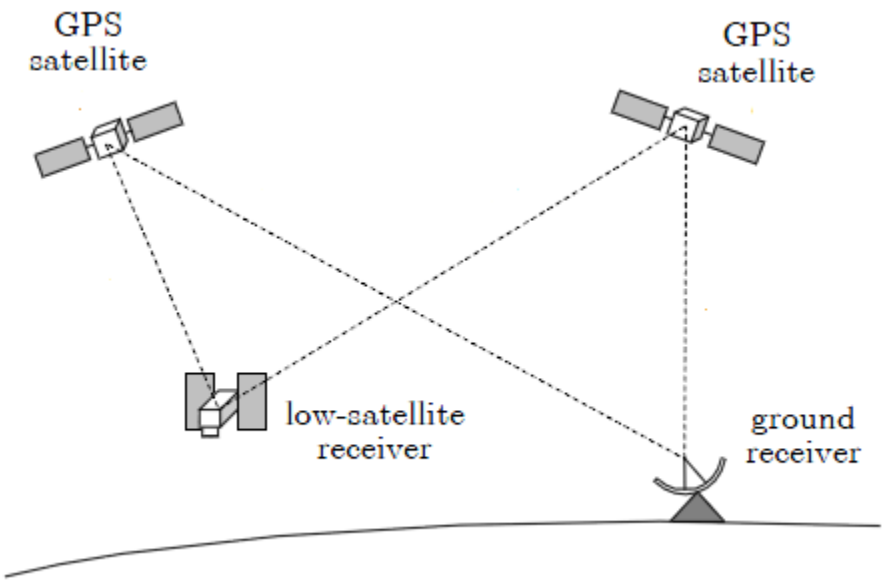

Figure 2.1: Double-Difference High-Low Geometry [20]

reference carrier signals generated within the BlackJack receiver. Knowledge of phase measurements on two different carriers allows the frequency-dependent effects of the ionosphere to be mitigated. The ionosphere-free phase observables are then converted to a pseudorange, which is biased by GPS satellite and receiver clock errors. In this case, a singe-difference high-low (SDHL) measurement is obtained by differencing pseudorange measurements from the onboard BlackJack receiver and a ground-based receiver to the same GPS satellite. The ground-based receiver measurements are provided by the IGS. Based on the results obtained by [21], the GPS orbits are held fixed to IGS solutions in the POD process. By differencing two single-differences (measured to different GPS satellites), a double-difference high-low (DDHL) measure-

ment is formed. Finally, corrections to the DDHL measurements are applied to account for propagation delays, relativistic effects, phase center variations (PCV), and ground station related effects [3].

In order to account for unmodeled or incorrectly modeled forces, force model parameterization is used for GRACE POD processing [18]. In this manner, force model parameters, such as the atmospheric drag coefficient and empirical accelerations are introduced to the orbit determination procedure. As additional empirical accelerations are estimated in the dynamic orbit process, it can start to approximate a reduced-dynamic approach [22]. In this case, empirical accelerations include tangential perturbations and one-cycle-per-orbital-revolution (1-cpr) force in the radial, transverse, and normal directions. The introduction of these parameters can significantly reduce orbit errors occurring at the 1-cpr frequency and in the along track direction [23]. They remove the long period effect of mismodeled forces and improve orbit determination accuracy and have piece-wise constant values over 3-4 hours. The complete set of estimated parameters for GRACE are listed in Table 2.3.

Table 2.3: GRACE POD Estimated Parameters [18]

Parameter	Description
GRACE Initial State	3D epoch position and velocity
GPS carrier phase ambiguity	One per combination per pass
Troposphere zenith delay	One per station in a 2.5-h arc
Empirical accelerations	1-cpr
Drag coefficient (C_D)	One per orbital revolution
GPS satellite OE corrections	One per arc for selected orbit elements
GPS receiver antenna correction	One per arc in nadir (Z) direction

2.2 Reduced-Dynamic Orbit Determination

At its core, the reduced-dynamic technique models empirical force parameters as stochastic processes, and their properties are adjusted to optimize the solution estimate by balancing the quality of tracking data and accuracy of force models. It operates by using the classical epoch state batch filter to generate a converged dynamic reference trajectory which is then used by a sequential filter for the final pass through the data [5]. The sequential filtering includes state noise compensation to combine geometric information from GPS with dynamic information contained in satellite force models. Empirical accelerations are included as process noise. GPS data density, geometry, and precision could be exploited by combining the geometric and dynamic approaches, leading to the reduced-dynamic method. The term reduced-dynamic orbit determination comes from the reduced susceptibility of the sequential process noise filter to dynamic model errors in comparison to the batch filter [24].

The reduced-dynamic orbits analyzed in this study were created at JPL and used as part of the GRACE RL05 processing at UT/CSR. These are the GPS Navigation Level 1B Format Record (GNV1B) files created with the GPS Inferred Positioning SYstem Orbit Analysis and SImulation Software (GIPSY-OASIS). The implemented form of the sequential filter algorithm used in GISPY-OASIS is a Square Root Information Filter (SRIF) pseudo-epoch state formulation with smoothing. Unlike MSODP, which uses a square root-free Givens method, the Householder method is used for orthogonal trans-

formations. The basics of sequential filtering with process noise, the SRIF, pseudo-epoch state and smoothing techniques are addressed in Appendix B. For a complete description of the filter as implemented in GIPSY-OASIS please refer to [24] and for more information about the SRIF with process noise and smoothing please see [1].

For the GNV1B files created at JPL, each GRACE satellite is processed independently using single receiver ambiguity resolution with GPS data [25]. The algorithm processes dual frequency GPS data from a single receiver together with wide-lane and phase bias estimates from the IGS network of receivers. The linear combinations of local phase biases are constrained in order to improve continuity with global bias estimates. In addition, in RL05 processing, the GPS clock solutions are solved for at a rate of 30 sec instead of 5 minutes (as was previously used).. This enables improved processing of higher rate GRACE POD solutions [25].

The reduced-dynamic solution is produced only in the final estimation step. First, a converged dynamic solution is obtained using a batch filter. The residuals from the batch filter contain information about the remaining orbit errors that can be exploited by the geometric strength of GPS observations. In the reduced-dynamic step, adjustments are made to the spacecraft state and all previously adjusted parameters except that the empirical accelerations [5]. The accelerations are now treated as process noise vectors that represent unmodeled or mismodeled body-fixed accelerations. This is re-estimated at each time step to allow high frequency due to gravity and atmospheric drag

to be accommodated in a manner that is difficult to achieve with an epoch state batch filter. Each component of the acceleration in the RTN directions is modeled as a first-order Gauss-Markov process constrained by an assigned correlation time and steady-state uncertainty. The stochastic acceleration parameters used in GRACE processing at JPL is summarized in Table 2.4. Note that this selection was based on the improved sampling rate of the GPS clock solutions at 30 sec intervals.

Table 2.4: GRACE Stochastic Acceleration Parameters [25]

Parameter	Process Noise ($\frac{nm}{s^2}$)	Update (s)	Time Correlation (s)
Constant normal	30	300	7,200
Constant radial	5	300	7,200
Constant transverse	10	300	7,200
1-cpr normal	5	6,750	21,600
1-cpr transverse	5	6,750	21,600

Finally, note that most of the force models used in JPL's processing are identical to those used at UT/CSR described in the previous section. For a complete list of the models and processing standards, please refer to [26].

2.3 Kinematic Orbit Determination

Based on the improvement of GPS data quality, kinematic orbit determination has become an alternative POD method for LEO's. It uses a precise-point positioning approach for point-wise calculations of satellite positions from GPS observations. The important characteristics of kinematic

orbits are that they do not use any force modeling and contain both signal and error at short wavelengths. The determination is usually done by using the zero-differenced, ionosphere-free GPS observations and their epoch-by-epoch phase differences. This is combined with precise orbits of GPS satellites and GPS clock products provided by the IGS to create a satellite trajectory. Note that the tracking data from ground stations is needed only for the generation of GPS clock corrections, since these errors are not removed from a double-differencing process.

The kinematic orbits analyzed in this study were provided by the Astronomical Institute of the University of Berne (AIUB) using the Bernese software. These were created using a zero-difference approach, and the satellite positions are provided at 30 second intervals in an Earth-fixed reference frame.

2.3.1 GPS Clock Corrections

The first step in the kinematic orbit determination process is to estimate the clock corrections to both the GPS satellites and the LEO GPS receiver. The corrections for the GPS receiver clock are determined along with the satellite's position. The corrections to the GPS satellite clocks are computed in a different step, and an algorithm to generate precise clock values for the GPS satellites at each observation epoch can be found in [27]. The code and phase observations from the IGS are analyzed together in order to establish a time series of precise satellite clock estimates for the entire GPS constellation. The GPS satellite orbits, troposhere parameters, and station

coordinates are fixed to the values provided by the IGS. Using the ionosphere-free linear combination results in a simple observation equation to estimate the clocks. Observation differences between subsequent epochs are computed to eliminate the initial ambiguity term. For both code and phase, an iterative process is set up to check for data problems and cycle slips. In the second step, the two clock sets (i.e., the code-derived absolute clock corrections and the phase derived clock difference corrections) are combined into one consistent time series of clock corrections. The matrix of the normal equation system associated with these corrections is tridiagonal. Therefore, the inversion required to solve the system is simple.

2.3.2 Point Positioning

At each epoch, code observations are used to determine positions, while phase difference observations are used to determine position differences of the LEO. The ionosphere-free linear combination of the $P1$ and $P2$ code measurements are used. Note that the relationship between the observables on the coordinates is non-linear. The orbits of the GPS satellites are known and fixed to those provided by the IGS while the GPS clock corrections are computed based on the procedure from the previous section. With these assumptions, the observation equation of one code observation from the LEO to one GPS satellite at epoch t_i is:

$$\rho = \|r_{GPS} - r_L\| + c \cdot \Delta t_L, \tag{2.1}$$

where ρ is the ionosphere-free linear combination of the observed pseudorange, r_{GPS} is the position vector of the observed GPS satellite at each epoch $t_i - \tau$ (where τ is the signal travel time), r_L is the unknown position vector of the LEO, c is the speed of light, and Δt_L is the unknown clock correction to the GPS receiver onboard the LEO satellite.

Equation 2.1 can be written for each observation acquired at one epoch. If more than four satellites are in view, the satellite's position coordinates x_L, y_L, and z_L and clock correction Δt_L are computed using a least squares adjustment for each epoch. The results are LEO point positions and clock corrections with the accuracy allowed by the quality of code measurements (0.5 to a few meters).

Ionopshere-free combination of carrier phase measurements are used to form differences between consecutive epochs and eliminate the initial ambiguity term,

$$b_i = (\lambda_{IF} A_{IF})_i, \tag{2.2}$$

where A_{IF} is the ambiguity and λ_{IF} is the wavelength of ionosphere-free carrier phase. Therefore, position differences are estimated between subsequent epochs. The ambiguity remains unchanged over an interval of continuous tracking unless a cycle slip or phase break occurs. The interval is usually not longer than about 40 minutes due to rapid change of relative geometry between LEO and GPS satellites. Therefore, there are about 15 continuous passes with constant ambiguities per day for a single GPS satellite. The observation equation for the phase difference between the epochs t_i and t_{i+1} for

one GPS satellite is [28]:

$$\begin{aligned}\Delta\phi(t_i, t_{i+1}) =& \|r_{GPS}(t_{i+1}) - r_L(t_{i+1})\| + c \cdot \Delta t_L(t_{i+1}) \qquad (2.3)\\ &- (\|r_{GPS}(t_i) - r_L(t_i)\| + c \cdot \Delta t_L(t_i)),\\ =& \|r_{GPS}(t_{i+1}) - r_L(t_i) - \Delta r_L(t_{i,i+1})\| \qquad (2.4)\\ &- \|r_{GPS}(t_i) - r_L(t_i)\| + c \cdot \Delta\Delta t_L(t_{i,i+1}).\end{aligned}$$

with $\Delta r_L(t_{i,i+1}) = r_L(t_{i+1}) - r_L(t_i)$ and $\Delta\Delta t_(t_{i,i+1}) = \Delta t_L(t_{i+i}) - \Delta t_L(t_i)$. The unknown coordinates $r_L(t_i)$ for the first epoch remain constant in this equation. However, the coefficient of this parameter in the linearized observation equation is several orders of magnitude smaller than that for Δr_L and is proportional to the time interval $t_{i+1} - t_i$. If an *a priori* orbit is available, the correction term for $r_L(t_i)$ can be neglected. Note that the code positions determined in the previous step or an orbit prediction from a previously processed arc can be used as the *a priori* orbit. Similarly to the GPS satellite clock corrections, the clock corrections generated from code,Δt_L and clock correction differences generated from phase differences $\Delta\Delta t_L$, may be combined to obtain satellite clock corrections with an accuracy given by the phase.

Note that the quality of kinematic solutions is highly dependent on the quality of GPS data available. Kinematic POD is particularly susceptible to large errors when measurements contain outliers or cycle slips. Additionally, errors occur at epochs where no position differences can be computed due to insufficient phase observations (e.g., caused by a loss of phase lock of the receiver). The arcs surrounding these epochs are not connected by the phase

data. This can lead to large spikes in the solution based on the accuracy of the code. Therefore, data screening is needed in order to use the results from the kinematic orbit determination [29]. This topic will be addressed in a subsequent chapter. Currently, an accuracy of 1-3 cm is achievable using the kinematic orbit determination approach [30].

Chapter 3

Velocity Variation and Gravity Potential

This chapter provides context for how well the velocities should be known in relation gravity field recovery. Using the semi-analytic approach as shown in Kim [8], the spectral relationship between the potential disturbance and velocity disturbance on a satellite at a given altitude can be computed.

To derive this relationship, we start with the following energy equation

$$\frac{1}{2}v^2 - U = E, \tag{3.1}$$

where E is the total energy and U is the total gravitational potential energy, and v is the velocity of the satellite. Note that non-conservative forces (i.e., atmospheric drag, radiation pressure, etc) are ignored such that the total energy is conserved. Therefore, when a satellite passes over a mass anomaly where the potential energy is less, the loss in total energy is compensated by an increase of kinetic energy, which in this case corresponds to a change in the satellite's velocity [8].

Next, U and v can be decomposed into a reference component and a

disturbance component as

$$U = U_0 + T', \tag{3.2}$$

$$v = v_0 + \Delta v,$$

where U_0 is the nominal gravity potential representing the gravity at the reference ellipsoid (consisting of only even zonal harmonics), T' is the disturbing potential which is the difference between the actual gravity and the reference gravity, and Δv is the velocity variation due to the disturbing potential.

The reference velocity v_0 is related to the reference gravity potential U_0 by

$$\frac{1}{2}v_0^2 - U_0 = E. \tag{3.3}$$

Substituting Equation 3.2 into 3.1 and eliminating higher order terms leads to the following expression

$$\frac{1}{2}v_0^2 + v_0\Delta v - U_0 - T = E. \tag{3.4}$$

Comparing this result to Equation 3.3 provides the relationship between velocity variation and the disturbing potential at a given satellite altitude:

$$\Delta v = \frac{1}{v_0}T'. \tag{3.5}$$

This expression can be converted to the spectral domain using spherical harmonics as

$$\Delta v(\phi, \lambda) = \sum_{n=0}^{\infty}\sum_{m=0}^{n} \bar{P}_{nm}(sin\phi)(\Delta\bar{v}^c_{nm}cosm\lambda + \Delta\bar{v}^s_{nm}sinm\lambda) \tag{3.6}$$

where (ϕ, λ) are geodetic latitude and longitude, the subscripts n and m denote degree and order, $\bar{P}_{nm}$ are the normalized Legendre associated functions, and $\Delta\bar{v}^c_{nm}$ and $\Delta\bar{v}^s_{nm}$ are the harmonic coefficients, respectively. Similarly, the disturbing potential acting on a satellite at a given attitude can be expressed as

$$T' = T(r, \phi, \lambda) = \frac{GM}{R_e} \sum_{n=2}^{\infty} \sum_{m=0}^{n} \left(\frac{R_e}{r} \right)^{n+1} \bar{P}_{nm}(sin\phi)(\bar{C}'_{nm} cosm\lambda + \bar{S}_{nm} sinm\lambda). \tag{3.7}$$

This equation does not include the $n = 0$ and $n = 1$ terms which correspond to the two body term and Earth center offset from the coordinate origin, respectively. The velocity errors in these terms are not mapped into the gravity potential error since the velocity spectrum from Equation 3.6 includes these two term. The error variance T is defined as an average of the expectation of the squared error over the unit sphere. Due to the orthogonality, the variance of T' is related to the degree error variance of T as follows

$$\sigma^2(\delta T') = \sum_{n=2}^{\infty} \left(\frac{R_e}{r} \right)^{2n+2} \sigma_n^2(\delta T), \tag{3.8}$$

where the nth degree variance of T is given by

$$\sigma_n^2(\delta T) = \sum_{m=0}^{n} (\delta\bar{C}^2_{nm} + \delta\bar{S}^2_{nm}). \tag{3.9}$$

Note that we have defined T as the disturbing potential on the Earth's surface and T' as the disturbing gravity potential at the satellite altitude. The coefficients $\bar{C}'_{nm}$ are obtained by subtracting the even zonal coefficients of the normal gravity field from full spherical harmonic coefficients.

Similarly, substituting Equations 3.6 and 3.7 into Equation 3.5 and taking error variances, the relationship between the degree error variances of velocity and gravity obtained as

$$\sigma_n^2(\Delta v) = \frac{GM}{R_e}\left(\frac{R_e}{r}\right)^{2n+1}\sigma_n^2(T) \tag{3.10}$$

where the circular velocity, $\sqrt{GM/r}$, replaces the reference velocity v_0.

Since a significant amount of information is already understood about the Earth's gravity field from other branches of geophysics and previous observations, the core interest of this study is putting the requirements on the "innovations" that were observed by GRACE and how well the velocity knowledge must be for chasing the time variable gravity signal when GRACE is no longer flying. In order to compute the relationship in Equation 3.10, the following definitions are required. The potential disturbance can be represented by monthly gravity estimates from GRACE. The "variability" is defined as monthly variations relative to the population mean of a time-series of GRACE gravity estimates. With these definitions, the degree spectrum of the potential can be computed. This is then used to calculate the degree velocity spectrum at a specific orbit altitude. If the velocity spectrum is root-sum-squared, the velocity bounds for gravity estimation can be obtained.

For this study, a time-averaged variability spectrum was analyzed. This subtracted from the population mean of monthly RL05 GRACE solutions from 2004 through 2012. To ensure that the sum squares over the degrees actually converged (the GRACE estimates have increasing errors and may diverge if

higher degrees are added), the partial sums were only carried up to degree 60. Figure 3.1 shows the resulting error variance of velocity variation.

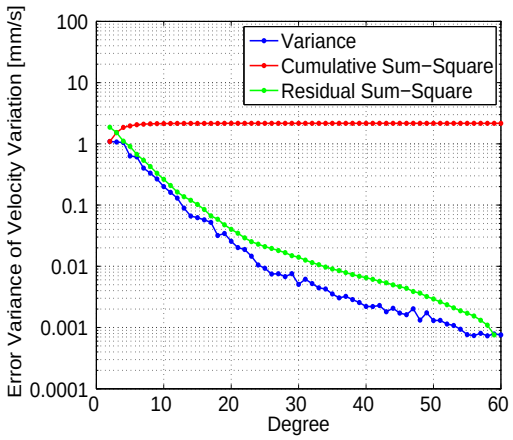

Figure 3.1: Velocity Uncertainty using Time-Averaged Spectrum

The results indicate that velocity must be known better than 0.01 mm/s to solve for the time-variable gravity field up to degree and order 30, and 0.001 mm/s for degree and order 60 (for a satellite at an altitude of 450 km). In addition to the velocity spectrum, the cumulative root-sum-square and residual root-square statistics are shown by degree. Note that the cumulative root-sum-square converges to 2.159 mm/s.

Chapter 4

Numerical Differentiation Methods

4.1 Introduction

As previously mentioned, one drawback of using kinematic orbits is the lack of velocity and acceleration information. Since accurate velocities and accelerations are required for gravity field estimation, numerical differentiation methods must be applied directly to the kinematic positions.

Numerical differentiation is the process of finding the numerical value of a derivative of a given function at a given point. In orbital mechanics, it is typically associated with trajectory problems, either in the form of propagation or optimization of a boundary value problem. Assume that there is a procedure to compute a function, $f(t)$. Although there are more complicated methods, the simplest way to compute the derivative, $f'(t)$, is by using the definition:

$$f'(t) \approx \frac{f(t+h) - f(t)}{h}, \tag{4.1}$$

from the limit as $h \to 0$. While there is still the problem of finding the optimal value of h, this is a simple procedure to implement. All one has to do is evaluate $f(t+h)$ and $f(t)$.

Numerically differentiating kinematic orbits is more complicated. In the case of this thesis, techniques must be applied to noisy data that is tabulated at

equally spaced 30 second intervals. In other words, one cannot explicitly evaluate the function since we are operating on a discrete data set. The relatively large time step of 30 seconds is one of the limiting factors. Cubic smoothing splines with remove-restore and Newton-Gregory interpolation were used to derive kinematic velocities in deriving the CHAMP-based gravity models TUM-1S and TUM-2Sp, respectively, created at the Institute of Astronomical and Physical Geodesy, Technical University of Munich [17]. Polynomial interpolation was used to derive kinematic accelerations by Liu [31] at the Delft University of Technology for gravity field recovery from GRACE SST data using an acceleration approach. While there have been some initial studies on the performance of various numerical differentiation methods such as [17] and [32], the results were case sensitive for the CHAMP satellite. In addition to the methods analyzed in [32], three new methods are tested in this study: Hermite interpolation, polynomial smoothing in the form of a Savitzky-Golay filter, and a CRN digital filter.

4.2 Hermite Interpolation

Hermite interpolation is commonly used for precise interpolation of satellite states [33]. A 10th order Hermite polynomial interpolation routine is used by several agencies dealing with the post-processing of satellite orbits, including IGS GPS orbits [33].

Hermite interpolation employs the use of the higher order derivative in

the interpolating function taking the general form [33]:

$$F(t) = \sum_{j=0}^{N} [H_j(t) y_j + h_j(t) y'_j] \tag{4.2}$$

where,

$t =$ time at which the satellite state is required,

$y_j =$ the satellite position in a single dimension at node j,

$H_j(t) =$ the Hermite polynomial coefficient associated with y_j for time t,

$y'_j =$ satellite velocity in a single dimension at node j,

$h_j(t) =$ Hermite polynomial coefficient associated with y'_j for time t.

By including the first derivative, the behavior becomes constrained and the accuracy unstable $N-1$ order polynomials improves when N is large. The information content in the 10th order Hermite polynomial is nearly equivalent to a polynomial of order $2N$. For dynamic and reduced-dynamic orbits, the velocity vector is available along with the position vector, thus enabling the use of Hermite interpolation.

Hermite interpolation is especially useful when considering its connection to orbital mechanics. Since the equations of motion of an LEO are second order, the coupling of position and velocity completely describe the state at any given instant. Numerical studies revealed that there is not much difference in accuracy between third order and tenth order Hermitian interpolation [33]. Therefore, higher order solutions do not necessarily improve the precision and

may even cause the system to become unstable. In this study, a 4th-order Hermite interpolation method was used.

One important note about Hermite interpolation is that it performs very poorly without accurate velocities. This is the case with kinematic orbits. In order to recover the velocities using Hermite interpolation, an iterative procedure was applied. Since the output are the first and second derivatives at the desired points, the input velocities are updated with these new values and used on the next iteration. This requires an initial guess for the velocities; in this case, the simple central difference method was used. Please refer to Table C.1 in Appendix C for summary of the results when using this iterative procedure.

4.3 Cubic Spline Interpolation

The implementation of cubic spline interpolations was based on the algorithm from [34]. Given a tabulated function $x_i = x(t_i), i = 1, \ldots, n$, consider the interval between t_j and t_{j+1}. Applying linear interpolation within this interval results in

$$x = Ax_j + Bx_{j+1}, \tag{4.3}$$

where,

$$A \equiv \frac{t_{j+1} - t}{t_{j+1} - t_j}, \tag{4.4}$$

$$B \equiv 1 - A = \frac{t - t_j}{t_{j+1} - t_j}. \tag{4.5}$$

Note that this is a special case of the general Lagrange interpolation formula shown in the next section (Equation 4.12).

Since it is piece-wise linear, Equation 4.3 has zero second derivative in the interior of each interval and an undefined second derivative at the node t_j. The goal of cubic spline interpolation is to get an interpolation formula that is smooth in the first derivative and continuous in the second derivative, both within an interval and at the boundaries.

If tabulated values of the second derivative were available, x'', they could be added to the right hand side of the equation. Now, it is a cubic polynomial whose second derivative varies linearly from a value x''_j on the left to a value x''_{j+1} on the right, and the second derivative is continuous. If the second derivative is not available, these values can be set to zero at t_j and t_{j+1}. This will still satisfy the agreement with the tabulated functional values x_j and x_{j+1} at the endpoints t_j and t_{j+1}.

Using this information, we can construct

$$x = Ax_j + Bx_{j+1} + Cx''_j + Dx''_{j+1}, \tag{4.6}$$

where C and D are now defined as,

$$C \equiv \frac{1}{6}(A^3 - A)(t_{j+1} - t_j)^2 \quad D \equiv \frac{1}{6}(B^3 - B)(t_{j+1} - t_j)^2. \tag{4.7}$$

Note that the independent variable t is in the linear t-dependence of A and B, and the cubic t-dependence of C and D.

One can readily check that x'' is in fact the second derivative of the new interpolating polynomial. Taking the derivatives of Equations 4.6 and 4.7 with respect to t and using the definitions of A, B, C, and D to compute the derivatives, results in

$$\frac{dx}{dt} = \frac{x_{j+1} - x_j}{t_{j+1} - t_j} - \frac{3A^2 - 1}{6}(t_{j+1} - t_j)x''_j + \frac{3B^2 - 1}{6}(t_{j+1} - t_j)x''_{j+1} \tag{4.8}$$

for the first derivative and

$$\frac{d^2x}{dt^2} = Ax''_j + By''_{j+1} \tag{4.9}$$

for the second derivative. Since $A = 1$ at x_j, $A = 0$ at x_{j+1}, while B is just the other way around, the second derivative equation shows that x'' is just the tabulated second derivative, and the second derivative will be continuous across the interval boundaries, for example (t_{j-1}, t_j) and (t_j, t_{j+1}).

However, even though we assumed x''_j's to be known, it is not. The first derivative will be continuous across the boundary between two intervals. The key concept of a cubic spline is to require this continuity and to use it to get equations for the second derivative, x''_j.

The required equations are obtained by setting $t = t_j$ in the interval $(t_j, t_{j+1}$. Rearranging, this gives (for $j = 2, \ldots, n-1$):

$$\frac{t_j - t_{j-1}}{6}x''_{j-1} + \frac{t_{j+1} - t_{j-1}}{3}x''_j + \frac{t_{j+1} - t_j}{6}x''_{j+1} = \frac{x_{j+1} - x_j}{tj + 1 - t_j} - \frac{x_j - x_{-1j}}{tj - t_{j-1}} \tag{4.10}$$

These are $n-2$ linear equations in the n unknowns $x''_i, i = 1, \ldots, n$. Therefore, there is now a two-parameter family of possible solutions.

In order to obtain a unique solution, two more restrictions must be added. This is obtained by specifying the boundary conditions at t_1 and t_n. The most common method is to set both x_1'' and x_n'' equal to zero, providing a "natural" cubic spline, which has zero second derivative on one or both of its boundaries.

One reason that cubic splines are especially practical is that the set of equations along with the two additional boundary conditions, are not only linear but also tridiagonal. Each x_j'' is coupled only to its nearest neighbors at $j \pm 1$. Therefore, the equations can be solved in $\mathcal{O}(n)$ operations by a tridiagonal algorithm.

4.4 Polynomial Fitting

Through any two points there is a unique line; through any three points, a unique quadratic, etc. The interpolating polynomial of degree $n-1$ through n points is given explicitly by Lagrange's classical formula,

$$P_n(t) = \sum_{k=0}^{n} x_k \prod_{\substack{i=0 \\ i \neq k}}^{n} \frac{(t - t_i)}{(t_k - t_i)}, \tag{4.11}$$

which, when written explicitly, becomes,

$$\begin{aligned} P_n(t) =& \frac{(t-t_2)(t-t_3)\dots(t-t_n)}{(t_1-t_2)(x_1-x_3)\dots(t_1-t_n)} x_1 + \frac{(t-t_1)(t-t_3)\dots(t-t_n)}{(t_2-t_1)(t_2-t_3)\dots(t_2-t_n)} x_2 \\ &+ \dots + \frac{(t-t_1)(t-t_2)\dots(t-t_{n-1})}{(t_n-t_1)(t_n-t_2)\dots(t_n-t_1)} x_n. \end{aligned} \tag{4.12}$$

There are n terms, each a polynomial of degree $n-1$ and each constructed to be zero at all of the t_i except one, at which it is constructed to be x_i.

Though Lagrange's formula could be implemented directly, it is more common to use Neville's algorithm as it is more efficient and stable. This is based on the ability to construct higher order polynomials from a nested series of successively lower order polynomials, beginning with a polynomial of degree zero. This type of recursive polynomial is referred to as interpolation of Newton's polynomial through divided-differences. Given $n+1$ points, it first computes $n+1$ zeroth-order polynomials (i.e., constants) going through each point, then n first-order polynomials (i.e., lines) going through consecutive pairs of points, etc., ending with a single n-th order polynomial going through all n points. In other words, the various nodes form a "tableau" with "ancestors" on the left leading to a single "descendant" at the extreme right [34]. For example, consider $n = 4$,

$$
\begin{array}{lllll}
x_1: & y_1 = P_1 & & & \\
 & & P_{12} & & \\
x_2: & y_2 = P_2 & & P_{123} & \\
 & & P_{23} & & P_{1234} \\
x_3: & y_3 = P_3 & & P_{234} & \\
 & & P_{34} & & \\
x_4: & y_4 = P_4 & & &
\end{array}
$$

Figure 4.1: Tableau for $n = 4$ [34]

Neville's algorithm is a recursive way of filling in the numbers in the tableau one column at a time, from left to right. It is based on the recursive expression:

$$P_{i(i+1)\ldots(i+m)} = \frac{(x - x_{i+m})P_{i(i+1)\ldots(i+m-1)} + (x_i - x)P_{(i+1)(i+2)\ldots(i+m)}}{x_i - x_{i+m}} \quad (4.13)$$

The small differences between the parents and children are tracked by defining,

$$C_{m,i} \equiv P_{i\ldots(i+m)} - P_{i\ldots(i+m-1)}, \tag{4.14}$$
$$D_{m,i} \equiv P_{i\ldots(i+m)} - P_{(i+1)\ldots(i+m-1)}.$$

for $m = 1, 2, \ldots, n-1$. From this, the following expressions can be derived:

$$C_{m,i} \equiv P_{i\ldots(i+m)} - P_{i\ldots(i+m-1)}, \tag{4.15}$$
$$D_{m,i} \equiv P_{i\ldots(i+m)} - P_{(i+1)\ldots(i+m-1)}.$$

At each level m, the C's and D's are the corrections that make the interpolation one order higher. The final answer $P_{1\ldots n}$ is equal to the sum of any y_i's plus a set of C's and D's that form a path through the tableau to the rightmost entry.

To recover the derivative, this algorithm is used to solve for the coefficients of the interpolating polynomial. Consider the $n-1$th order polynomial at an arbitrary point of a time series, i.e.,

$$x_i = a_{n-1}t_i^{n-1} + a_{n-2}t_i^{n-2} + \cdots + a_2 t_i^2 + a_1 t_i + a_0. \tag{4.16}$$

If we interpolate to find the value of the interpolating polynomial at $t = 0$, then this value will be equivalent to a_0. Now we can subtract this from the values of x_i and divide each by its corresponding t_i. Throwing out one point (the one with the smallest t_i is a good candidate), we can repeat the procedure to find a_1 and so on. With the obtained coefficients, the time derivative (i.e., velocity in this context) can be derived as,

$$x_i' = (n-1)a_{n-1}t_i^{n-2} + (n-1)a_{n-2}t_i^{n-3} + \cdots + 2a_2 t_i + a_1. \tag{4.17}$$

As shown in [35], in order to obtain an adequate approximation of kinematic velocities and accelerations, a relatively high degree polynomial must be used. This requires a sufficient number of consecutive epochs. However, at higher order, the Vandermonde system can become ill-conditioned and the algorithm unstable. In this study, a 7th order polynomial was implemented with 8 points used for estimating the coefficients. This process was implemented piece-wise. In other words, at the ith point, the neighboring points $i-3$th,$i-2$th,...,$i+3$th,$i+4$th are used. At the end a continuous arc, i.e., the first three and last three points, the velocity is estimated from the polynomial derived in the fourth and 5th to last points, respectively.

4.5 Newton-Gregory Interpolation

Recall the $(n-1)$th order polynomial showed in the previous section (i.e., Equation 4.16). This equation contains n unknowns, the coefficients a_i from $i = 0, \ldots, n-1$. By considering n neighboring points, one can solve for these coefficients. Equivalently,

$$\begin{aligned} x_i =& a_0 + a_1(t_i - t_1) + a_2(t_i - t_1)(t_i - t_2) + \cdots \\ &+ a_{n-1}(t_i - t_1)(t_i - t_2)\ldots(t_i - t_{n-1}), \end{aligned} \tag{4.18}$$

where $t_1, t_2, \ldots, t_{n-1}$ are the known values of the interpolation (i.e., the existing entries of the time series) and t_i is the point at which the interpolation should be evaluated. It is equivalent with the polynomial in that both forms describe the orbit with powers of t up to order $n-1$ and n coefficients a_i. The

number of unknowns, a_i, is n, so that we can unequivocally determine them by considering n neighboring points of the time series.

The solution can be obtained by solving for the increasing orders of i. The coefficients at the first point are:

$$a_0 = x_1, a_1 = \frac{x_2 - x_1}{t_2 - t_1}, a_2 = \frac{\frac{x_3 - x_1}{t_3 - t_1} - \frac{x_2 - x_1}{t_2 - t_1}}{t_3 - t_2}. \tag{4.19}$$

The 0th coefficient, a_0, is equal to x itself and can be explained as the 0th gradient of x. The a_1 coefficient is the first order gradient, while a_2 is the coefficient of the second-order gradient. Therefore, the nth coefficient can be generalized as the nth gradient of the function.

By assuming equally spaced nodes, t, the solution gets simpler, since any $t_{i+1} - t_i$ time difference is constant, h, and it redefines the nth order gradient as:

$$a_i = \frac{1}{n!} \frac{\Delta^n x_0}{h^n} \tag{4.20}$$

After obtaining the coefficients using the equation above, the first derivative of a general jth tag of the interpolation formula $a_{j-1}(t_i - t_1)(t_i - t_2) \dots (t_i - t_{j-1})$ becomes:

$$a_{j-1} \sum_{k=1}^{j-1} \prod_{f=1}^{j-1} (t_i - t_f) \tag{4.21}$$

for $f \neq k$.

The advantage of this technique is forward difference errors are reduced. By repeatedly forming differences of successive positions, biases drop out and if adjacent positions are correlated, the influence of measurement errors decreases

significantly [16]. In this study, 7 adjacent points are used for the interpolation and the solution for the first time derivative of x can be shown to be [32]:

$$\dot{x}_i = \frac{1}{60h}(-x_{i-3} + 9x_{i-2} - 45x_{i-1} + 45x_{i+1} - 9x_{i+2} + x_{i+3}); \tag{4.22}$$

4.6 Cubic Smoothing Spline

The cubic smoothing spline method used in this study is based on the one derived by Schoenberg and Reinsch as shown in [36]. Given the approximate values $x_i = g(t_i) + \epsilon_i$ of some "smooth" function g at $t_1, \ldots, t_n$, and an estimate δx_i of the standard deviation in x_i, we try to recover g from this data by constructing the function $f = f_p$ that minimizes

$$p \sum_{i=1}^{n} \left(\frac{x_i - f(t_i)}{\delta x_i} \right)^2 + (1-p) \int_{x_1}^{x_n} (f^m(t))^2 \mathrm{d}t, \tag{4.23}$$

over all functions f with m derivatives. Minimizing this performance index is a compromise between the desire to stay close to the given data and obtain a smooth function which depends on the choice of p.

The solution f_p is a spline of order $k = 2m$, with simple knots at $x_2, \ldots, x_{n-1}$, satisfying the "natural" end conditions:

$$f_p^{(j)}(x_1) = f_p^{(j)}(x_n) = 0 \quad \text{for } j = m, \ldots, k-2. \tag{4.24}$$

Correspondingly, the smoothing parameter S is defined as

$$S(f) = \sum_{i=1}^{n} ((x_i - f(t_i))/\delta y_i)^2, \tag{4.25}$$

where $S(f_p)$ strictly decreases as p goes from 0^+ to 1^-, to a value of 0 at $p = 1^-$, unless $S(f_p) = 0$ for all p. It is therefore possible to determine, for a given S, the function f_S that minimizes $\int_a^b ((f^{(m)}(x))^2 \mathrm{d}x$ over all f for which $S(f) \leq S$. The Schoenberg and Reinsch method minimizes $\int (f^{(m)}(t))^2 \mathrm{d}x$ instead of the sum of squares of mth differences [36].

The derivative of the cubic smoothing spline that provides a unique solution of $f(t_i)$ has the form:

$$g'(t) = 3a_i t^2 + 2b_i t + c_i \tag{4.26}$$

The exact algorithm to solve for the unknown coefficients is shown in [36] and uses a Cholesky decomposition to solve the system.

The remaining problem is the selection of the smoothing parameter S. Reinsch proposed that S should be within $\sqrt{2N}$ of N. The extent of smoothing depends on the length of the time series and the amplitude of the signal [17]. Therefore, the smoothing parameter was defined to be $S =$ scale factor $\times$ length(arc) . Several scale factors were tested on the kinematic orbits to see how well the resulting cubic smoothing spline reconstructs the known positions and unknown velocities. The results of this study are shown in Table C.2 in Appendix C.

4.7 Polynomial Smoothing - Savitzky Golay Filter

Typically, polynomial smoothing is the same as using polynomial interpolation as shown in Section 4.4. However, in the case of "smoothing", more

than n points are used to fit the $n-1$th polynomial, i.e., fitting a 7th order polynomial to 12 adjacent points.

In this study, a low-pass digital filter known as the Savitzky-Golay from [34] was used. It is derived directly in the time domain from a particular formulation of the data smoothing problem in the time domain. Historically, this filter was used to extract the relative widths and heights of spectral lines in noisy data. It works by performing a least-squares fit of a polynomial of degree M, using an additional number n_L of points to the left and some number n_R of points to the right of each desired x value. The estimated derivative is then the derivative of the resulting fitted polynomial.

A digital filter is applied to a series of equally spaced data values $f_1 \equiv f(t_i)$, where $t_1 \equiv t_0 + i\Delta$ for some constant sampling interval, Δ. The simplest form of digital filter (i.e., finite-impulse response filter) replaces each data value f_i by a linear combination g_i of itself and a number of neighboring points,

$$g_i = \sum_{n=-n_L}^{n_R} c_n f_{i+n}, \tag{4.27}$$

where n_L represents the number of points to the left of the data point of interest and n_R is the number of points to the right. A "causal" filter would have $n_R = 0$.

To derive the Savitzky-Golay filter, consider the simplest possible averaging procedure: for some fixed $n_L = n_R$, compute each g_i as the average of data points from f_{i-n_L} to f_{i-n_R}. This is referred to as moving-window averaging. It corresponds to Equation 4.34 where $c_n = 1/(n_L + n_R + 1)$. For a

linear or constant function, no bias is introduced into the result. However, in the case of a satellite orbit, there are non-zero second derivatives and biases are introduced. Note that moving window averaging preserves the area under a spectral line (i.e., the zeroth moment) and the first moment if the window is symmetric. However, the second moment (i.e., the line width) is violated.

The Savitzky-Golay filter is designed to find filter coefficients c_n that preserve higher moments. This is accomplished by approximating the underlying function within the moving window by a higher-order polynomial instead of a constant. For each point f_i, a polynomial is fitted in the least-squares sense to all $n_L + n_R + 1$ points in the moving window, and then set g_i to be the value of the polynomial at position i. The values of the polynomial are not used at any other point; instead when the next point, f_{i+1}, is considered, a new least-squares fit is done using the shifted window. Since the least-squares fitting involves a linear matrix inversion, the coefficients of a fitted polynomial are also linear. This implies that all the fitting can be performed on a fictitious data set, consisting of all zeros except for a single entry equal to one and the fits can be performed on the real data just by taking linear combinations. There are particular sets of filter coefficients c_n for which Equation 4.34 "automatically" accomplishes the process of polynomial least-squares fitting inside a moving window.

To derive these coefficients, we want to fit a polynomial of degree m in i, i.e fit $a_0 + a_1 i + \cdots + a_m i^m$ to the values $f_{-n_L}, \ldots, f_{n_R}$. Then g_0 will be the value of the polynomial at $i = 0$, namely a_0. The design matrix for this

problem becomes:

$$A_{ij} = i^j \quad i = -n_L, \ldots, n_R, \quad j = 0, \ldots, m, \tag{4.28}$$

and the normal equations for the vector for a_j's in terms of the vector of f_i's s in matrix notation:

$$(A^{\mathrm{T}} \cdot A) \cdot a = A^{\mathrm{T}} \cdot f, \tag{4.29}$$

$$a = (A^{\mathrm{T}} \cdot A)^{-1} \cdot (A^{\mathrm{T}} \cdot f). \tag{4.30}$$

with the specific forms

$$A^{\mathrm{T}} \cdot A_{ij} = \sum_{k=-n_L}^{n_R} A_{ki} A_{kj} = \sum_{k=-n_L}^{n_R} k^{i+j}, \tag{4.31}$$

$$A^{\mathrm{T}} \cdot f_j = \sum_{k=-n_L}^{n_R} A_{kj} f_k = \sum_{k=-n_L}^{n_R} k^j f_k. \tag{4.32}$$

Since the coefficients c_n is the component a_0 when f is replaced by the unit vector $\hat{e}_n$,$-n_L \leq n < n_R$, we obtain

$$c_n = [(A^{\mathrm{T}} \cdot A)^{-1} \cdot (A^{\mathrm{T}} \cdot \hat{e}_n)]_0 = \sum_{i=0}^{M} [(A^{\mathrm{T}} \cdot A)^{-1}]_{0m} n^m. \tag{4.33}$$

Note that this equation shows that only one row of the inverse matrix is needed. This can be obtained numerically by using what is known as an LU decomposition with only a single back substitution.

4.8 CRN Filter

The CRN is a finite-impulse response (FIR) digital filter, which stands for N self-convolutions of a rectangular time domain window function. This

type of filter was derived by Thomas (employed at JPL) [37] for applications with the GRACE KBR range system. It is first constructed in the frequency domain and then transformed to the time domain by taking the Fourier transform. The following section outlines the derivation of the CR7 filter as shown.

A basic time domain filter, F_n, operates in the time domain on the measured value R'_i to generate the observables at the nominal output rate:

$$R_i = \sum_{n=-n_h}^{n_h} F_n R'_{i-n}, \tag{4.34}$$

where,

$$n_h = 1/2(n_f - 1),$$
$$n_f = f_s t_f,$$

and n_f is the total number of points spanned by the filter and t_f is the filter time span. The index i is the ith value computed as a weighted sum of the input points symmetrically surrounding the ith point in time.

Nominally, a digital filter with a perfect rectangular response in the frequency domain is desired. A filter of this form can be derived by convolving a signal with $\sin x/x$ function in the time domain if the range of the function is extended to infinity. However, in implementation, the function is limited to a time window length by multiplication of a rectangular window function. The original filter in Equation 4.34 can be written as:

$$F_n = W_n \frac{\sin 2\phi Bn/f_s}{2\pi Bn/f_s}, \tag{4.35}$$

where,

$W_n =$ rectangular window function,

$1/f_s =$ time between input sample points,

$B =$ singe-sided bandwidth produced by a $\sin x/x$ function of infinite extent.

The window function is zero outside the filter time span and equal to one within it. The sharp transitions at the edges of the window function are resolved by multiplying the $\sin x/x$ function by a graduated window function. The graduated window function slowly decreases to zero at the edges of the window, smoothing the transition from $\sin x/x$ dependence to zero weight, reducing the ripple and sidelobes. The gain ripple is improved by constructing a window function whose Fourier transform has a fast sidelobe drop-off rate. It is the shape of the window function, in particular the width of the main lobe and magnitude and drop-off rate of its sidelobes, that determines the deviation in overall filter response from the desired rectangular shape.

The CRN filter is transformed from the frequency domain to the time domain by using time domain window functions formed by convolving a rectangular time domain window with itself n_c times. The convolution theorem shows that since the Fourier transform of a rectangular window has a $\sin x/x$ form in the frequency domain, the frequency response of an N-fold self-convolved time domain will be $(\sin x/x)^n$. As the number of self-convolutions increases, the sidelobes decrease rapidly which greatly helps in reducing gain ripple in the ultimate frequency response. However, there is a negative consequence to

increasing the number of convolutions as it produces a filter with a time span given approximately by $N_c t_R$. What this means is that for a total window time span of t_f, the width of the basis rectangle decreases in inverse proportion to n_c and therefore the width of the main lobe as well as the spacing of the sidelobes increase as n_c. The spreading of the sidelobes means that the sidelobe magnitude does not drop off as rapidly as a function of frequency due to the sidelobe count. For this reason, the CRN filter chosen for this study is 7 self-convolutions. The number of coefficients was selected to be 180, as a result of the study shown in Table C.3 in Appendix C.

The first time derivative of R_i is computed by the same algorithm where the weighting function F_n is replaced by its time derivatives:

$$\dot{R}_i^{out} = \sum_{i=-N_h}^{N_h} \dot{F}_n R_{i-n}^{raw}, \tag{4.36}$$

$$\dot{F}_n = \frac{1}{F^{norm}} \sum_{k=-N_h}^{N_h} \left(\frac{-1\phi k}{T_f} \right) H_k \sin\left(\frac{2\pi k n}{N_f} \right). \tag{4.37}$$

The parameters of the CRN filter in this study are:

$f_s =$ raw data sampling rate $= \frac{1}{30}$ Hz,

$N_c =$ number of self convolutions $= 7$,

$T_f =$ fit interval $= 5400$ sec (i.e., 180 points),

$B =$ target low-pass bandwidth $= 0.012$ Hz (corresponds to degree 60),

$f_0 =$ dominant signal frequency $= 0.00037$ Hz (corresponds to J2) ,

$N_B = BT_f =$ the number of frequency bins in the pass band,

$N_f = f_s T_f =$ the number of raw data points in the fit interval (odd integer).

4.9 Remove-Restore Method

In addition to all of the previous numerical differentiation methods, a remove-restore procedure was also implemented for each method. This procedure operates on the residual positions between the kinematic orbit and a reference orbit for the same day, which can be either dynamic or reduced-dynamic. This is accomplished in three steps:

1. Residual positions of kinematic orbit with respect to reference orbit are computed,

2. Residual velocities are computed from residual positions using the numerical methods discussed in this chapter,

3. In the restore step, the reference velocities are added back to the derived residual velocities to obtain the kinematic velocities.

This procedure was used with cubic smoothing splines for TUM-1S gravity model [32]. Note that including remove-restore means the kinematic orbit may no longer be independent of any *a priori* gravity field.

Chapter 5

Validation of Numerical Differentiation Methods

The first test of the numerical differentiation methods was to see how well they perform on dynamic and reduced-dynamic positions in reconstructing their velocities. While the behaviors of these orbits is different than a kinematic orbit, the velocities are known so it can set the baseline expectations.

First, the actual dynamic and reduced-dynamic positions and velocities are compared at a sampling interval of 30 sec in the body-fixed frame in order to mimic the kinematic orbit. Next, the velocities were derived numerically directly from the positions and compared to the actual dynamic and reduced-dynamic velocities. This included an error comparison and cross-comparison. In other words, the numerically derived dynamic velocities were compared to the actual dynamic velocities and the actual reduced-dynamic velocities and vice-versa for the numerically derived reduced-dynamic velocities.

The final experiment in this section is performed to determine the results of numerical methods used to derive the accelerations of the dynamic orbits. All of the results in this chapter are shown for a single test day for

brevity, though other days were tested to ensure that the main results are valid for any day. The selected test day was January 3, 2008, based on the quality of the kinematic orbit for this day, which will be detailed in the next chapter.

5.1 Orbit Comparison

The actual positions and velocities of the dynamic and reduced-dynamic orbits were compared for the test day as seen in Figures 5.1 and 5.2 as well as Tables 5.1 and 5.2. For this day the 3-D RMS of the position differences were 2.163 and 1.291 cm while the velocity differences were 0.0223 and 0.0141 mm/s for GRACE-A and B, respectively. This comparison was then carried out for the entire year of 2008. The result is shown in Figure 5.5. One can see that the differences in the positions vary from 1-2 cm in any direction which results in a 3-D RMS of 1 to 2.5 cm while the differences in the velocities are about 0.01-0.02 mm/s 3-D RMS. These statistics illustrate that the differences observed for the test day are typical.

The square root form of the power spectral density (PSD) of the differences are also included in Figures 5.1 and 5.1. Since, the time-variable gravity signal is mostly at the low degrees, i.e. around degree 30, the signal in the orbit of about 30 cycles per revolution. The static field gravity signal is at both low and high degrees, i.e. up to degree 180 or so. Therefore, the perturbation period of interest for the static field spans to approximately 30 seconds. With these frequency ranges in mind, the PSDs can be used to interpret how the numerical differentiation errors could worsen corresponding gravity solutions.

In addition, note that the RMS of a time-series is equal to a scaling of the square-root of the area under the PSD curve.

Table 5.1: Summary of Dynamic-Reduced Dynamic Position Differences for Test Day

	RMS of Residual [cm]	
Coordinate in Body-Fixed Frame	GRACE-A	GRACE-B
x	1.106	0.736
y	1.138	0.648
z	1.469	0.840
Position	2.163	1.291

Table 5.2: Summary of Dynamic-Reduced Dynamic Velocity Differences for Test Day

	RMS of Residual [mm/s]	
Coordinate in Body-Fixed Frame	GRACE-A	GRACE-B
x	0.0117	0.0085
y	0.0120	0.0087
z	0.0147	0.0070
Velocity	0.0223	0.0141

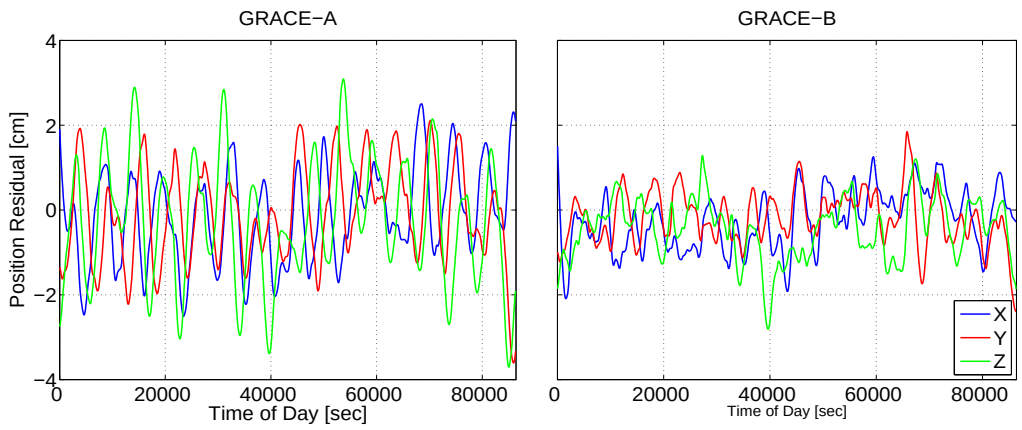

Figure 5.1: Dynamic-Reduced Dynamic Position Differences in Body-Fixed Frame

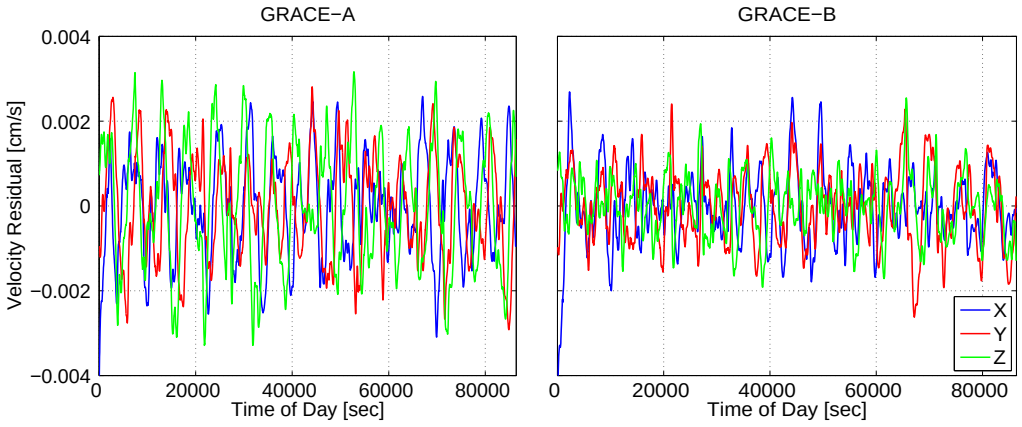

Figure 5.2: Dynamic-Reduced Dynamic Velocity Differences in Body-Fixed Frame

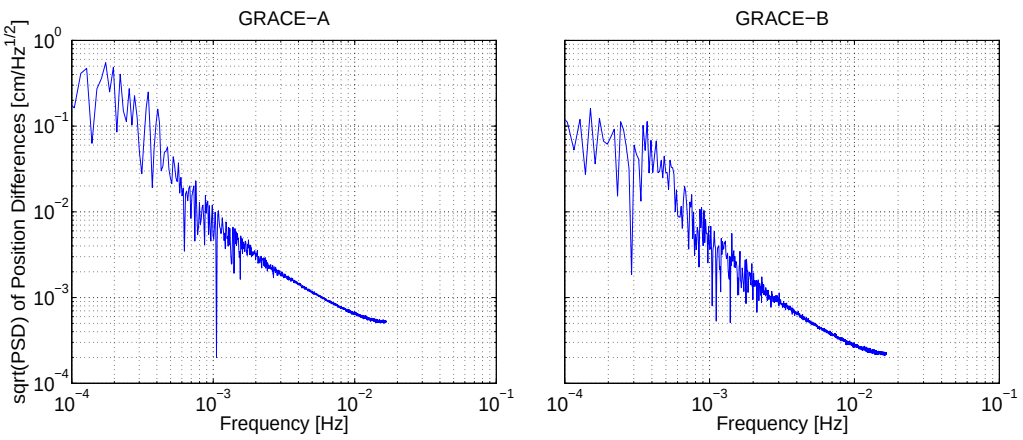

Figure 5.3: Dynamic-Reduced Dynamic Position Differences PSD

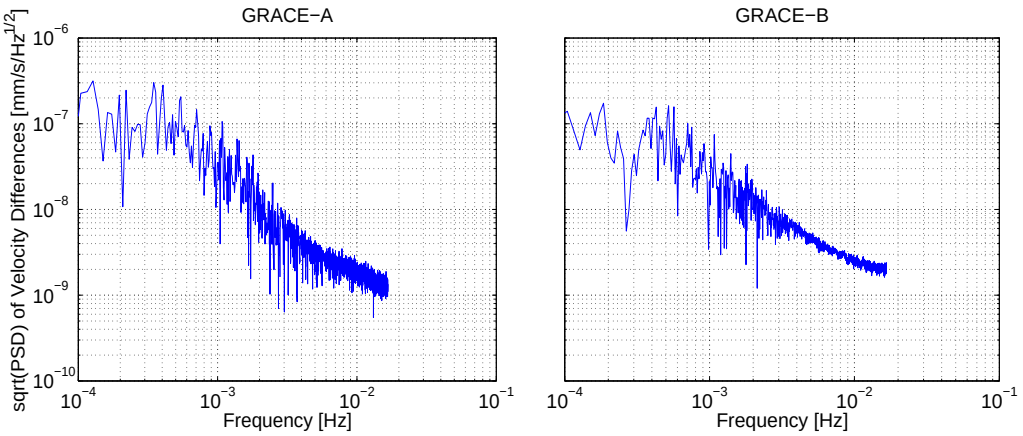

Figure 5.4: Dynamic-Reduced Dynamic Velocity Differences PSD

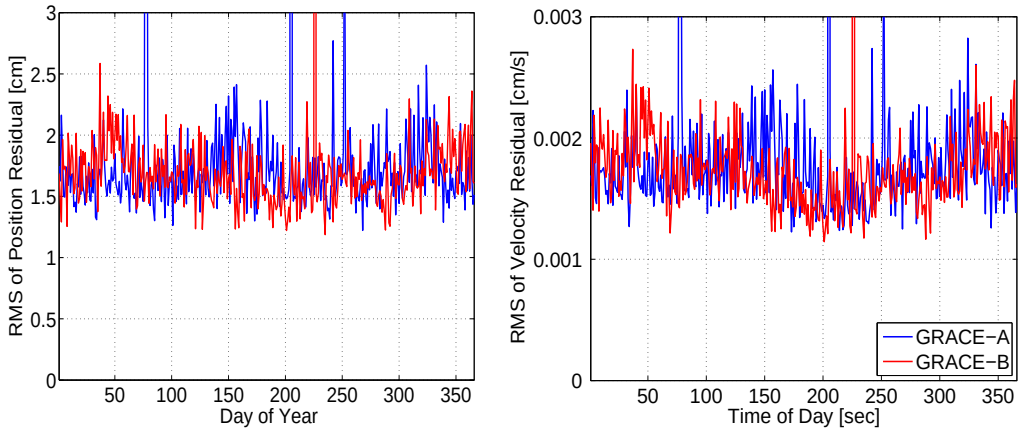

Figure 5.5: Daily 3-D RMS of Position and Velocity Differences for 2008

5.2 Validation of Numerical Velocities

5.2.1 Error Results

Since the velocities of the dynamic and reduced-dynamic orbits are known, the numerical differentiation methods were tested directly on the positions to see how well the velocities are reconstructed. In this case, the derived velocities are compared against the actual velocities for the specific orbit type. In other words, the derived dynamic velocities are compared to the actual dynamic velocities and the same for the reduced-dynamic velocities. The error should be zero if the numerical differentiation methods worked perfectly. However, this is not the case; the remaining error is 0.04 to 0.08 mm/s without remove-restore. The error results in this section show the limits of the numerical differentiation methods. The three best methods are Newton-Gregory interpolation, polynomial interpolation, and the CRN filter. The performance

of polynomial interpolation is expected based on the smooth behavior of dynamic orbits. When remove-restore is used, the opposite orbit type is used as the reference orbit. For example, when deriving the dynamic velocities using remove-restore, the reduced-dynamic orbit is used as the reference orbit. Also, the results of using the three best methods with remove-restore were approximately the same, so only one result is shown in Table 5.3 (i.e., the last row).

Table 5.3: Dynamic Velocity Error

	RMS of Error [mm/s]	
Technique	GRACE-A	GRACE-B
Hermite Interpolation	1.759	1.759
Cubic Spline Interpolation	0.0794	0.0794
Polynomial Fitting	0.0413	0.0413
Newton-Gregory Interpolation	0.0414	0.0414
Cubic Smoothing Splines	0.0794	0.0794
Savitzky-Golay Filter	0.0498	0.0499
CRN Filter	0.0412	0.0412
Remove-Restore	0.0040	0.0040

Table 5.4: Reduced-Dynamic Velocity Error

	RMS of Error [mm/s]	
Technique	GRACE-A	GRACE-B
Hermite Interpolation	1.758	1.759
Cubic Spline Interpolation	0.0817	0.0817
Polynomial Fitting	0.0446	0.0446
Newton-Gregory Interpolation	0.0447	0.0447
Cubic Smoothing Splines	0.0817	0.0817
Savitzky-Golay Filter	0.0526	0.0526
CRN Filter	0.0445	0.0445
Remove-Restore	0.0040	0.0040

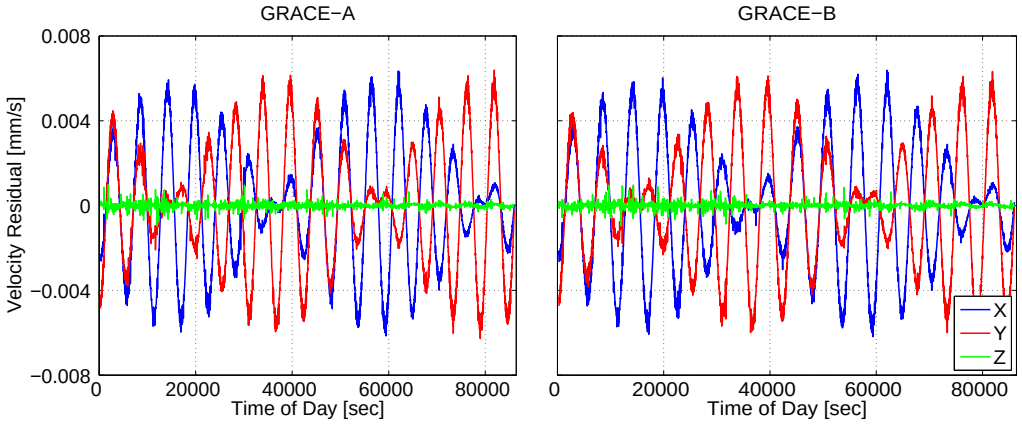

Figure 5.6: Dynamic Velocity Errors using Remove-Restore

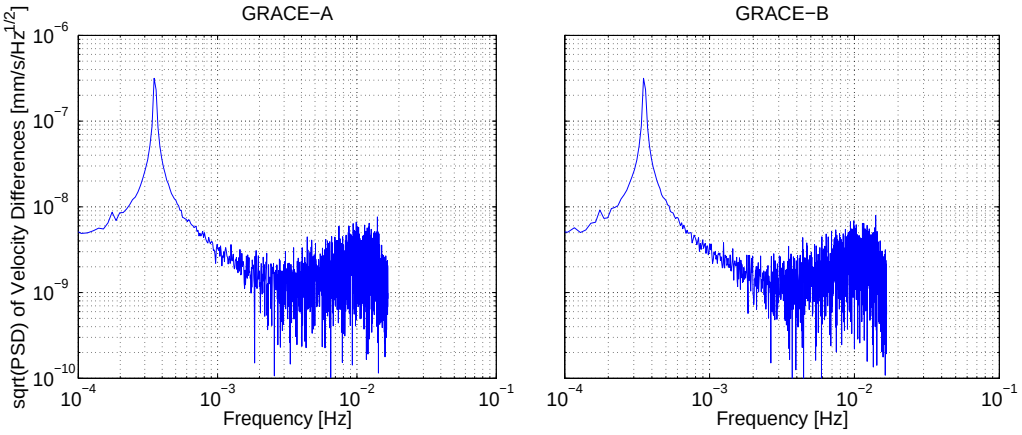

Figure 5.7: Dynamic Velocity Error PSD using Remove-Restore

5.2.2 Cross-comparison Results

The next comparison of the results is aimed to set the expectations for the kinematic velocities. In this case, the derived velocities are compared to the opposite orbit type. The differences between the derived dynamic velocities and actual reduced-dynamic velocities are computed, and the differences between the derived reduced-dynamic velocities and actual dynamic velocities are computed. This is useful since the kinematic velocities will be compared to the dynamic and reduced-dynamic velocities. The cross comparison results show that RMS of the velocity residuals are about 0.05 to 0.08 mm/s without remove-restore and 0.01 to 0.02 mm/s with remove-restore. If remove-restore is not used, then the numerical methods introduce noise significantly larger than the inherent differences between the orbits which was 0.01 to 0.02 mm/s. This shows that the use of remove-restore is necessary to match the

limits of agreement between the actual dynamic and reduced-dynamic velocities. Similar to the error results, the three best methods are Newton-Gregory interpolation, polynomial interpolation, and the CRN filter.

Table 5.5: Derived Dynamic-Actual Reduced Dynamic Velocity Residuals

	RMS of Residual [mm/s]	
Technique	GRACE-A	GRACE-B
Polynomial Fitting	0.0459	0.0459
Newton-Gregory Interpolation	0.0460	0.0466
CRN Filter	0.0451	0.0457
Remove-Restore	0.0221	0.0130

Table 5.6: Derived Reduced Dynamic-Actual Dynamic Velocity Residuasl

	RMS of Residual [mm/s]	
Technique	GRACE-A	GRACE-B
Polynomial Fitting	0.0435	0.0434
Newton-Gregory Interpolation	0.0505	0.0506
CRN Filter	0.0508	0.0437
Remove-Restore	0.0221	0.0130

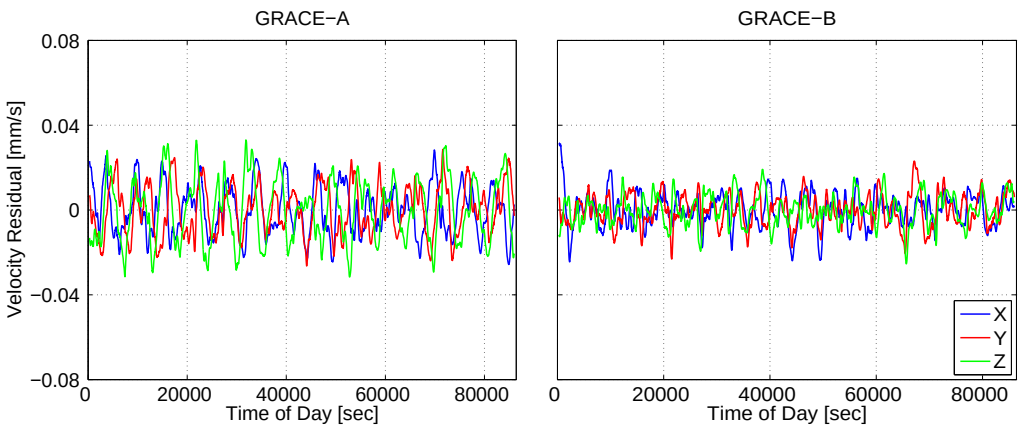

Figure 5.8: Derived Dynamic-Actual Reduced Dynamic Velocity Residuals using Remove-Restore

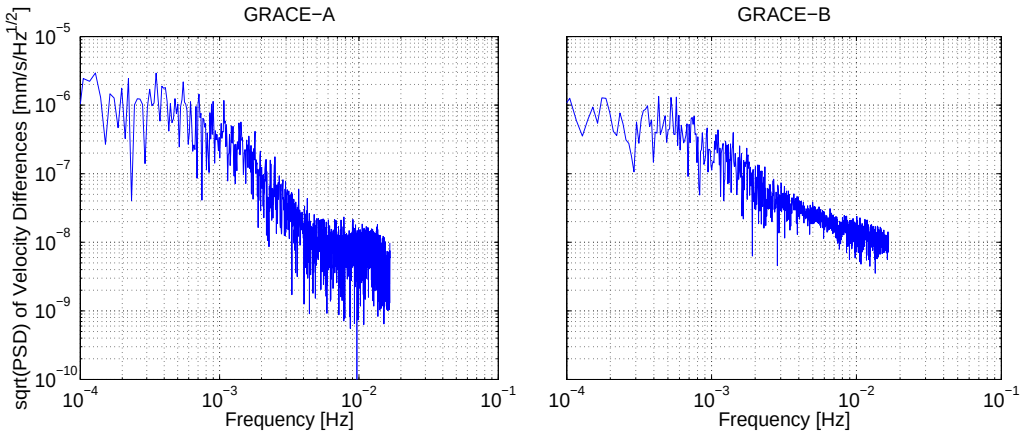

Figure 5.9: Derived Dynamic-Actual Reduced Dynamic Velocity Residuals PSD using Remove-Restore

The results of this section show that when the orbit positions differ by 11 mm, the velocities differ by 10-12 micron/sec. This is a proportionality of about 1:1000, which corresponds to the mean motion (about 1 milliRad/sec).

The floor set by the remove-restore is lower than this, at around 4 micron/sec. In the cross-comparison case, it takes remove-restore to achieve numbers closer to the orbit differences, around 13-20 micron/sec. A comparison of the PSDs in Figure 5.10 show that the remove-restore cross-comparison velocity results are slightly noisier than the inherent velocity differences between the dynamic and reduced-dynamic orbits.

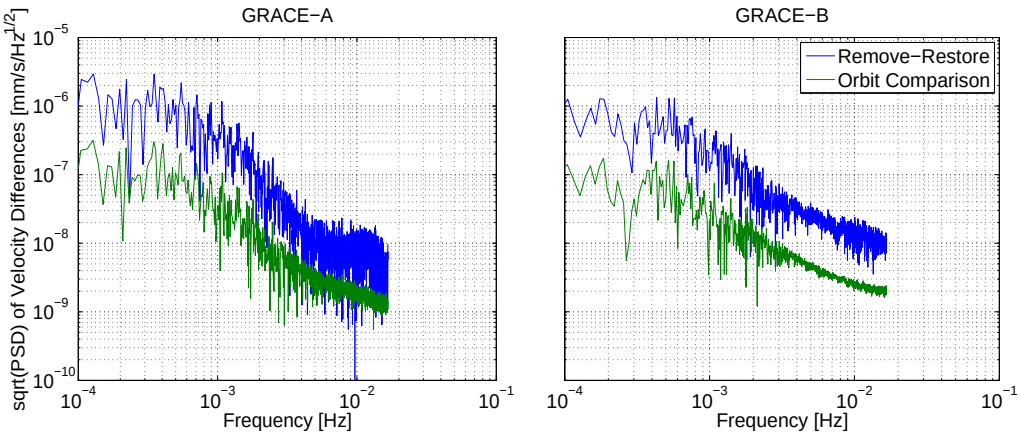

Figure 5.10: Orbit Comparison and Remove-Restore Velocity PSD

5.3 Accelerations

The final experiment in this chapter tested the performance of the numerical differentiation methods when deriving accelerations. In the dynamic POD processing within MSODP, the accelerations in the J2000 frame are written out into a file every time the integrator calls the force evaluation routine, which is nominally every 5 seconds. This set of accelerations was used as the reference against which the numerically derived dynamic and reduced-

dynamic accelerations were compared.

The three best methods from the previous section were used to derive accelerations from the dynamic and reduced-dynamic orbits. This was performed three different ways. The first involved deriving the accelerations directly from the dynamic and reduced-dynamic velocities at a 5 second sampling rate. The second method used the velocities at a 30 second sampling rate. Finally, the accelerations were derived from from the dynamic and reduced-dynamic positions at a 30 second sampling rate in order to approximate the kinematic orbits. Note that this method uses different formulations of the algorithms in Chapter 4 than those used to derive the velocities (with the exception of Newton-Gregory interpolation which was applied twice successively to the positions).

The 3-D RMS differences of the accelerations from Newton-Gregory interpolation and polynomial interpolation with the integrator output accelerations are 0.099 and 0.15 nm/s^2 (i.e. $nanometers/s^2$) for dynamic orbits. The reduced-dynamic residuals are approximately 0.27 $\mu m/s^2$ (i.e., $micrometers/s^2$) for each method. It is not surprising that the derivatives of the reduced-dynamic velocities do not compare as well to the reference accelerations since those were created during the dynamic orbit processing.

Table 5.7: Derived Dynamic Acceleration Differences using Velocities at 5 sec sampling

	RMS of Residual [nm/s^2]	
Technique	GRACE-A	GRACE-B
Newton-Gregory Interpolation	0.0991	0.0937
Polynomial Interpolation	0.1546	0.1498
CRN Filter	0.2467	0.2408

Table 5.8: Derived Reduced Dynamic Acceleration Differences using Velocities at 5 sec sampling

	RMS of Residual [μm/s^2]	
Technique	GRACE-A	GRACE-B
Newton-Gregory Interpolation	0.2719	0.2735
Polynomial Interpolation	0.2715	0.2731
CRN Filter	0.2721	0.2737

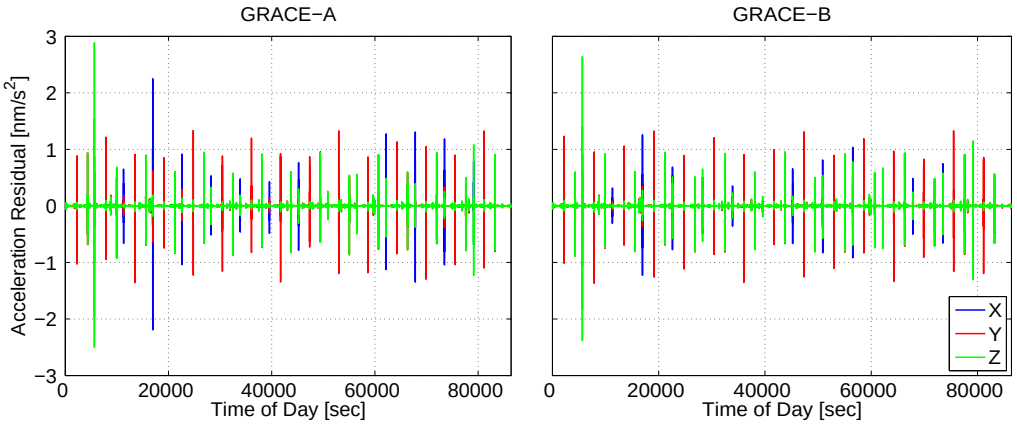

Figure 5.11: Derived Dynamic Acceleration Differences using Newton-Gregory Interpolation from Velocities at 5 sec sampling

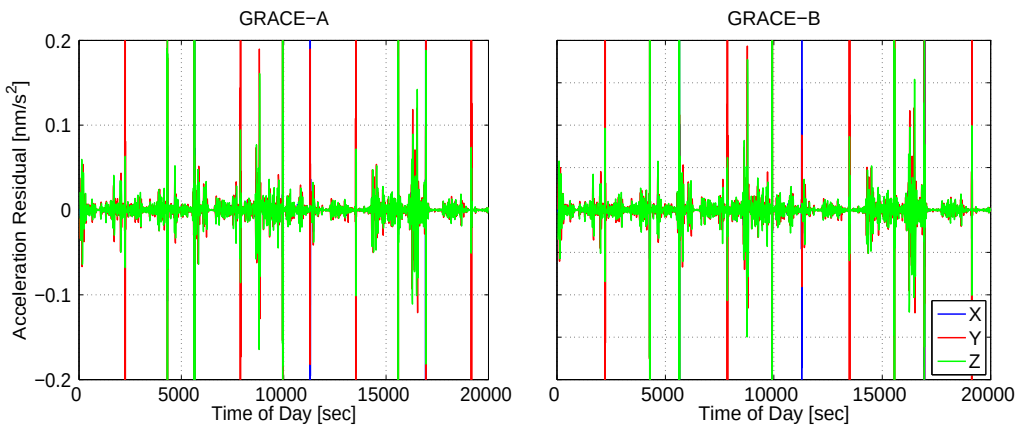

Figure 5.12: Derived Dynamic Acceleration Differences using Newton-Gregory Interpolation (Zoomed)

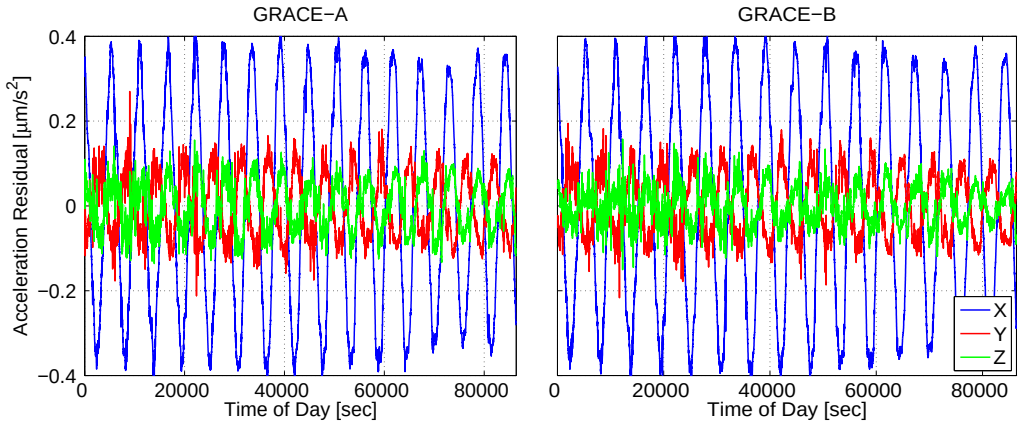

Figure 5.13: Derived Reduced Dynamic Acceleration Differences using Polynomial Interpolation from Velocities at 5 sec sampling

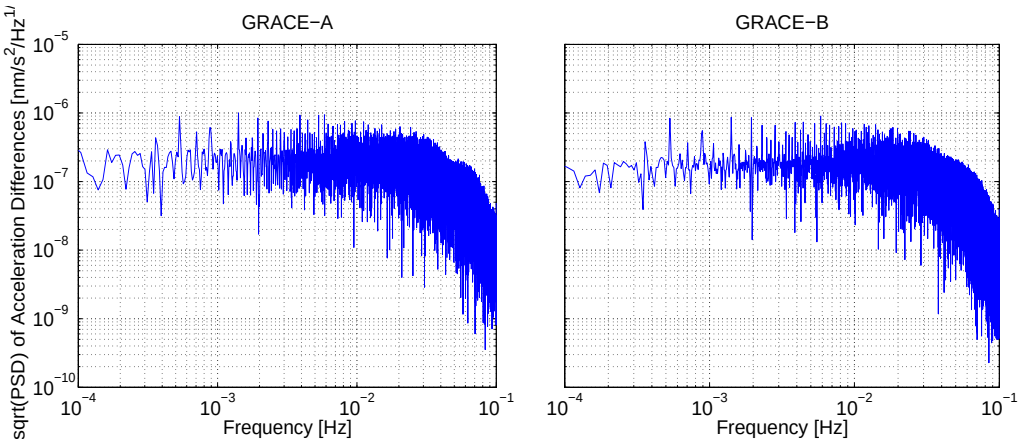

Figure 5.14: Derived Dynamic Acceleration Differences PSD using Newton-Gregory Interpolation from Velocities at 5 sec sampling

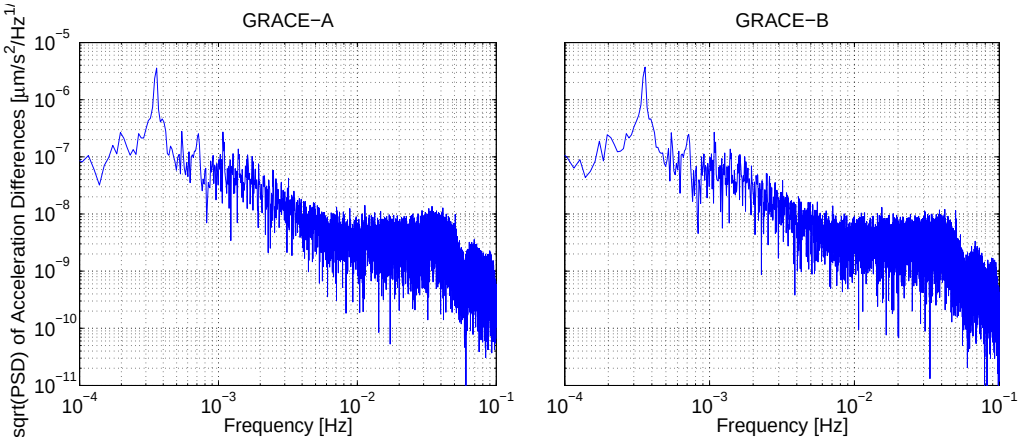

Figure 5.15: Derived Reduced Dynamic Acceleration Differences PSD using Polynomial Interpolation from Velocities at 5 sec sampling

Next, in order to more closely simulate the kinematic orbits, the accelerations were derived directly from positions at 30 second intervals. Therefore, the results from this case can be used to set the expectations for the kinematic

accelerations. The only significant conclusion that can be drawn is that one cannot expect to do much better than 3 μm/s^2 difference for the kinematic case.

Table 5.9: Derived Dynamic Acceleration Differences from Positions at 30 sec sampling

	RMS of Residual [μm/s^2]	
Technique	GRACE-A	GRACE-B
Newton-Gregory Interpolation	0.5078	0.5095
Polynomial Interpolation	0.3854	0.3855
CRN Filter	0.7056	0.7081

Table 5.10: Derived Reduced Dynamic Acceleration Differences from Positions at 30 sec sampling

	RMS of Residual [μm/s^2]	
Technique	GRACE-A	GRACE-B
Newton-Gregory Interpolation	3.372	3.375
Polynomial Interpolation	2.979	2.977
CRN Filter	3.063	3.066

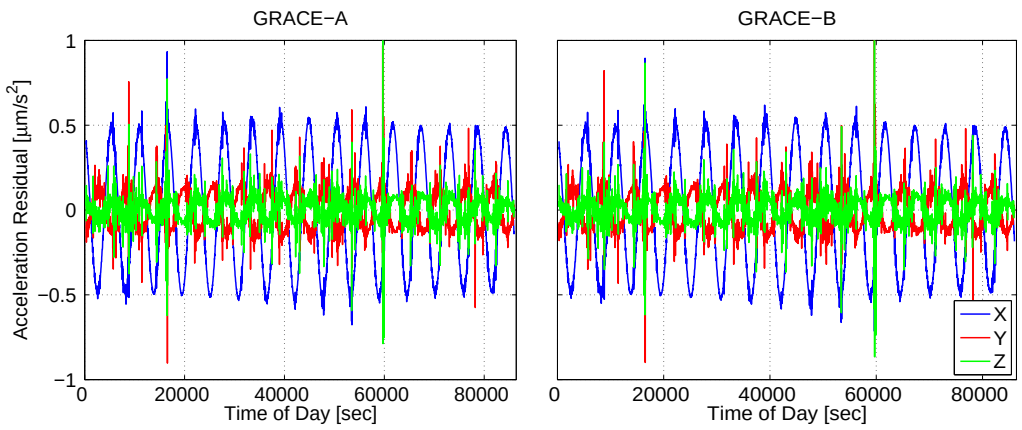

Figure 5.16: Derived Acceleration Differences using Polynomial Interpolation on Dynamic Positions at 30 sec sampling

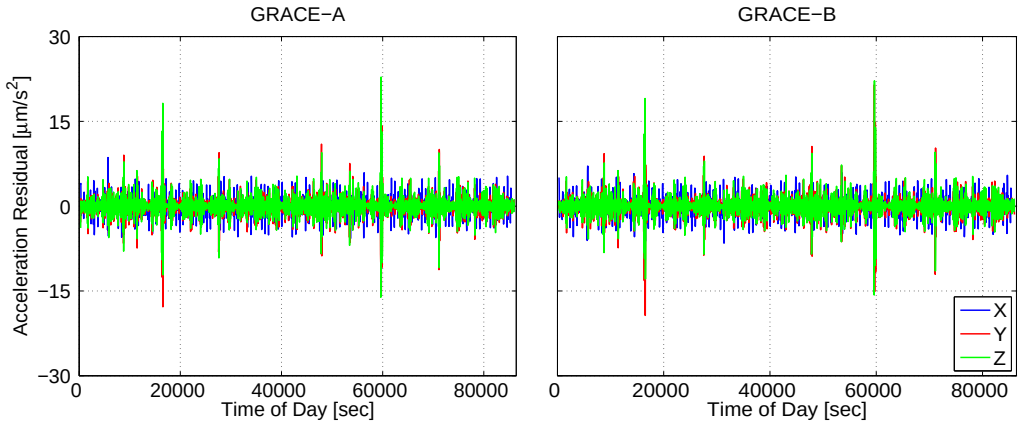

Figure 5.17: Derived Acceleration Differences using Polynomial Interpolation on Reduced-Dynamic Positions at 30 sec sampling

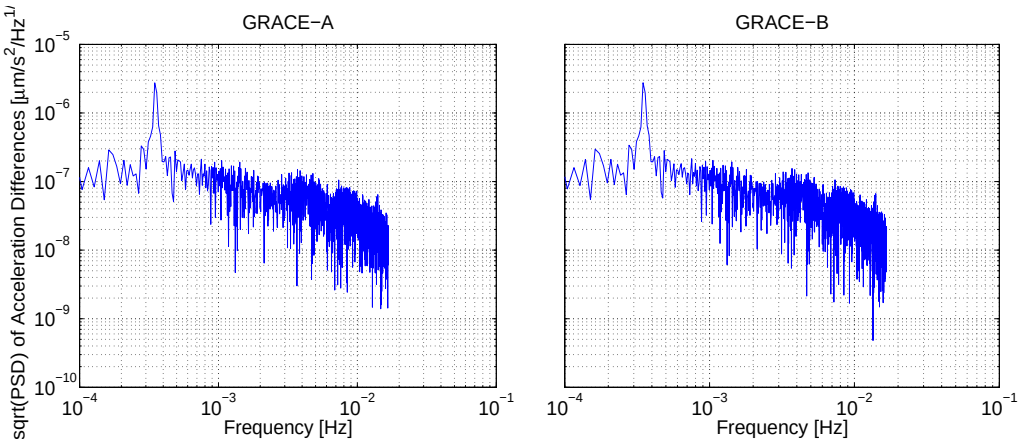

Figure 5.18: Derived Acceleration Differences PSD using Polynomial Interpolation on Dynamic Positions at 30 sec sampling

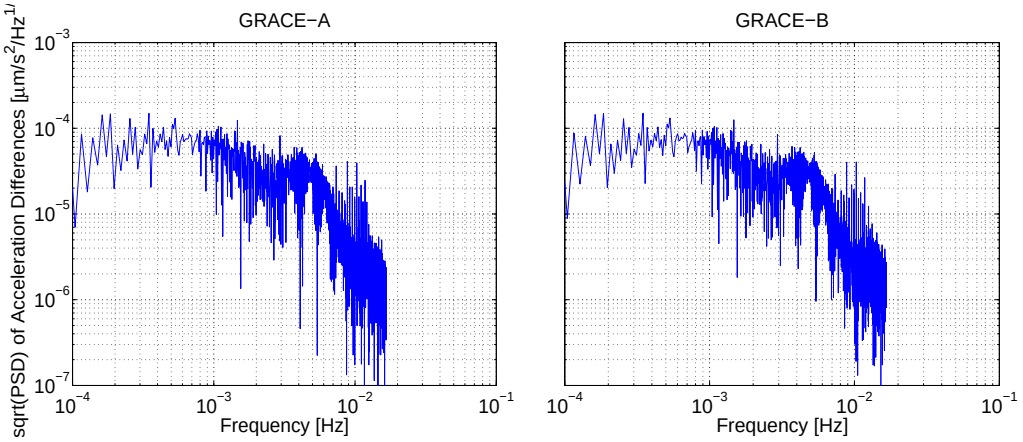

Figure 5.19: Derived Acceleration Differences PSD using Polynomial Interpolation on Reduced-Dynamic Positions at 30 sec sampling

As an extra validation step, the accelerations were derived from velocities at 30 second intervals. These results also showed degraded performance from downsampling. In this case, the dynamic and reduced-dynamic results

become roughly the same now. Recall that at 5 sec sampling, the dynamic accelerations were in units of nm/s^2 and are now in units of μ/s^2.

5.3.1 Remove-Restore

The implementation of the remove-restore technique for deriving accelerations is slightly different than deriving velocities. For that case, a reference solution of "truth" positions and velocities was used to derive the velocities directly from a different set of only positions. For accelerations, a reference set of positions, velocities, and accelerations is needed. This is contained in the integrator output from the dynamic orbit processing within MSODP. This means that the remove-restore technique can only be used to derive reduced-dynamic accelerations; it cannot be used to improve the dynamic acceleration results. With remove-restore, the results improve slightly as seen in Table 5.11, which includes the results for polynomial interpolation. Note that only the 30 second sampling cases are shown; the 5 second case did not improve with remove-restore.

Table 5.11: Reduced-Dynamic Acceleration Differences using Polynomiail Interpolation with Remove-Restore

	RMS of Residual [μm/s^2]	
Technique	GRACE-A	GRACE-B
Velocity Input	0.2801	0.2817
Position Input	1.3896	1.3896

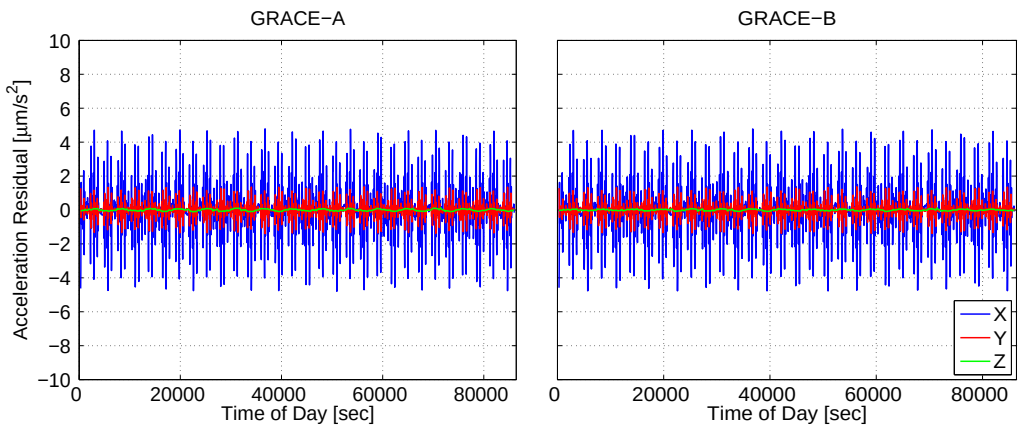

Figure 5.20: Derived Acceleration Differences using Polynomial Interpolation with Remove-Restore on Reduced-Dynamic Positions at 30 sec sampling

5.4 Summary

In this chapter, several numerical differentiation methods were tested for their performance on traditional (i.e., dynamic and reduced-dynamic) POD solutions. First, the positions were differentiated and compared to the known velocities. In other words, dynamic positions were differentiated and compared to the known dynamic velocities. This was repeated for the reduced-dynamic case. The three best methods are Newton-Gregory interpolation, polynomial interpolation, and the CRN filter. The errors were on the order of 0.04 to 0.08 mm/s without remove-restore and 0.004 mm/s using remove-restore. When remove-restore is used, the opposite orbit type was used as the reference orbit.

Next, the cross-comparison results were analyzed. In this case, the numerically obtained velocities were compared to the known velocities of the

opposite orbit type. The differences between the derived dynamic velocities and actual reduced-dynamic velocities were computed as well as the differences between the derived reduced-dynamic velocities and actual dynamic velocities. The cross comparison residuals had a RMS of about 0.05 mm/s without remove-restore and 0.01 to 0.02 mm/s with remove-restore. If remove-restore is not used, then the numerical methods introduce noise significantly larger than the inherent differences between the orbits. This shows that the use of remove-restore is necessary to match the limits of agreement between the actual dynamic and reduced-dynamic velocities. Similar to the error results, the three best methods were Newton-Gregory interpolation, polynomial interpolation, and the CRN filter. Note that with remove-restore, the "best-case" velocity errors satisfy the requirements for gravity recovery up to degree and order 30 in Chapter 3.

The final section in this chapter tested the methods in determining dynamic accelerations. The results were compared to accelerations provided by the integrator output from processing the dynamic orbits. When tested directly on the dynamic and reduced-dynamic velocities sampled every 5 seconds, the three best methods from the previous section the derived accelerations compare well to the integrator output (i.e., 3-D RMS of 0.09 to 0.15 nm/s^2). In order to simulate the kinematic orbit case, the accelerations were derived using only dynamic positions sampled every 30 seconds. The results were much worse, on the order of 0.35 $\mu m/s^2$. From this result, it is clear that a 30 second sampling rate will present issues in deriving the kinematic

accelerations.

Overall, this chapter sets the expectations for the kinematic velocity results. Since the kinematic positions differences between the dynamic and reduced-dynamic orbits are expected to be higher than 2.5 cm, the numerical kinematic velocities cannot be any better than the results shown in this chapter.

Chapter 6

Kinematic Results

6.1 Editing of Kinematic Orbits

After the kinematic POD process, the resulting solution still has anomalous points. These are typically caused by poor geometry between the LEO GPS receiver and the GPS satellites, which can cause a loss of phase connection. The standard editing procedure is to compute the kinematic positions differences between two successive epochs with the positions from a dynamic or reduced dynamic orbit [29]. In this study, points where the differences exceed a certain threshold are flagged. These points are not rejected since the numerical differentiation methods require an equally spaced discrete data set. The points are instead corrected through polynomial interpolation using 8 points. These are not points immediately neighboring the "bad" point but rather several points away in order to reduce the effect of consecutive "bad" points. An alternative approach would be to create a new arc, however, this was not implemented in this study. The unedited and edited kinematic minus dynamic position residuals for the test day are shown in Tables 6.1 and 6.2, respectively. These flagged points can be discarded in subsequent spherical harmonic analysis. Note that the test day was selected as January 3, 2008 due to the quality of the kinematic orbits available. In this case, four points were

edited for GRACE-A, and 8 points were edited for GRACE-B.

Table 6.1: Unedited Kinematic-Dynamic Position Residuals

	RMS of Residual [cm]	
Coordinate in Body-Fixed Frame	GRACE-A	GRACE-B
x	2.385	2.153
y	2.261	2.065
z	2.919	14.66
Position	4.396	14.96

Table 6.2: Edited Kinematic-Dynamic Position Residuals

	RMS of Residual [cm]	
Coordinate in Body-Fixed Frame	GRACE-A	GRACE-B
x	2.374	2.017
y	2.258	1.941
z	2.621	1.988
Position	4.196	3.434

6.2 Comparison with Dynamic and Reduced-Dynamic Positions

With the editing procedure in place, the kinematic positions are compared to the dynamic and reduced-dynamic positions. In these results, the edited points from the previous step are ignored in the RMS calculations. Tables 6.3 and 6.4 include the differences after the editing procedure. One can see that the residuals are greater than the dynamic versus reduced-dynamic positions from the previous chapter, which was 1 to 2.5 cm. In this case, the 3-D RMS of the position differences is 3 to 4 cm. The limiting factor in these

results is the "bad" points. Even after the editing procedure, some anomalous points can easily be spotted within the z-direction in the position plots at around 55,000 and 84,000 seconds of day for GRACE-A and 20,000 and 55,000 seconds for GRACE-B. This will have an important impact on the numerical methods for obtaining kinematic velocities.

Table 6.3: Kinematic-Dynamic Position Residuals

	RMS of Residual [cm]	
Coordinate in Body-Fixed Frame	GRACE-A	GRACE-B
x	2.374	2.017
y	2.258	1.941
z	2.621	1.988
Position	4.196	3.434

Table 6.4: Kinematic-Reduced Dynamic Position Residuals

	RMS of Residual [cm]	
Coordinate in Body-Fixed Frame	GRACE-A	GRACE-B
x	2.299	2.111
y	2.107	1.872
z	2.515	2.080
Position	4.007	3.505

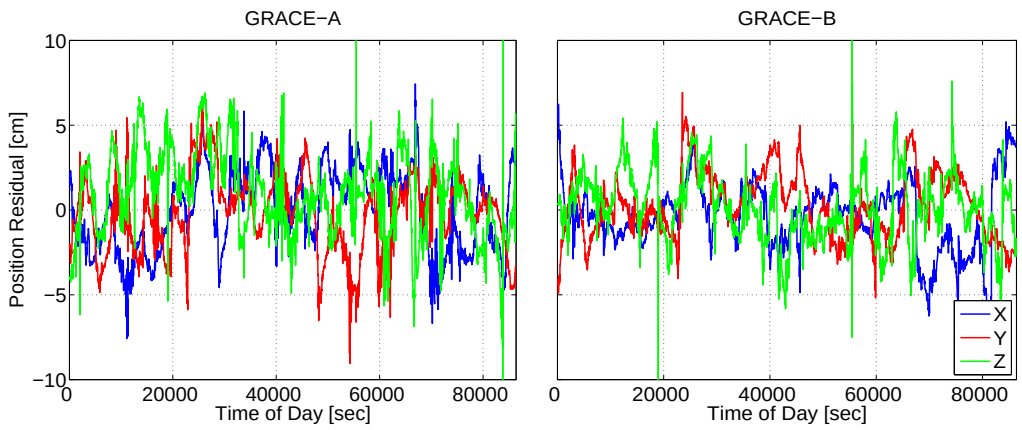

Figure 6.1: Kinematic-Dynamic Position Differences in Body-Fixed Frame

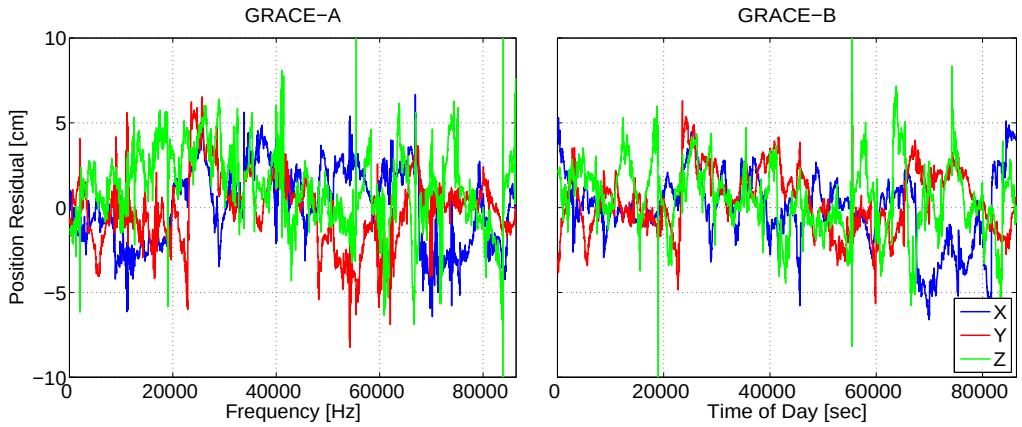

Figure 6.2: Kinematic-Reduced Dynamic Position Differences in Body-Fixed Frame

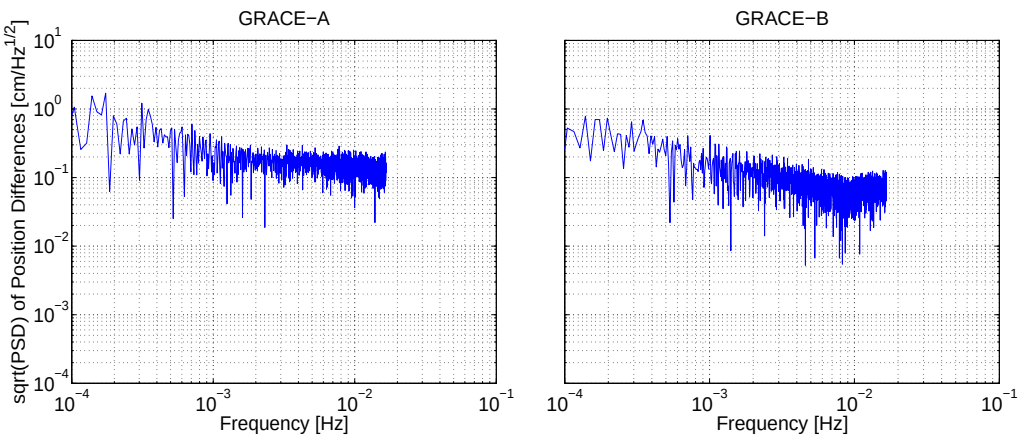

Figure 6.3: Kinematic-Dynamic Position Differences PSD

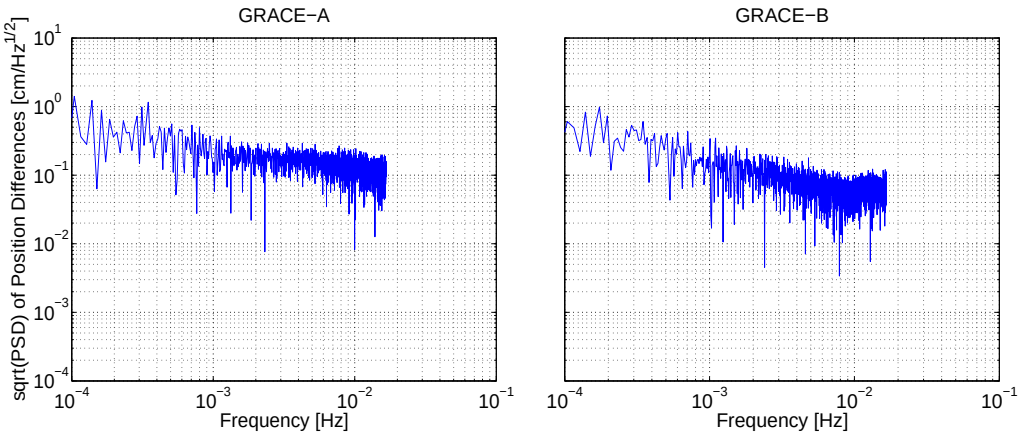

Figure 6.4: Kinematic-Reduced Dynamic Position Differences PSD

6.3 Numerically Derived Velocities

6.3.1 Comparison with Dynamic and Reduced-Dynamic Velocities

The kinematic velocities were computed directly from the kinematic positions in the body-fixed frame using the various numerical methods. The

results were compared to the independent dynamic and reduced-dynamic velocities. The differences with these reference velocities to provide an indication of which methods perform the best. However, it should be noted that the derived kinematic velocities with a relatively high RMS differences to a reference orbit may not necessarily imply a bad solution for gravity field analysis.

Table 6.5: Kinematic-Dynamic Velocity Residual

	RMS of Residual [mm/s]	
Technique	GRACE-A	GRACE-B
Newton-Gregory Interpolation	0.3554	0.2411
Savitzky-Golay Filter	0.2106	0.1600
CRN Filter	0.3550	0.2438

Table 6.6: Kinematic-Reduced Dynamic Velocity Residual

	RMS of Residual [mm/s]	
Technique	GRACE-A	GRACE-B
Newton-Gregory Interpolation	0.3548	0.2418
Savitzky-Golay Filter	0.2097	0.1610
CRN Filter	0.3545	0.2444

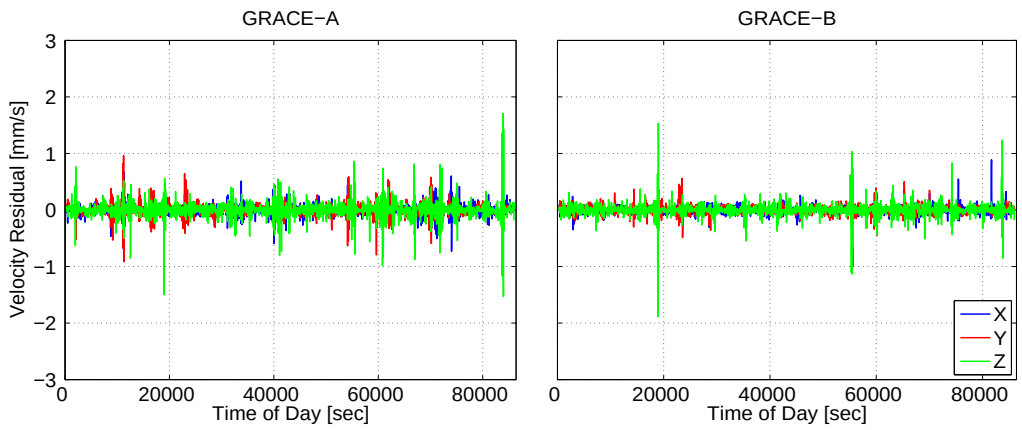

Figure 6.5: Kinematic-Dynamic Velocity Residuals for Savitzky-Golay Filter

Newton-Gregory interpolation, Savitzky-Golay filter, and CRN filter performed the best in this comparison. This was expected based on the results from the previous chapter. In this case, polynomial interpolation is replaced by the Savitzky-Golay filter. This can be explained by the noise in the kinematic positions and that the Savitzky-Golay filter is a method of polynomial interpolation used for smoothing noisy data. The differences with the dynamic and reduced-dynamic velocities vary from 0.2 to 0.4 mm/s RMS, which is consistent with the literature on CHAMP [32]. However, this is contrary to the expectations set by the previous chapter. For orbit position differences of 20 to 40 mm, the velocity differences were expected to be 20 to 40 μ/s. The limiting factor for these results are the edited points that were observed in the position comparison from the previous section. Inspecting a zoomed-in section of Figure 6.5, the statistics are much closer to the expectations with a 3-D RMS of 80 μ/s (Figure 6.6).

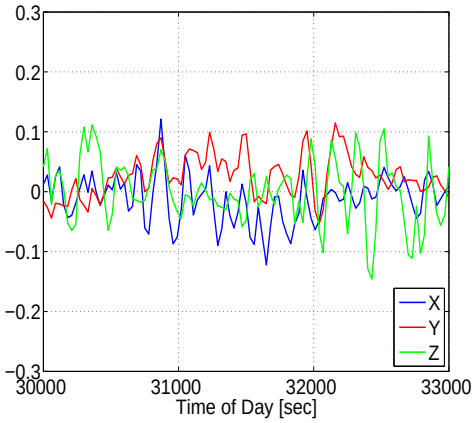

Figure 6.6: GRACE-B Kinematic-Dynamic Velocity Residuals (Zoomed)

6.3.2 Using Remove-Restore

The results from the previous section are now reanalyzed using the remove-restore method. For this study the reference orbit was the same as the compared orbit. In other words, when the dynamic orbit is used to compute the kinematic velocities, the results are only shown compared to dynamic velocities.

The remove-restore results are very interesting. The solution is greatly improved for the simple central difference method. While the RMS differences are slightly better for the GRACE-A results than when no reference orbit is used, this is not the case for the GRACE-B results. Upon further investigation, this is caused by the edited points. The introduction of a reference orbit worsens the solution at these points which also causes worse performance at the neighboring points. Therefore, for the kinematic orbits, if the use of remove-

restore method is desired, then these points should not be included in the numerical differentiation process. Recall that the methods require a constant sampling interval. One method to resolve this is to break the day-long solution into arcs around these "bad" points. However, this topic was not considered in this study in order to preserve 24-hour batch solutions. Additionally, breaking the orbit into arcs introduces error since the numerical differentiation methods require a few points at the beginning and end to converge. In summary, based on the studies in this chapter, the Savtizky-Golay filter should be used without remove-restore to derive the velocities for kinematic orbits.

Table 6.7: Kinematic-Dynamic Velocity Residual using Remove-Restore

	RMS of Residual [mm/s]	
Technique	GRACE-A	GRACE-B
Central Difference Method	0.2372	0.2088
Newton-Gregory Interpolation	0.3524	0.2981
Savitzky-Golay Filter	0.2034	0.1838
CRN Filter	0.3521	0.3124

Table 6.8: Kinematic-Reduced Dynamic Velocity Residual using Remove-Restore

	RMS of Residual [mm/s]	
Technique	GRACE-A	GRACE-B
Central Difference Method	0.2375	0.2089
Newton-Gregory Interpolation	0.3536	0.2981
Savitzky-Golay Filter	0.2032	0.1839
CRN Filter	0.3685	0.3109

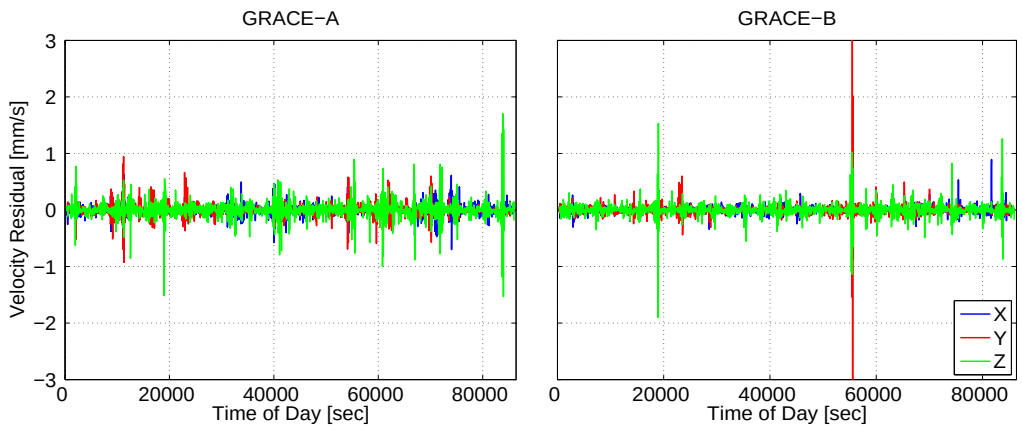

Figure 6.7: Kinematic-Dynamic Velocity Residuals for Savitzky-Golay Filter using Remove-Restore

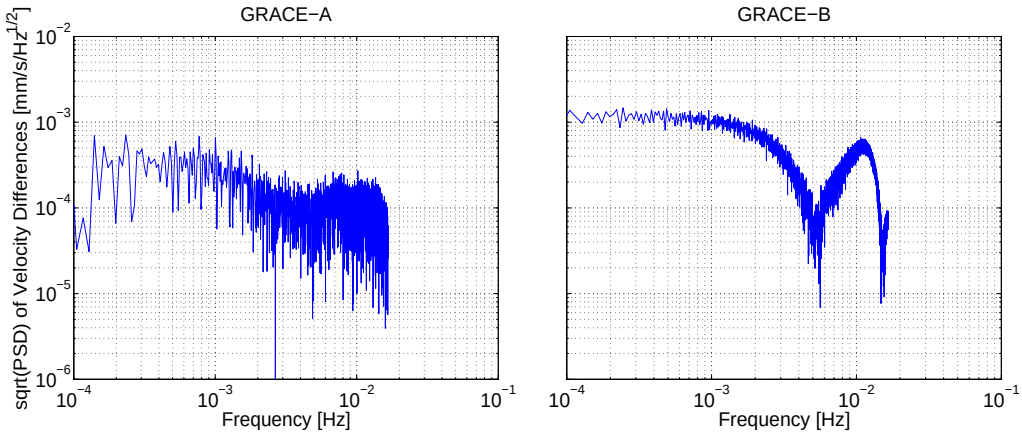

Figure 6.8: Kinematic-Dynamic Velocity Residuals PSD for Savitzky-Golay Filter using Remove-Restore

6.4 Accelerations

The kinematic accelerations are of particular importance in regards to gravity field recovery. Recall that the dynamic orbit represents the motion

due to the gravity modeling that was included during the POD (i.e., the RL05 processing environment). The position, velocity, and accelerations under these influences are known. On the other hand, the kinematic orbit is representative of the total motion under all accelerations. This includes accelerations that were modeled for the dynamic orbits as well as all unmodeled accelerations. Therefore, if the kinematic accelerations are known accurately enough, the differences between them and the dynamic accelerations could provide insight into unmodeled gravity forces.

The kinematic accelerations were derived using the three best methods, with and without remove-restore. These were derived directly from the kinematic positions. While not shown here, the derivation to get accelerations directly from positions follows the procedures given in Chapter 4. Additionally, the accelerations were derived from the best numerical velocities (i.e., the Savitzky-Golay results from the previous section), however, the results did not improve.

Table 6.9: Derived Kinematic Acceleration Differences from Positions

	RMS of Residual $[\mu m/s^2]$	
Technique	GRACE-A	GRACE-B
Newton-Gregory Interpolation	17.42	10.83
Savitzky-Golay Filter	5.627	4.426
CRN Filter	23.62	20.14

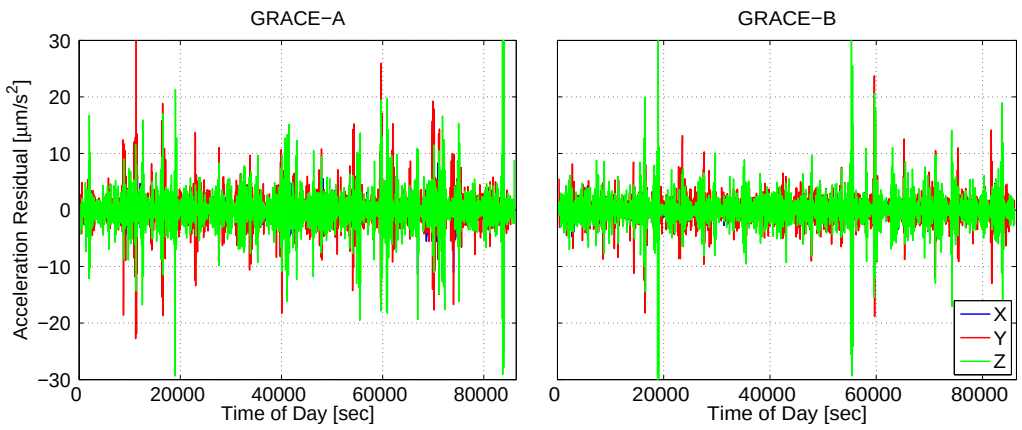

Figure 6.9: Derived Kinematic Acceleration Differences using Savitzky-Golay Filter on Positions

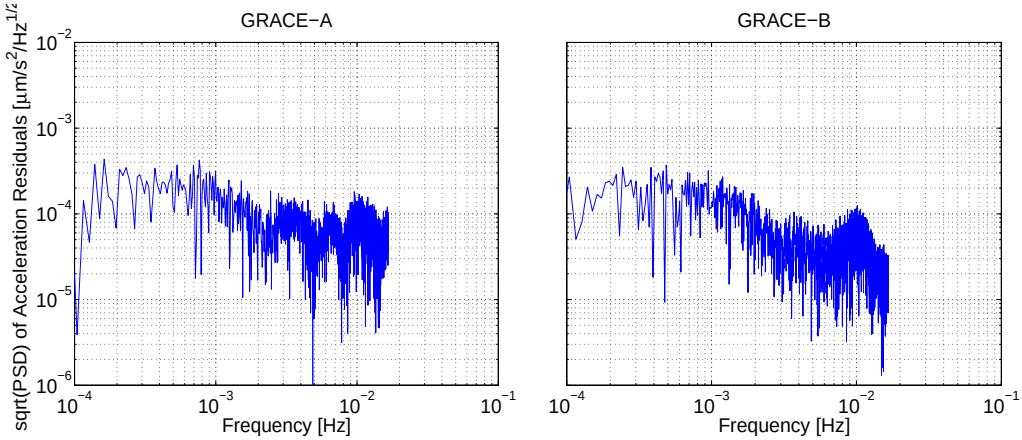

Figure 6.10: Kinematic Acceleration Differences PSD using Savitzky-Golay Filter on Positions

6.4.1 Remove-Restore

In these results the "truth" dynamic positions, velocities, and accelerations from the dynamic orbit processing at CSR were used as the reference

solution in the same way as the previous chapter. The results show slight improvement over the acceleration results without remove-restore.

Table 6.10: Kinematic Acceleration Differences using Savitzky-Golay Filter with Remove-Restore

	RMS of Residual [μm/s^2]	
Technique	GRACE-A	GRACE-B
Velocity Input	4.750	3.541
Position Input	5.311	3.982

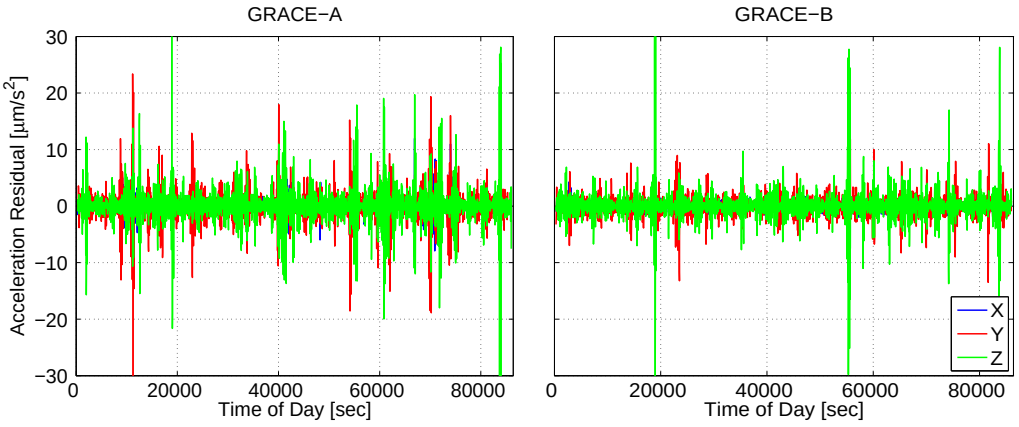

Figure 6.11: Derived Acceleration Differences using Savitzky-Golay Filter with Remove-Restore on Kinematic Positions at 30 sec sampling

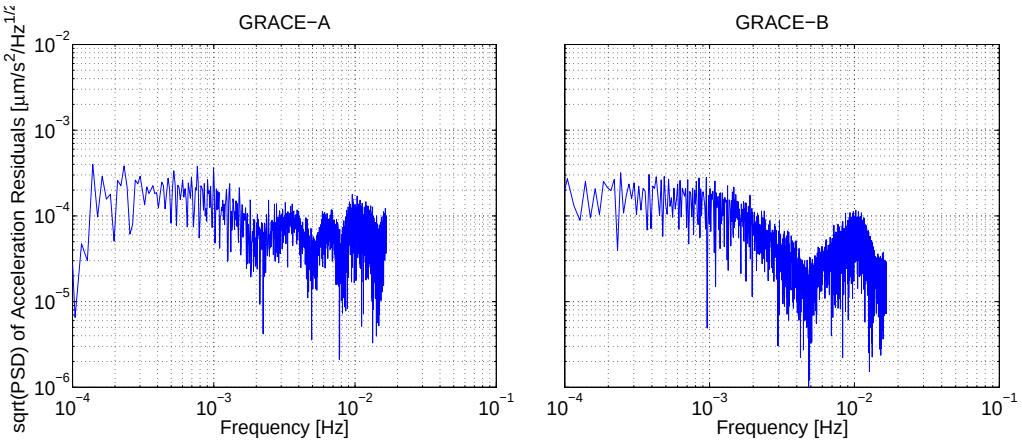

Figure 6.12: Derived Acceleration Differences PSD using using Savitzky-Golay Filter with Remove-Restore on Kinematic Positions at 30 sec sampling

6.5 Summary

In this chapter, the best numerical differentiation methods from the previous chapter were tested on kinematic POD solutions. Before this could be accomplished, an editing procedure was implemented to remove anomalous points. Next, since the kinematic velocities are unknown, only the cross comparison results of the numerical differentiation were analyzed. In other words, kinematic positions were differentiated and compared to the known dynamic and reduced-dynamic velocities. The three best methods proved to be Newton-Gregory interpolation, the Savitzky-Golay filter, and the CRN filter. The RMS of the residuals varied from 0.2 to 0.4 mm/s. Note that the differences with the reduced-dynamic orbits were slightly smaller based the increased "freedom" of the velocities from the dynamic to reduced-dynamic case. When the remove-restore procedure was implemented, the results were

not significantly improved. This was found to be caused by the edited points in the kinematic solution. The introduction of a reference orbit worsens the solution at these points which also causes worse performance at the neighboring points. Therefore, for the kinematic orbits, if the use of remove-restore method is desired than these points should not be included in the numerical differentiation process.

The final section in this chapter tested the methods in determining kinematic accelerations. The results were compared to accelerations output from the integrator during the orbit determination process. The residuals were on the order 4 to 7 μm/s^2 3-D RMS which is slightly worse than the results for a dynamic accelerations derived from positions which had an RMS of 0.35 μm/s^2.

Chapter 7

KBR Residuals

A unique advantage of GRACE POD processing is the availability of KBR data to evaluate the relative accuracy of orbit solutions. Note that in the GRACE gravity model processing at UT/CSR, KBR range-rate data is used since it avoids the discontinuities and bias uncertainties associated with range data. These discontinuities are caused by cycle slips or other interruptions in the K-Band ranging system. However, taking the time derivative of a signal generally increases the noise at high frequencies and decreases it at lower frequencies. Therefore, the benefit of using range-rate is that it reduces low-frequency noise which may attenuate the gravity signal relative to the data noise for the low-degree coefficients. The inter-satellite range acceleration information represents an independent data set to validate the derived accelerations from the previous chapters. In this chapter, the KBR range, range-rate, and range acceleration residuals are computed for all three orbit types: dynamic, reduced-dynamic, and kinematic in the J2000 frame.

7.1 Definitions

The equations for inter-satellite range, range-rate, and range acceleration are given by:

$$\rho(t) = \|\vec{r}_A(t) - \vec{r}_B(t)\|, \tag{7.1}$$

$$\dot{\rho}(t) = [\vec{v}_A(t) - \vec{v}_B(t)] \cdot \hat{e}_\rho, \tag{7.2}$$

$$\ddot{\rho}(t) = [\vec{a}_A(t) - \vec{a}_B(t)] \cdot \hat{e}_\rho + \frac{1}{\rho(t)}[\delta v(t)^2 - \dot{\rho}(t)^2], \tag{7.3}$$

where $\vec{r}$, $\vec{v}$, $\vec{a}$ represent the satellite position, velocity, and acceleration vectors, respectively, and $\hat{e}_\rho$ is the unit-range vector. In order to compensate for the large range residual biases, the mean has been subtracted.

7.2 Results

The baseline case compared the KBR data to the initial dynamic orbits used in RL05 processing at UT/CSR. Note that these orbits are at a 5 second sampling rate, and they also contain the output accelerations from the integrator. Therefore, no differentiation methods were used in this case. These results are shown in Figures 7.1 to 7.3.

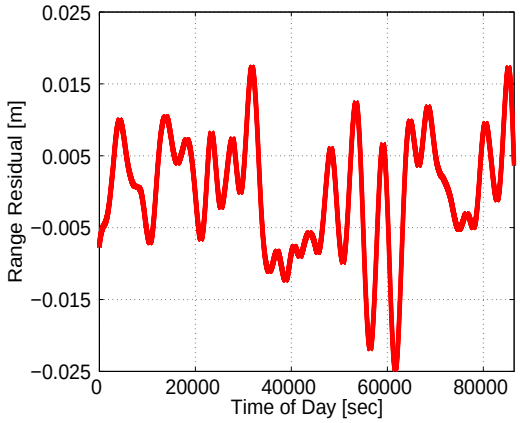

Figure 7.1: KBR Range Residuals - Dynamic Orbits at 5 second Rate

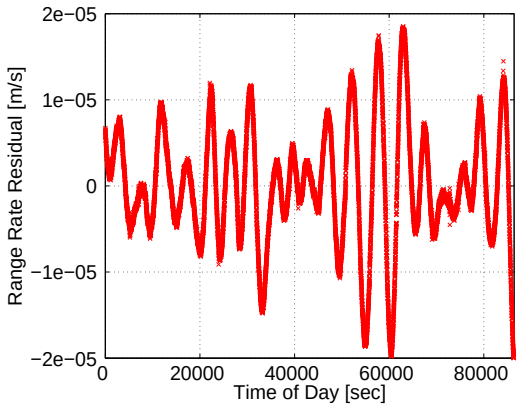

Figure 7.2: KBR Range-Rate Residuals - Dynamic Orbits at 5 second sampling

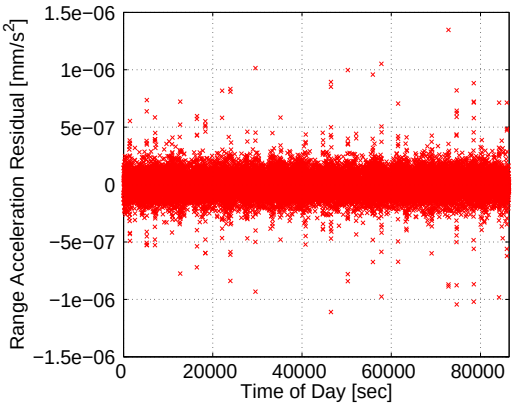

Figure 7.3: KBR Range Accelerations Residuals - Dynamic Orbits at 5 second sampling

The next case used derived dynamic and reduced-dynamic accelerations at a 5 second sampling rate. The positions and velocities are provided directly from the orbits. The accelerations used here were the two best results for a 5 second sampling rate from Chapter 5. Recall that this was Newton-Gregory interpolation for the dynamic accelerations and polynomial interpolation for the reduced-dynamic accelerations. Both were derived directly from velocities without remove-restore.

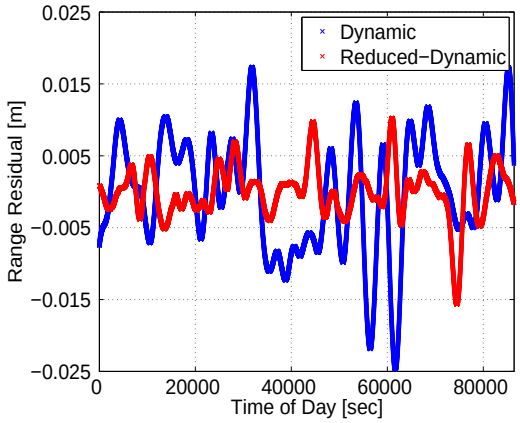

Figure 7.4: KBR Range Residuals - 5 second Case

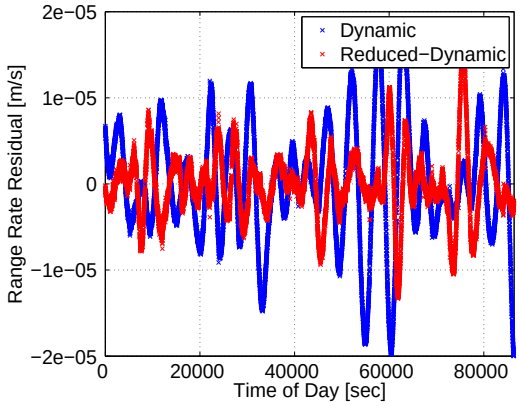

Figure 7.5: KBR Range-Rate Residuals - 5 second Case

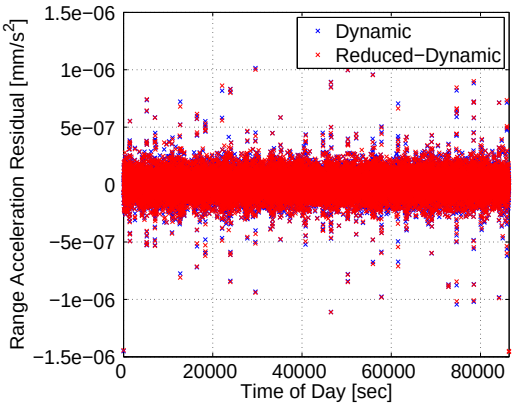

Figure 7.6: KBR Range Accelerations Residuals - 5 second Case

The final case utilized orbits and derived accelerations at a 30 second sampling rate. For the dynamic and reduced-dynamic comparison, the positions and velocities are provided directly from the orbits. The kinematic velocities were derived using the Savitzky-Golay filter without remove-restore. The dynamic, reduced-dynamic, and kinematic accelerations were derived using polynomial interpolation, polynomial interpolation with remove-restore, and the Savitzky-Golay filter with remove-restore, respectively. All accelerations were derived directly from velocities. Note that the KBR data were down-sampled to 30 seconds in order to correspond to the orbit data.

Table 7.1: Summary of KBR Residuals

Orbit Type	Range [m]	Range-Rate [mm/s]	Range-Acc [mm/s^2]
Dynamic	0.0081	0.0068	0.0003
Reduced-Dynamic	0.0036	0.0039	0.0001
Kinematic	0.0175	0.0124	0.0029

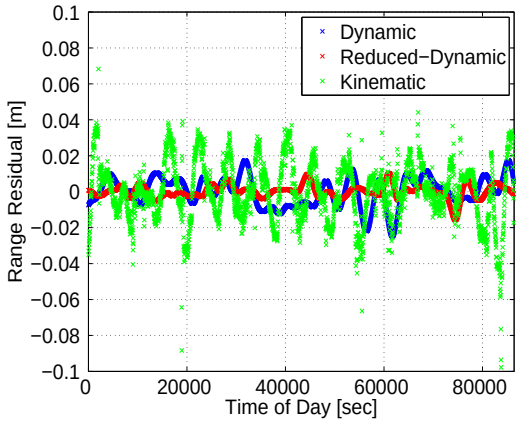

Figure 7.7: KBR Range Residuals - 30 second Case

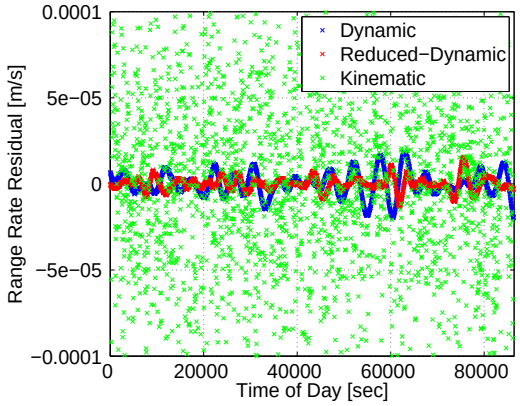

Figure 7.8: KBR Range-Rate Residuals - 30 second Case

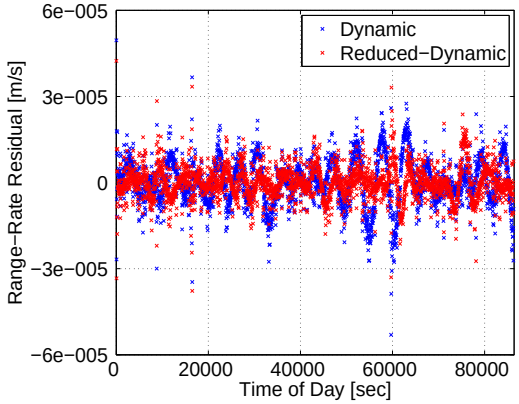

Figure 7.9: KBR Range-Rate Residuals (Zoomed In) - 30 second Case

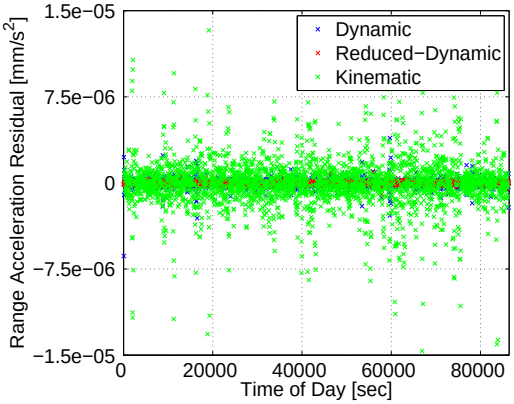

Figure 7.10: KBR Range Acceleration Residuals - 30 second Case

Based on initial inspection, the dynamic orbit best represents the best fit of the KBR, followed by the reduced-dynamic orbit. This was determined based on the RMS of the range, range-rate, and range-acceleration residuals summarized in Table 7.2. The kinematic orbit performs poorly in direct comparison to the KBR data. This is most likely explained by the epoch-wise

estimation process of the kinematic orbit solution, which means the positions are uncorrelated. Also, the noise introduced by the numerical differentiation also affects the kinematic results and make it difficult to draw conclusions from these statistics alone. Therefore, the PSDs of range-rate and range-acceleration were also computed and are shown Figures 7.11 and 7.12.

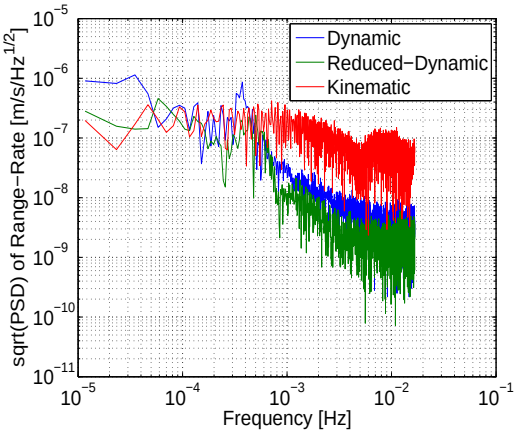

Figure 7.11: KBR Range-Rate Residuals PSD - 30 second Case

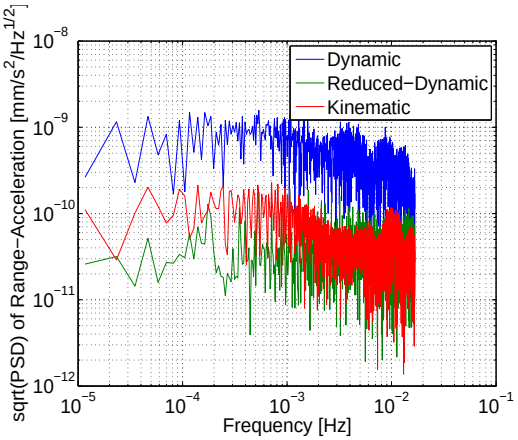

Figure 7.12: KBR Range-Accelerations Residuals PSD - 30 second Case

Recall that in the GRACE gravity estimation process, the accuracy of low-degree gravity coefficients is affected by acceleration errors while high-degrees are affected by errors in the KBR data [8]. Also, the monthly GRACE gravity estimates are derived from the dynamic orbit signal contained in the range-rate PSD (Figure 7.11). The reduced-dynamic range-rate spectrum is fairly similar to the dynamic, except with slightly higher noise at the mid to high frequencies. On the other hand, the kinematic results show much higher noise at all high-frequencies. This is contrary to expectations. Since the kinematic orbits should be tracking the total perturbation, its spectrum was expected to be the lowest. These results indicate that gravity field recovery using the kinematic velocities will not produce accurate results using the range-rate observable, and that one may have to aggregate a longer span of kinematic data in order to reduce the noise sufficiently.

In the range-acceleration PSD in Figure 7.12, the dynamic accelerations have higher noise frequency noise than the kinematic accelerations. While it is difficult to discern the difference between signal and noise in this plot, it does indicate that there may be a chance to obtain better knowledge of the lower degrees by utilizing the kinematic accelerations. Such methods are described in [15] and [31].

Chapter 8

Conclusions

8.1 Summary

This study was performed to assess the performance of dynamic, reduced-dynamic, and kinematic precise orbit solutions for the GRACE mission. First the relationship between velocity variation and gravity potential was examined. It was found that the velocity uncertainty must be under 3 mm/s for gravity field recovery at the very lowest degrees, and better than 0.1 mm/s for degrees up to 30. The positions of dynamic and reduced-dynamic orbits were found to agree within 1 to 2 cm, and the velocities agree within 0.01 to 0.02 mm/s. An editing procedure was implemented for the kinematic orbits to remove outliers and improve the solution. This method involved flagging bad points where the difference between the kinematic position and a reference orbit (i.e., dynamic or reduced-dynamic) at a specific epoch violated a given tolerance. After the editing process, the kinematic positions were found to agree within 3 to 4 cm of the other two orbit types.

As part of this study, several numerical methods were analyzed to determine how accurate they are in constructing the velocities and accelerations of orbits. In the case of dynamic or reduced-dynamic orbits where the veloc-

ities are missing or the accelerations are required, polynomial interpolation should provide sufficient precision and accuracy. The Savitzky-Golay filter was determined to be the best method for performing numerical differentiation of kinematic orbits at a 30 sec sampling rate. While the remove-restore procedure proved to be a useful tool when differentiating dynamic or reduced dynamic orbits, it performs poorly when used on edited kinematic orbits velocities. For this reason, it is not recommended for velocity recovery. However, remove-restore was successful in improving the derived accelerations for the reduced-dynamic and acceleration cases. Additionally, it is clear that a 30 second sampling interval is not adequate to extract the accelerations sufficiently.

Finally, the orbits were compared using KBR range, range-rate, and range-acceleration residuals. The raw RMS results generally favored the dynamic orbit. Spectral analysis indicated that current knowledge of the kinematic velocities is inadequate for gravity field determination. However, the range-acceleration spectrum of the kinematic orbit was better than the dynamic orbit. While there was a lot of noise in this comparison, it indicated that kinematic accelerations may potentially have signal that could improve gravity knowledge at low degrees.

8.2 Future Work

While several random days were tested for this study, more effort may be required to use outlined procedure for editing and differentiating kinematic orbits for any given day. Additional studies should be conducted to determine

if obtaining kinematic orbits at 5 second intervals is appropriate and what impact this may have. Some initial studies were conducted at the end of this study on new kinematic orbits sampled every 10 seconds, however, they had too many "bad" points and the results were not improved. Finally, the spherical harmonic analysis should be investigated to see if the different numerical methods analyzed in this study have an impact on the quality of the produced gravity field. This could provide insight into the impact of the errors caused by the limitations of numerical differentiation on gravity field recovery.

Appendices

Appendix A

The Global Positioning System

A.1 Introduction

Since the late 1970s, the U.S. Department of Defense (DOD) has operated the NAVigation Satellite Time and Ranging Global Positioning System (NAVSTAR GPS). GPS is a satellite-based navigation system designed to provide highly accurate position and timing information globally to anyone with a GPS receiver. The GPS tracking system consists of three segments: the space segment, the control segment, and the user segment.

The space segment originally consisted of 24 satellites (currently there are 32 operational satellites). The operational satellites are spread out over six orbital planes whose line of nodes are separated by 60 degrees. Each satellite operates in a nearly circular 20,000 km altitude orbit at an inclination of 55 degrees with an orbital period of 12 hours. This configuration, as depicted in Figure A.1, is designed to provide continuous global coverage such that at least 4 satellites are always visible from any location on the surface. Therefore, with four visible GPS satellites, a position fix can be produced anywhere on Earth. As many as twelve satellites may be visible for elevation angles above the local horizon.

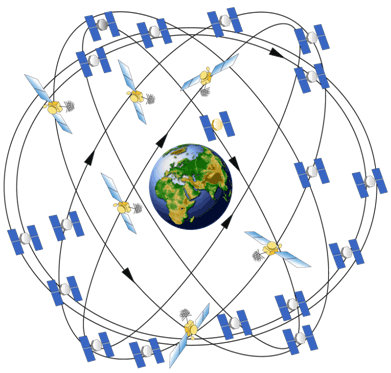

Figure A.1: GPS Constellation [38]

The Air Force normally flies more than 24 GPS satellites to maintain coverage whenever the baseline satellites are serviced or decommissioned. These additional satellites are not considered part of the core constellation, but they provide redundant measurements which may improve the precision of GPS receiver calculations. With an increased number of satellites, the constellation is no longer uniform. This arrangement improves reliability and availability, relative to a uniform system, when multiple satellites fail. Currently, the GPS constellation consists of 31 Block IIA/IIR/IIR-M satellites.

The control segment consists of tracking locations spread throughout the world. There is a Master Control Station (MCS), an alternate MCS, four dedicated ground antennas, and six dedicated monitor stations. The MCS is located in Colorado Springs, Colorado. These monitor stations measure signals from the satellites which are incorporated into orbital models for each of the satellites. The models require precise ephemerides and SV clock corrections

for each satellite. The MCS processes the data collected by the monitoring stations to determine satellite orbits and update each satellite's navigation message. The ground antennas are used to transmit the navigation message updates to each satellite once per day. The satellites then send subsets of the ephemeris data to GPS receivers over radio signals.

The user segment consists of GPS antennas and receivers that can provide position, velocity, and time information to the user. The receiver could be located at any point on the Earth or on-board a satellite (nominally below the GPS constellation). Although originally intended for military use, GPS has evolved into both a military and civilian tool. It is used by the civilian community for navigation in aviation and automobiles as well as position determination in spacecraft guidance. In addition, GPS has proved invaluable in the fields of surveying, mapping, and other precise geodetic applications.

A.2 Satellite-Based Navigation

The concept of satellite-based positioning is based on using time to measure distance. If the time it takes for the signal broadcast from the satellite to reach the receiver is known, the range between the satellite and the receiver can be determined. Therefore, each GPS satellite carries very stable, high accuracy atomic clocks. Using these clocks, each GPS satellite generates a nominal L-band frequency at 10.23 MHz [24]. Each GPS satellite transmits a signal continuously on two L-band frequencies known as L1 and L2, generated by multiplying the fundamental frequency by 152 and 120, respectively,

resulting in

$$L1 = 1574.42 \text{ MHz},$$

$$L2 = 1227.60 \text{ MHz}.$$

Unique information is sent along with codes on each signal in order to identify the signals of different GPS satellites. These codes are characterized by pseudo-random noise (PRN) sequences. Each of the two signal frequencies is modulated with a code. The L1 signal is modulated by the precision (P) code and a coarse acquisition (C/A) code, while the L2 signal is modulated only by the P code. Appropriate ground receivers generate the same code and match the received code to determine the transmit time and range. This type of observable is known as pseudorange. One has to compensate for many unavoidable errors such as inaccurate GPS satellite positions, clock inaccuracies, tropospheric and ionospheric refraction of the signal, atmospheric absorption, receiver noise, multipath error, and clock errors. In addition to the C/A-code and the P-code, a navigation message is superimposed on the L1 and L2 carriers to transmit the information required for basic navigation. This data includes GPS satellite ephemerides, time synchronization information, and correction terms to ionospheric delay and GPS clock errors [24]. Pseudoranges to four satellites are required to compute the receiver position and the clock bias using triangulation. Additional satellites can be used to reduce random error.

The alternate type of observable is carrier phase; this allows the user

to track the phase difference between doppler-shifted frequencies from the moving GPS satellites to the receivers. It works by counting the number of cycles of the L1 and L2 carrier frequency that are received. By tracking the frequency and reproducing the sinusoid, it is possible to count the number of cycles received. It is typically 100 times more precise than the pseudorange but requires the resolution of the integer number of wavelengths since the initial phase is unknown [25]. This process is known as ambiguity resolution. For more detail on GPS signal structure, see Misra and Enge [39].

The accuracy of a position solution is partly dependent on the receiver and GPS satellite geometry. This quantity is typically measured as Geometric Dilution of Precision (GDOP). To obtain the smallest GDOP, the GPS satellites should be widely dispersed with respect to the receiver tracking them. This concept is illustrated in Figure A.2. However, contemporary GPS receivers are capable of tracking up to fifteen GPS satellites, so it is not a major source of error for kinematic solutions [24]. In the kinematic case, tracking more GPS satellites should improve the solution.

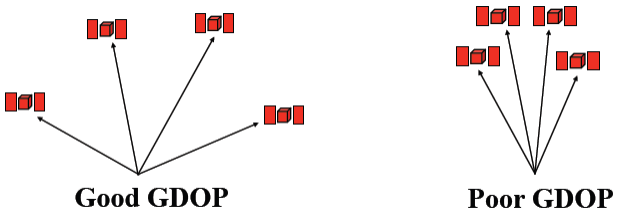

Figure A.2: GDOP Illustration

A.3 International GNSS Service

The International GNSS Service (IGS), formerly the International GPS Service, is a collaboration of more than 200 worldwide government agencies and universities. Formed in 1993 as a service of the International Association of Geodesy (IAG), the IGS supports geodetic research by providing various GPS data products. The IGS collects, archives, and distributes accurate data sets that meet the requirements of scientific and engineering applications and studies. The products created by IGS consist of [40]:

- GPS satellite ephemerides,
- Earth rotation parameters,
- IGS tracking station coordinates and velocities,
- GPS satellite and tracking station clock information,
- Zenith tropospheric path delay estimates,
- Global ionospheric maps.

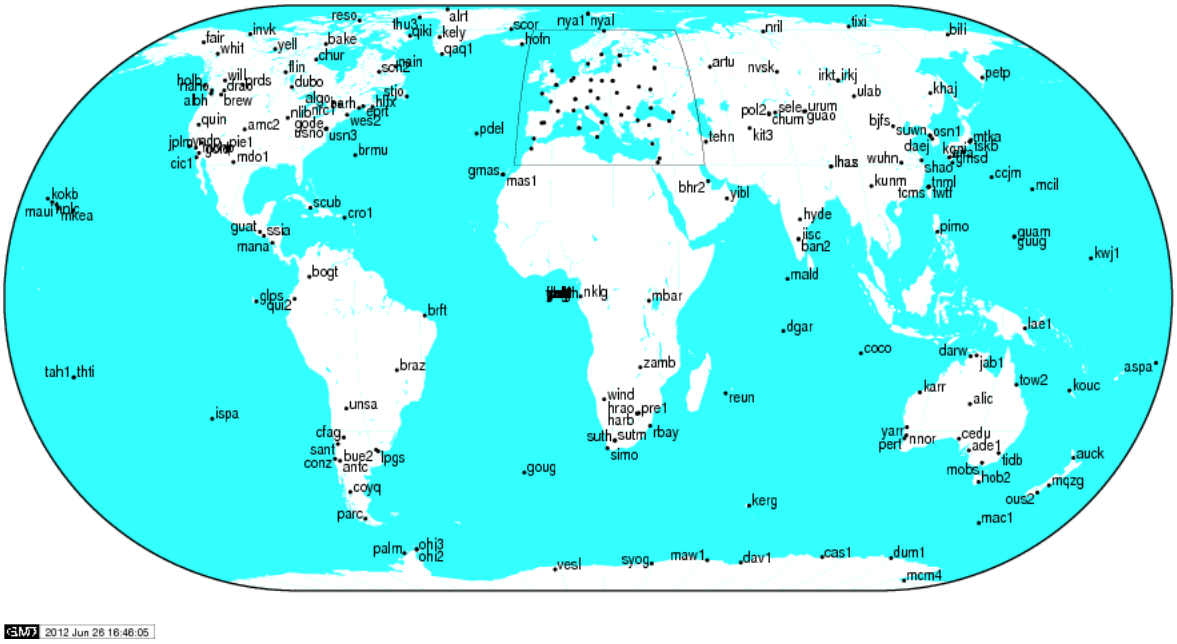

Figure A.3: IGS Tracking Stations [40]

IGS products support scientific activities such as improving determination of the International Terrestrial Reference Frame (ITRF), monitoring deformations of the solid Earth and variations in the Earth's sea level and ice sheets, determining orbits of scientific satellites, and monitoring the ionosphere [40].

Appendix B

Fundamentals of Orbit Determination

B.1 Dynamic Orbit Determination

The three primary components of the dynamic POD procedure are

- Numerical Integration and Force Modeling,
- Observation Processing,
- Estimation Algorithm.

B.1.1 Orbit Dynamics and Force Models

B.1.1.1 Time Systems

Time is expressed in many different ways; historical methods are based on the rotation of the Earth while newer ones are based on atomic time standards. An event can be described by a calendar date and time of day, expressed in local time or Universal Time. Alternatively, it can also be identified by a Julian Date (JD), which is measured from 4713 B.C. Time transformations are necessary in order to relate the time tags associated with observations to the independent variable in the equations of motion because the various time systems are not uniform.

The international standard for time is International Atomic Time (TAI). TAI is obtained from counting the oscillations of a Cesium-133 atom. TAI is maintained as a paper clock determined by averaging a number of real clocks. The offset between each clock and TAI is monitored by traveling clocks, or more routinely, by broadcast time transfer.

The independent variable conventionally used in the equations of motion is Terrestrial Time (TT). TT is an abstract uniform time scale which is related to TAI by

$$TDT = TAI + 32.184 \text{ s.} \tag{B.1}$$

The conventional time scale for planetary ephemerides is Solar-system Barycentric Dynamical Time (TDB). TT is transformed to TDB using only periodic variations; this transformation is given in [41]. Please refer to the IERS 2010 conventions for additional details on the various time definitions [42].

The time system based on the rotation of the Earth is Universal Time (UT). It is defined conceptually as the Greenwich hour angle of the fictitious mean sun relative to the mean vernal equinox plus 12 hours. A number of effects contribute to the rotation of the Earth. Several new time quantities remove some of the contributions from the Earth's rotation. UT0 is derived from direct observations of the diurnal motion of the stars. UT1 is obtained from UT0 by removing the effects of polar motion. UT2 is UT1 with the effects of seasonal variations in the Earth's rotation rate removed. UT1R is equivalent to UT1 with high frequency tidal effects removed.

The time system used for observation time tags is Coordinated Universal Time (UTC). It is a uniform time system derived from atomic time that is adjusted to adapt to Earth's rotation changes. UTC differs from TAI by an integer number of seconds. Including the time zone differences in this calculcation results in civilian time. UTC is adjusted relative to TAI by adding leap seconds to ensure close relation to UT2.

GPS Time (GPST) is an atomic time scale used in GPS satellites and the GPS ground control stations. Unlike UTC, GPS is not adjusted for leap seconds. GPS time was last synchronized with UTC on January 6, 1980, and is currently ahead of UTC by 16 seconds. A coarser unit of time used for GPS observations is the GPS Week. The GPS Week is the number of days since January 6, 1980, divided by seven.

B.1.1.2 Coordinate Systems

An inertial reference frame is needed to integrate the equations of motion since Newton's equations are valid only in inertial space, i.e. a frame defined by a stationary, non-rotating set of orthogonal axis vectors. The coordinate system used for the dynamic model in MSODP1 is the J2000 Earth-centered Inertial (ECI) coordinate system. It is a geocentric inertial coordinate system defined by the mean equator and equinox at Julian epoch 2000.0. The x-axis is aligned with the mean equinox, the z-axis is aligned with the Earth's spin axis, and the y-axis is rotated 90 degrees East about the celestial equator [43]. The Jet Propulsion Laboratory (JPL) DE-400 series of planetary

ephemerides, which contain the positions and velocities of the planets, are released in the J2000 Barycentric Inertial Coordinate System and must be transformed to the ECI frame [44].

The positions of tracking stations, atmospheric drag perturbations, and gravitational perturbations are expressed in the Earth-centered-Earth-fixed (ECEF) rotating coordinate system. Vectors represented in the ECEF reference frame can be transformed to the ECI frame by considering the precession and nutation of the Earth, polar motion and variations in the rotation of the Earth (UT1-TAI).

The Radial-Tangential-Normal (RTN) system is a local orbital frame. The RTN directions are specified by unit vectors $\hat{u}_r$, $\hat{u}_t$, and $\hat{u}_n$, which are defined by,

$$\vec{r} = r\hat{u}_r$$

$$\vec{h} = h\hat{u}_n$$

and $\hat{u}_t$ completes the right-handed orthogonal system [1]. The origin is located at the satellite's center of mass, and it rotates as the satellite moves around the Earth. The radial axis is along the vector $\vec{r}$ from the center of the Earth toward the satellite. The tangential axis is in the direction of the local horizontal component of the velocity vector (or if the orbit is exactly circular, the velocity vector direction itself), and it may be referred to as the along-track direction. The normal axis is parallel to the satellite's angular momentum vector $\vec{h}$, and it may be referred to as the cross-track direction. An illustration of this is

shown in Figure B.1.1.2. The elements of the ECI to RTN transformation are given by [1]:

$$\begin{aligned} \hat{u}_r &= \frac{\vec{r}}{|\vec{r}|} \\ \hat{u}_t &= \hat{u}_n \times \hat{u}_r \\ \hat{u}_n &= \frac{\vec{r} \times \vec{v}}{|\vec{r} \times \vec{v}|} \end{aligned} \tag{B.2}$$

where $\vec{r}$ and $\vec{v}$ are the position and velocity vectors of the reference orbit.

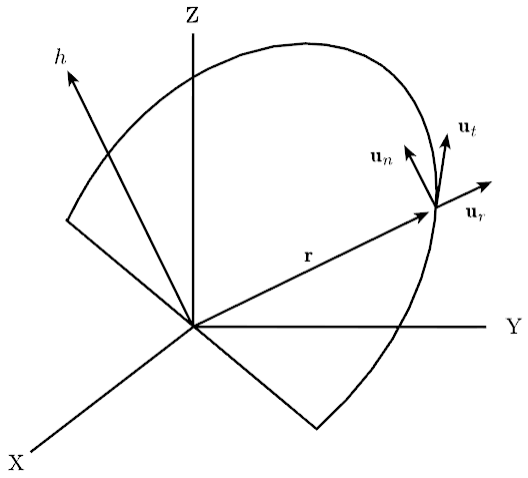

Figure B.1: RTN Coordinate System [1]

Finally, the body-fixed frame is a set of orthogonal vectors that are fixed to the body of the spacecraft. The various sensors and actuators of the spacecraft are typically defined with respect to the body frame. MSODP produces POD solutions in both the body-fixed and J2000 reference frames.

B.1.1.3 Equations of Motion

The force models used to describe the motion of an Earth orbiting satellite can be divided into three categories [3]:

1. Gravitational forces acting on the satellite, i.e., Earth's geopotential, solid earth tides, ocean tides, planetary third-body perturbations, and relativistic accelerations;

2. Non-gravitational forces, i.e., drag, solar radiation pressure, earth radiation pressure, and thermal radiation acceleration;

3. Empirical force models to accommodate unmodeled or mismodeled forces.

The resulting equations of motion for a LEO satellite in an inertial reference frame are:

$$\ddot{\vec{a}} = \vec{a}_g + \vec{a}_{ng} + \vec{a}_{emp}, \tag{B.3}$$

where $\ddot{\vec{a}}$ is the acceleration vector of the center of mass of the satellite (i.e., second differential of the position vector), $\vec{a}_g$ is the sum of the gravitational forces on the satellite, $\vec{a}_{ng}$ is the sum of non-gravitational forces acting on the surface of the satellite, and $\vec{a}_{emp}$ is empirical contribution that accounts for unmodeled or incorrectly modeled forces acting on the satellite [3].

B.1.1.4 Gravitational Forces

The gravitational forces, $\vec{a}_g$, can be expressed as

$$\vec{a}_g = \vec{P}_{geo} + \vec{P}_{st} + \vec{P}_{oy} + \vec{P}_{rd} + \vec{P}_n + \vec{P}_{rel} \tag{B.4}$$

where,

$\vec{P}_{geo}$ = perturbations due to the mass distribution of the Earth,

$\vec{P}_{st}$ = perturbations due to solid Earth tides,

$\vec{P}_{oy}$ = perturbations due to ocean tides,

$\vec{P}_{rd}$ = perturbations due to rotational deformation,

$\vec{P}_{n}$ = perturbations due to third-body effects,

$\vec{P}_{rel}$ = perturbations due to general relativity.

B.1.1.5 Non-Gravitational Forces

The non-gravitational forces, $\vec{a}_g$, are surface forces that depend on the shape and orientation of the satellite. They can be expressed as

$$\vec{a}_{ng} = \vec{P}_{drag} + \vec{P}_{solar} + \vec{P}_{earth} + \vec{P}_{thermal} \tag{B.5}$$

where,

$\vec{P}_{drag}$ = perturbations due to the atmospheric drag,

$\vec{P}_{solar}$ = perturbations due to solar radiation pressure,

$\vec{P}_{earth}$ = perturbations due to the Earth's radiation pressure,

$\vec{P}_{thermal}$= perturbations due to thermal radiation.

The development of accurate force models for both $\vec{a}_g$ and $\vec{a}_{ng}$ has been a major research topic for the past two decades, especially at UT/CSR. For a full description of the mathematical models of the non-gravitational forces implemented in MSODP please refer to [3].

B.1.1.6 Empirical Accelerations

In order to account for unmodeled or incorrectly modeled forces, empirical accelerations are introduced to the orbit determination procedure. The implementation of this is similar to what is done in reduced-dynamic orbit determination. As additional force model parameters are estimated in the dynamic orbit prcocess, it can start to approximate a reduced-dynamic approach [22]. In this case, empirical accelerations include tangential perturbations and one-cycle-per-orbital-revolution (1-cpr) force in the radial, transverse, and normal directions. Many mismodeled forces are known to show a one cycle-per-revolution (1-cpr) frequency associated with the satellite orbital period, and the introduction of these parameters can significantly reduce orbit errors occurring at the 1-cpr frequency and in the along track direction [23]. They remove the long period effect of mismodeled forces and improve orbit determination accuracy and have piecewise constant values over 3-4 hours. Since these are not explicitly present in the measurement equation, they are implemented into the estimation process via propagation of the state transition matrix as explained later in this chapter.

The tangential perturbation can be modeled empirically as

$$\vec{P}_{tangen} = C_t \hat{u}_t \tag{B.6}$$

where,

C_t = empirical tangential parameter,

$\hat{u}_t$ = unit vector in the tangential direction.

A set of piecewise constants, C_t, can be estimated to account for these unmodeled tangential perturbations. Unmodeled perturbations in the radial, transverse, and normal directions can be modeled as

$$\vec{P}_{rtn} = \begin{bmatrix} P_r \\ P_t \\ P_n \end{bmatrix} = \begin{bmatrix} C_r \cos u + S_r \sin u \\ C_t \cos u + S_t \sin u \\ C_n \cos u + S_n \sin u \end{bmatrix} \tag{B.7}$$

where,

P_r = one-cycle-per-revolution radial perturbation,

P_t = one-cycle-per-revolution transverse perturbation,

P_n = one-cycle-per-revolution normal perturbation,

u = argument of latitude of the satellite,

C_r, S_r = one-cycle-per-revolution radial parameters,

C_t, S_t = one-cycle-per-revolution transverse parameters,

C_n, S_n= one-cycle-per-revolution normal parameters.

B.1.2 Observation Processing

In theory, the equations of motion described in Equation B.3 would perfectly model the motion of a near Earth artificial satellite. With the proper initial conditions, one could numerically integrate these equations to compute the position and velocity of the satellite at any time. However, errors in the initial conditions and model parameters cause this solution to deviate from the actual state. This is why independent observations are used to correct the predicted solution. As previously described, for GRACE POD processing at

UT/CSR, GPS Double-Differenced Carrier Phase measurements are used.

B.1.2.1 Mathematical Formulation of DDHL Observtations

The equations used to form DDHL observations are discussed here. The carrier phase measurement between a GPS satellite and receiver (located either on-board a satellite or at a ground station) can be modeled as,

$$\phi_i^{cj}(t_{R_i}) = \phi^j(t_{T_i}) - \phi_i(t_{R_i}) + N_i^j(t_{0_i}) \tag{B.8}$$

where,

t_{R_i}= receive time at i-th receiver,

t_{T_i} = transmit time of j-th GPS satellite's phase received by i-th receiver,

ϕ_i^{cj}= computed phase difference between j-th GPS satellite and i-th receiver,

ϕ^j = phase of j-th GPS satellite signal received by i-th receiver,

ϕ_i = phase generated by i-th ground receiver,

t_{0_i} = initial epoch of i-th receiver,

N_i^j=unknown integer bias, i.e. ambiguity.

The signal transmit time of the j-th GPS satellite can be related to the signal receive time by including the range between the transmitter and receiver as well as error terms such that:

$$t_{T_i^j} = t_{R_i} - (\rho_i^j(t_{R_i}/c) - \delta t_{\phi_i^j}, \tag{B.9}$$

where ρ_i^j is the geometric line of sight range between j-th GPS satellite and i-th receiver and δt_ϕ represents the sum relativistic effects, ionospheric and

tropospheric delay. Since the time tag of the measurement is in the receiver time scale, which has some clock error, the true receive time is

$$t_{R_i} = t_i - \delta t_{c_i}, \tag{B.10}$$

where δt_{c_i} represents the clock error of the i-th receiver. The satellite and ground station receiver oscillators use highly stable clocks; therefore, a linear approximation of $\phi(t + \delta t) = \phi + f \cdot \delta t$ can be used for the clock error. Substituting the previous expressions for signal transmit time and true receive time (Equations B.9 and B.10, respectively) into Equation B.8, the expression for the carrier phase measurement becomes

$$\phi_i^{cj}(t_{R_i}) = \phi^j(t_i) - f^j \cdot [\delta t_{c_i} + (\rho_i^j(t_{R_i})/c) + \delta t_{\phi_i^j}] - \phi_i^{cj}(t_{R_i}) + N_i^j(t_{0_i}) \tag{B.11}$$

when neglecting higher order terms.

Each receiver obtains signals from more than one GPS satellite. By differencing Equation B.11 with a similar expression for the i-th receiver and l-th GPS satellite, a single-differenced phase (SDP) measurement can be formed as,

$$SDP_i^{jl} = \phi_i^{cj}(t_{R_i}) - \phi_i^{cl}(t_{R_i}). \tag{B.12}$$

With data from another receiver, which can be called the k-th receiver, two SDP measurements can be differenced to create a double-differenced phase (DDP) measurement:

$$DDP_{ik}^{jl} = SDP_i^{jl} - SDP_k^{jl} \tag{B.13}$$

which, when expanded, becomes:

$$\begin{aligned} DDP_{ik}^{jl} = & - f^j \cdot [\delta t_{c_i} + (\rho_i^j(t_{R_i})/c) + \delta t_{\phi_i^j}] \\ & + f^l \cdot [\delta t_{c_i} + (\rho_i^l(t_{R_i})/c) + \delta t_{\phi_i^l}] \\ & + f^j \cdot [\delta t_{c_k} + (\rho_k^j(t_{R_k})/c) + \delta t_{\phi_k^j}] \\ & - f^l \cdot [\delta t_{c_k} + (\rho_i^l(t_{R_k})/c) + \delta t_{\phi_k^l}] \\ & + \phi^j(t_i) - \phi^l(t_i) + \phi^j(t_k) + \phi^l(t_k) + N_{ik}^{jl}, \end{aligned} \tag{B.14}$$

where $N_{ik}^{jl} = N_i^j(t_{0_i}) - N_k^j(t_{0_k}) - N_i^l(t_{0_i}) + N_k^l(t_{0_k})$. Note that all the phase terms associated with the ground receiver and the satellite are cancelled out.

To convert DDP measurements to range, Equation B.14 is multiplied by a negative nominal wavelength, $-\lambda = -c/f_0$, where f_0 is the nominal value for the transmitted frequency of the GPS signal and the receiver mixing signal, resulting in:

$$\begin{aligned} DDP_{ik}^{jl} = & \left(\frac{f^j}{f_0}\right) \cdot (\rho_i^j(t_{R_i}) - \rho_k^j(t_{R_k})) - \left(\frac{f^l}{f_0}\right) \cdot (\rho_i^l(t_{R_i}) - \rho_k^l(t_{R_k})) \\ & - \left(\frac{c}{f_0}\right) \cdot (\phi^j(t_i) - \phi^l(t_i) + \phi^j(t_k) + \phi^l(t_k)) \\ & + c \cdot \left(\frac{f^j - f^l}{f_0}\right) \cdot (\delta t_{c_i} - \delta t_{c_k}) \\ & + \left(\frac{f^j}{f_0}\right) \cdot (\delta \rho_{\phi_i^j} - \delta \rho_{\phi_k^j}) - \left(\frac{f^l}{f_0}\right) \cdot (\delta \rho_{\phi_i^l} - \delta \rho_{\phi_k^l}) \\ & + C_{ik}^{jl}, \end{aligned} \tag{B.15}$$

where $\delta\rho_\phi = -c \cdot \delta t_\phi$ and $C_{ik}^{jl} = -\lambda \cdot N_{ik}^{jl}$. Note that there are two different time tags, associated with the two receivers. If the two receiver clocks are synchronized, then the second line can be cancelled out. In practice the receiver clocks

are not synchronized, but differ by a constant, dt. If this difference is small (on the order of 1 second), a linear approximation can be applied. Therefore, substituting $t_k = t_i + dt_{ik}$ in Equation B.15 yields:

$$\begin{aligned} DDP_{ik}^{jl} = & \left(\frac{f^j}{f_0}\right) \cdot (\rho_i^j(t_{R_i}) - \rho_k^j(t_{R_k})) - \left(\frac{f^l}{f_0}\right) \cdot (\rho_i^l(t_{R_i}) - \rho_k^l(t_{R_k})) \\ & + c \cdot \left(\frac{f^j - f^l}{f_0}\right) \cdot dt_{ik} \\ & + c \cdot \left(\frac{f^j - f^l}{f_0}\right) \cdot (\delta t_{c_i} - \delta t_{c_k}) \\ & + \left(\frac{f^j}{f_0}\right) \cdot (\delta\rho_{\phi_i^j} - \delta\rho_{\phi_k^j}) - \left(\frac{f^l}{f_0}\right) \cdot (\delta\rho_{\phi_i^l} - \delta\rho_{\phi_k^l}) \\ & + C_{ik}^{jl}, \end{aligned} \tag{B.16}$$

Since the oscillators used for the clocks on GPS satellites are highly stable, their frequencies usually stay close to the nominal frequency, f_0. By expressing the frequencies of the two satellite's oscillators as a sum of the nominal frequency and an offset, $f^j = f_0 + \Delta f^j$ and $f^l = f_0 + \Delta f^l$, Equation B.16

becomes:

$$
\begin{aligned}
DDP_{ik}^{jl} =& \rho_i^j(t_{R_i}) - \rho_k^j(t_{R_k}) - \rho_i^l(t_{R_i}) + \rho_k^l(t_{R_k}) \\
&+ \left(\frac{\Delta f^j}{f_0}\right)(\rho_i^j(t_{R_i}) - \rho_k^j(t_{R_k})) - \left(\frac{\Delta f^l}{f_0}\right)(\rho_i^l(t_{R_i}) - \rho_k^l(t_{R_k})) \\
&+ c \cdot \left(\frac{\Delta f^j - \Delta f^l}{f_0}\right) \cdot dt_{ik} \\
&+ c \cdot \left(\frac{\Delta f^j - \Delta f^l}{f_0}\right) \cdot (\delta t_{c_i} - \delta t_{c_k}) \\
&+ \delta\rho_{\phi_i^j} - \delta\rho_{\phi_k^j} - \delta\rho_{\phi_i^l} + \delta\rho_{\phi_k^l} \\
&+ \left(\frac{\Delta f^j}{f_0}\right) \cdot (\delta\rho_{\phi_i^j} - \delta\rho_{\phi_k^j}) - \left(\frac{\Delta f^l}{f_0}\right) \cdot (\delta\rho_{\phi_i^l} - \delta\rho_{\phi_k^l}) \\
&+ C_{ik}^{jl},
\end{aligned}
\tag{B.17}
$$

The second, third, fourth, and sixth lines contain terms that include the frequency offset. The offset divided by the nominal frequency is an expression of the stability of the GPS satellite clock. As previously mentioned, the atomic clocks on GPS satellites are highly stable. This is small when compared to the noise level of the measurement, thus for small baselines between two receivers the contribution of the second line can be ignored. The terms in the sixth line can be ignored, since their contribution is also small compared to the noise level. The terms in the fourth line include the receiver clock errors. These terms can also be ignored due to their small contribution. Therefore, by ignoring lines two, four, and six and applying a linear approximation to the range terms in the first line and using Equation B.10 for both receivers,

Equation B.17 becomes:

$$\begin{aligned} DDP_{ik}^{jl} =& \rho_i^j(t_{R_i}) - \rho_k^j(t_{R_k}) - \rho_i^l(t_{R_i}) + \rho_k^l(t_{R_k}) \\ & - [\dot{\rho}_i^j(t_i) - \dot{\rho}_k^l(t_i)]\delta t_{c_i} + [\dot{\rho}_k^j(t_k) - \dot{\rho}_k^l(t_k)]\delta t_{c_k} \\ & + c \cdot \left(\frac{\Delta f^j - \Delta f^l}{f_0} \right) \cdot dt_{ik} \\ & + \delta\rho_{\phi_i^j} - \delta\rho_{\phi_k^j} - \delta\rho_{\phi_i^l} + \delta\rho_{\phi_k^l} \\ & + C_{ik}^{jl}, \end{aligned} \tag{B.18}$$

The term in the third line involving the difference between the receiver clocks is not ignored, but will be zero if the two receivers are set to track satellites simultaneously. The terms in the second line can be accounted for if independent receiver clock information from pseudo-range measurements is available. If this information is not available, the receiver clock errors can be modeled as linear functions comprised of a clock bias term and clock drift term.

Producing DD observables formed by the differences between the two single-differences from two different GPS satellites eliminates the ground receiver and GRACE GPS receiver clock error. However, there are still some errors that have not been eliminated. For example, the terms in the fourth line include propagation delay and relativistic effects. First-order ionospheric effects are removed by combining the DD carrier phase observables from dual frequencies: L1 and L2. The rest of the effects–including tropospheric delay, general and special relativity, phase windup, phase center offsets in the transmitting and receiving antennas, and ground station effects–are covered in [3]. In addition, the positions of the GPS satellites and the tracking sta-

tion receivers, which are provided by the IGS, and *a priori* values for the double-difference ambiguities, typically assumed to be zero, are required.

B.1.3 Formulation of Orbit Determination Problem

A set of "computed" DDHL measurements is generated using Equation B.18 and a reference trajectory, obtained by numerically integrating Equation B.3. The resulting observations are then compared to the actual, or "observed", DDHL measurements obtained. The difference between the observed and computed quantities is typically referred to as "O-C", or the observation residual. The dynamic POD approach is to minimize the observation residual in the least squares sense by updating the initial conditions and selected parameters in the dynamic and observation models. This is accomplished by first linearizing the dynamic and observation models and then applying a least-squares batch filter.

B.1.3.1 Linearization of Orbit Determination Problem

The equations of motion and the observation model equation (Equations B.3 and B.18, respectively) are highly complex, non-linear differential equations. The state cannot be solved directly. If the state and observation vectors can be related linearly, linear estimation theory can be applied to solve for the state. Assuming a reference trajectory is available and the true trajectory is close to this, the trajectory for the actual motion can be expanded in a Taylor series about the reference trajectory at each point in time. Trun-

cating to eliminate higher order terms, the deviation in the state from the reference trajectory can be described by a set of linear differential equations with time-dependent coefficients.

The following derivation is based on the approach in [1]. First, the unknown, n-dimensional state vector $X(t)$, is defined to include the satellite position $\vec{r}$ and velocity $\dot{\vec{r}}$, along with a selected set d of dynamic or observation model parameters to be estimated.

$$X(t) = \begin{bmatrix} \vec{r} \\ \dot{\vec{r}} \\ d \end{bmatrix} \tag{B.19}$$

The original equation of motion (Equation B.3) can be expressed as,

$$\dot{X} = F(X, t), \quad X(t_0) \equiv X_0 \tag{B.20}$$

where, X_0 represents the initial conditions. Similarly, the mathematical observation model relating the GPS observables to the satellite state (i.e., observer-state relationship) is,

$$Y_i = DDHL_i = G(X_i, t_i) + \epsilon_i; \quad i = 1, \ldots, l \tag{B.21}$$

where Y_i is the vector of observations at t_i, $G(X_i, t_i)$ is the observation model relating the state at time X_i at time t_i to observations, and ϵ_i is a vector of observation errors. The number of observations at a particular epoch depends on the number of GPS satellites tracked by each receiver and their relative geometry. The DD ambiguity must be estimated for each pass, defined as a series of consecutive DDHL combinations of the same receivers and GPS

satellites, and is included in the set d. Based on the results obtained by [21], the GPS orbits are held fixed to IGS solutions in the POD process. They could be estimated along with the positions of tracking station receivers if desired by being added to the state.

The previous equations can be linearized about a reference trajectory if the reference and true trajectories are sufficiently close throughout the time interval of interest. To show this, start by defining

$$x(t) = X(t) - X^*(t), \quad t_0 \leq t \leq t_f \tag{B.22}$$

$$y_i = Y_i - G(X_i^*, t_i), \quad i = 1, \ldots, l. \tag{B.23}$$

By substituting these expressions into Equations B.20 and B.21, we can perform a Taylor series expansion to get

$$\dot{X}(t) = F(X,t) = \dot{X}^* + \left[\frac{\partial F}{\partial X}\right]^* x_i + \ldots, \tag{B.24}$$

$$Y_i = G(X_i, t_i) + \epsilon_i = G(X_i^*, t_i) + \left[\frac{\partial G}{\partial X}\right]_i^* x_i + \ldots + \epsilon_i. \tag{B.25}$$

If higher order terms are neglected, these expressions become:

$$\dot{x}(t) = A(t)x(t), \tag{B.26}$$

$$y_i = \tilde{H}_i x_i + \epsilon_i, \quad i = 1, \ldots, l \tag{B.27}$$

where,

$$A(t) = \left[\frac{\partial F}{\partial X}\right]^*$$

$$\tilde{H}_i = \left[\frac{\partial G}{\partial X}\right]_i^*$$

This is a system of linear differential equations with time-dependent coefficients whose solution can be expressed by:

$$x(t) = \Phi(t, t_0)x_0 \tag{B.28}$$

where the $n \times n$ state transition matrix, $\Phi(t, t_0)$, satisfies the differential equation:

$$\dot{\Phi}(t, t_0) = A(t)\Phi(t, t_0), \quad \Phi(t_0, t_0) = I, \tag{B.29}$$

where I is the $n \times n$ identity matrix. Using Equation B.28, the linear observation equation becomes

$$y_i = \tilde{H}_i\Phi(t_i, t_0)x_0 + \epsilon_i, \quad i = 1, \ldots, l, \tag{B.30}$$

Thus, the original nonlinear estimation problem has been reformulated as a linear estimation in terms of the difference of the state from the nominal trajectory at the initial epoch and the observation residuals. In order to minimize the effects of neglecting higher order terms, an iterative solution procedure is used.

B.1.4 Estimation Algorithm

The solution of the overdetermined linear system derived in the previous section is different for dynamic and reduced-dynamic techniques. Both approaches use least-squares filters; a filter is a computational algorithm that processes observations to generate a minimum error estimate of the state of the system using knowledge of the system and measurement dynamics, assumed

statistics of the system noises and measurement errors, and initial condition information [24].

The most commonly used filtering approach in POD is the epoch state batch filter, where all data in a batch are mapped backwards to some specified epoch and are processed simultaneously to obtain an estimate of the state at that time. State estimates at future times are obtained by mapping the epoch state forward using the equations of motion. The batch filter has been used since the late 1950's to provide POD for geodetic satellites. For gravity estimation, a large number of observations mapped to the same reference epoch is required to estimate all of the parameters and reduce the effect of random noise. For this reason, an epoch-state batch filter is used for GRACE POD processing at UT/CSR.

B.1.4.1 Epoch-State Batch Filter

The batch filter is obtained by using the state transition matrix to relate all observations to some specified epoch. We start by defining

$$y = Hx + \epsilon, \tag{B.31}$$

where,

$$y = \begin{bmatrix} y_1 \\ \vdots \\ y_l \end{bmatrix}, H = \begin{bmatrix} \tilde{H}_1\Phi(t_1, t_0) \\ \vdots \\ \tilde{H}_l\Phi(t_l, t_0)l \end{bmatrix}, \epsilon = \begin{bmatrix} \epsilon_1 \\ \vdots \\ \epsilon_l \end{bmatrix}. \tag{B.32}$$

Note that y and ϵ are m vectors ($m = l \times p$), and H is an $m \times n$ matrix. Therefore, Equation B.19 is a system of m equation and n unknowns. In

orbit determination, there are more observations than estimated parameters ($m > n$), which means that the system is overdetermined.

Assuming that the observation errors, ϵ, are random with zero mean $E[\epsilon] = 0$ and satisfies $E[\epsilon\epsilon^{\mathrm{T}}] = W^{-1}$, we can scale each term by $W^{1/2}$ to get the condition

$$W^{1/2}E[\epsilon\epsilon^{\mathrm{T}}]W^{\mathrm{T}/2} = W^{1/2}W^{-1}. \tag{B.33}$$

Now consider the following quadratic performance index,

$$J = \frac{1}{2}\|W^{1}2(Hx - y)\|^2 = \frac{1}{2}(Hx - y)^{\mathrm{T}}W(Hx - y) \tag{B.34}$$

The solution to this weighted least-squares estimation problem (which is equivalent to the minimum variance and maximum likelihood estimation problem, under certain restrictions [1]) is obtained by finding the value $\hat{x}$ that minimizes Equation B.34. This is shown in [1] to be

$$\hat{x}_0 = (H^{\mathrm{T}}R^{-1}H)^{-1}(H^{\mathrm{T}}R^{-1}y), \tag{B.35}$$

where the weighting matrix W equals R^{-1}. The covariance matrix associated with this estimate is

$$P_0 = (H^{\mathrm{T}}R^{-1}H)^{-1}. \tag{B.36}$$

If an *a priori* estimate of the epoch state $\bar{x}_0$ and state covariance matrix $\bar{P}_0$ are available, then Equations B.35 and B.36 become:

$$\hat{x}_0 = (H^{\mathrm{T}}R^{-1}H + \bar{P}_0^{-1})^{-1}(H^{\mathrm{T}}R^{-1}y + \bar{P}_0^{-1}\bar{x}_0), \tag{B.37}$$

$$P_0 = (H^{\mathrm{T}}R^{-1}H + \bar{P}_0^{-1})^{-1}. \tag{B.38}$$

B.1.4.2 Estimation via Orthogonal Transformation

Computing the solution from Equations B.35 or B.37 requires the inversion of an n-dimensional square matrix. When this number is large, as is the case for the dynamic POD problem, the matrix can be ill-conditioned. This implies that an explicit inversion is numerically unstable. Therefore, the method employed in GRACE POD processing at UT/CSR is to reformulate the problem and solve via orthogonal rotations. These methods are analogous to Gauss-Jordan elimination techniques, with the exception that orthogonal transformations preserve the unit covariance property of the noise term.

To achieve this, let Q be an $m \times m$ orthogonal matrix; therefore, the performance index can be rewritten as

$$J = \frac{1}{2}\|QW^{1/2}(Hx - y)\|^2, \tag{B.39}$$

If Q is selected such that

$$QW^{1/2}H = \begin{bmatrix} R \\ 0 \end{bmatrix}, \quad QW^{1/2}y = \begin{bmatrix} b \\ e \end{bmatrix}, \tag{B.40}$$

where R is $n \times n$ upper-triangular, 0 is an $(m-n) \times n$ null matrix, b is a $n \times 1$ vector, and e is an $(m-n) \times 1)$ vector, the performance index becomes:

$$J(x) = \frac{1}{2}\|Rx - b\|^2 + \frac{1}{2}\|e\|^2, \tag{B.41}$$

The value of x which minimizes this is obtained by the solution,

$$R\hat{x} = b, \tag{B.42}$$

and is obtained through simple back substitution. Given this, the minimum value of the performance index becomes

$$J(\hat{x}) = \frac{1}{2}\|e\|^2 = \frac{1}{2}\|y - h\hat{x}\|^2, \tag{B.43}$$

In addition to the estimate, the covariance of the solution is obtained from

$$P = R^{-1}R^{-\mathrm{T}}, \tag{B.44}$$

and only involves the inversion of an upper triangular matrix.

Therefore, the procedures are direct and implementation requires only a convenient computational procedure for $QW^{1/2}H$ and $QW^{1/2}y$ [3]. The Givens method, based on a series of orthogonal rotations, is used for accumulation and solution in MSODP [3].

B.1.5 Parameterization for Multi-Satellite Orbit Determination

The orbit determination problem is highly parameterized. Parameters can be divided into two groups: dynamic and kinematic. Dynamic parameters need to be mapped into other states by using the state transition matrix, which is usually computed by numerical integration, while kinematic parameters are treated as constant throughout the computation. Dynamic parameters can be grouped again into two parts: local and global. Local parameters are satellite-specific, while global parameters influence every satellite (i.e., gravitational forces).

Following this parameterization, the estimation state vector is defined

as

$$X \equiv \begin{bmatrix} X_{KP} \\ X_{SS} \\ X_{LDP} \\ X_{GDP} \end{bmatrix}, \tag{B.45}$$

where,

$X_{KP} =$ the kinematic parameters,

$X_{SS} = [X_{POS}, X_{VEL}]^{\mathrm{T}} =$ the satellite states,

$X_{LDP} =$ the local dynamic parameters,

$X_{GDP} =$ the global dynamic parameters.

The resulting equations of motion and state transition matrix can be found in [3].

B.2 Reduced-Dynamic Orbit Determination

The reduced-dynamic orbit determination POD strategy uses the classical epoch state batch filter to generate a converged dynamic reference trajectory which is then used by a sequential filter for the final pass through the data [5]. The sequential filtering includes state noise compensation to combine geometric information from GPS with dynamic information contained in satellite force models. Empirical accelerations are included as process noise. GPS data density, geometry, and precision could be exploited by combining the geometric approach associated with GPS and the dynamic approach typically associated with SLR and DORIS systems, leading to the reduced-dynamic

method. The term reduced-dynamic orbit determination comes from the reduced susceptibility of the sequential process noise filter to dynamic model errors in comparison to the classical batch filter [24].

B.2.1 Empirical Accelerations

The reduced-dynamic solution is produced only in the final estimation step. First, a converged dynamic solution is obtained using a btach filter. The residuals from the batch filter contain unique information about the remaining orbit errors that can be exploited by the geometric strength of GPS observations. In the reduced-dynamic step, adjustments are made to the spacecraft state and all previously adjusted parameters except two types: the empirical once and twice-per revolution terms (which are now held fixed) and the constant accelerations [5]. The accelerations are now treated as process noise vectors that represent unmodeled or mismodeled body-fixed accelerations. This is re-estimated at each time step to allow high frequency due to gravity and atmospheric drag to be accommodated in a manner that is difficult to achieve with an epoch state batch filter. Each component of the acceleration in the RTN directions is modeled as a first-order Gauss-Markov process constrained by an assigned correlation time and steady-state uncertainty.

B.2.2 Sequential Filter

Although the sequential estimation algorithms have had wide use in autonomous navigation and control applications, they have not received much

attention for use with POD of LEOs. This is primarily due to filter divergence, which is when the estimate of the state departs from the true value.

Though early studies indicated some potential advantages of sequential filtering, it was not suited for geophysical model improvement. In addition, the noisy, sparse data provided by traditional SLR and DORIS tracking systems had errors and data gaps that would cause the sequential filter to diverge [24]. It was not until the development of GPS that interest in sequential filtering for POD was renewed. The continuous tracking provided by a space-based tracking system, coupled with the potential precision of the GPS observables, was ideally suited for a sequential filter where process noise is used to compensate for high-frequency orbit errors associated with the geopotential.

The Kalman form of the sequential filter derived from the batch filter (including an *a priori* estimate) is given by [1]:

$$P_0 = \bar{P}_0 - \bar{P}_0 \tilde{H}_0^{\mathrm{T}} [\tilde{H}_0 \bar{P}_0 \tilde{H}_0^{\mathrm{T}} + R_0]^{-1} \tilde{H}_0 \bar{P}_0. \tag{B.46}$$

Note that the matrix to be inverted has the same dimensions as the observation error covariance matrix. If the weighting matrix (i.e., Kalman gain), K_k, is defined as

$$K_0 \equiv \bar{P}_0 \tilde{H}_0^{\mathrm{T}} [\tilde{H}_0 \bar{P}_0 \tilde{H}_0^{\mathrm{T}} + R_0]^{-1}, \tag{B.47}$$

then Equation B.46 can be expressed in a more compact form

$$P_0 = [I - K_0 \tilde{H}_0] \bar{P}_0 \tag{B.48}$$

If Equation B.46 is substituted into Equation B.37 and simplified, the sequential form for computing the estimate can be written as [1]:

$$\begin{aligned}\hat{x}_0 =& P_k[\tilde{H}_0^{\mathrm{T}} R_k^{-1} y_k + \bar{P}_k^{-1}\bar{x}_0], \\ =& \bar{x}_0 + K_0[y_0 - \tilde{H}_0\bar{x}_0].\end{aligned} \tag{B.49}$$

The sequential filter provides an estimate of the state at each measurement time based upon observations until that time. The sequential filter is generally associated with obtaining an estimate of the current state, although state estimates in the past may be obtained by employing a technique called smoothing which operates in reverse time order. In this form of the sequential filter, it is equivalent to the batch filter. Therefore, given the same input data, both algorithms should produce the same estimate when mapped to the same epoch.

B.2.3 Sequential Filter with Process Noise

Inaccuracies in the dynamical model can lead to divergence in the estimate. For a sufficiently large number of observations, the sequential filter can become saturated [45], that is the elements of the covariance matrix asymptotically approaching zero, and the filter will ignore any new data, leading to divergence [1]. To prevent this, it is assumed that the error in the linearized dynamics can be approximated by process noise.

The state dynamics of a linear system under the influence of process

noise is given by:

$$\dot{x}(t) = A(x)x(t) + B(t)u(t), \tag{B.50}$$

where $A(t)$ and $B(t)$ are known functions of time. The functional form of $u(t)$ can include a number of processes, including constant, piecewise constant, correlated, or white noise [1]. In this case, it is assumed to be a white noise process with the following properties:

$$E[u(t)] = 0, \quad E[u(t)u^{\mathrm{T}}(t)] = Q(t)\delta(t-\tau), \tag{B.51}$$

where $\delta(t-\tau)$ is the Dirac Delta function and Q is the process noise covariance matrix. Using the method of variation of parameters, it can be shown that the solution to Equation B.50 is [1]:

$$x(t) = \Phi(t, t_0)x_0 + \int_{t_0}^{t} \phi(t, \tau)G(\tau)u(\tau)\mathrm{d}\tau. \tag{B.52}$$

The equations for propagating the state estimate and error covariance matrix are given by

$$\bar{x}(t) = \Phi(t, t_0)\hat{x}_0, \tag{B.53}$$

$$\bar{P}(t) = \Phi(t, t_0)P_0\Phi^{\mathrm{T}}(t, t_0) + \int_{t_0}^{t} \Phi(t, \tau)G(\tau)Q(\tau)G^{\mathrm{T}}(\tau)\Phi^{\mathrm{T}}(t, \tau)\mathrm{d}\tau. \tag{B.54}$$

Note that these equations are for a continuous time system. However, the POD problem is a continuous system (i.e., the trajectory) subjected to discrete observations from tracking data [1]. The equations are discretized by replacing t with t_{k+1} and t_0 with t_k and assuming that $u(\tau)$ is a white random

sequence rather than a process. Therefore, $u(t)$ is now considered to be a piecewise constant function with covariance

$$E[u(t_i)u^{\mathrm{T}}(t_j)] = Q_i\delta_{ij}, \quad \text{where } \delta_{ij} = \begin{cases} 1, & i = j \\ 0, & i \neq j \end{cases} \tag{B.55}$$

where the Dirac delta function has been replaced with the Kroneker delta function, its equivalent in the discrete case. The equations for propagating the state estimate and error covariance matrix (Equations B.53 and B.54) become:

$$\bar{x}(t_{k+1}) = \Phi(t_{k+1}, t_k)x_k + \Gamma(t_{k+1}, t_k)u_k, \tag{B.56}$$

$$\bar{P}_{k+1} = \Phi(t_{k+1}, t_k)P_k\Phi^{\mathrm{T}}(t_{k+1}, t_k) + \Gamma(t_{k+1}, t_k)Q_k\Gamma^{\mathrm{T}}(t_{k+1}, t_k), \tag{B.57}$$

where,

$$\Gamma(t_{k+1}, t_k) = \int_{t_k}^{t_{k+1}} \Phi(t_{k+1}, \tau)B(\tau)\mathrm{d}\tau. \tag{B.58}$$

Γ is referred to as the process noise transition matrix. Finally, it is important to note that the equations to determine the estimate, covariance, and for propagating the estimate are not affected by including process noise; only the propagation of the error covariance matrix is affected.

B.2.4 Smoothing

The sequential filter is based upon a recursive procedure that uses data up to the current epoch to estimate the state so only the current state is adjusted using all of the data in the arc. In the POD process, it is desired to use all of the data in the arc to obtain the best estimate of the state at each

epoch. This is accomplished with a process called smoothing, which entails filtering the data in reverse time order using the terminal state and covariance obtained in the forward filter pass as the *a priori* state and covariance for the backward filter pass. Eventually, the epoch state and covariance adjusted based on all of the data in the arc. A smoothing algorithm for a sequential filter with process noise can be found in [1]. This is based on the approach of Jazwinski [REF], which uses a Bayesian method of maximizing the density function of the state conditioned on knowledge of the observations through the current epoch. The result is equivalent to the Rauch, Tung, and Striebel smoother [1].

The Rauch-Tung-Striebel (RTS) equations [24] provide a smoothing recursion compatible with the sequential Kalman filter with process noise:

$$x_j^* = \hat{x}_j + C_j(x_{j+1}^* - \tilde{x}_{j+1}), \tag{B.59}$$

$$P_j^* = \hat{P}_h + C_j(P_{j+1}^* - \tilde{P}_{j_1}), C_j^{\mathrm{T}}, \tag{B.60}$$

where,

$$C_j = \hat{P}_j \Phi_j^{\mathrm{T}} P_{j+1}^{-1}. \tag{B.61}$$

In these equations, $(\sim)$ denotes a predicted or propagated quantity, $(\wedge)$ indicates a filtered quantity, and $(*)$ indicates a smoothed quantity. From these equations, it can be seen that the smoothed estimate at t_j is the weighted sum of the filtered estimate and difference of the smoothed and predicted estimates at t_{j+1}. The weighting matrix multiplying the difference of the smoothed and predicted estimates is called the smoother gain matrix and is a function of the

filtered covariance at t_j, the predicted covariance at t_{j+1}, and the state transition matrix. The smoothed covariance is the filtered covariance plus a term that is a function of the difference of the smoothed and predicted covariances at t_{j+1} and the smoother gain matrix.

B.2.5 Square Root Information Filter

One of the primary causes of filter divergence are errors that occur in the measurement update of the state error covariance matrix. Specifically, this matrix can become non-positive definite. Since this is related to errors introduced during the computational procedure, it is possible to reformulate the computational process to minimize the effects of such errors. One approach is to use square root solution methods where the state error covariance matrix is replaced by its square root.

As previously mentioned, the sequential process noise filter implemented in GIPSY-OASIS is based on a factored formulation known as the SRIF. This algorithm is derived from factoring the information equations (i.e., the normal equations) rather than the state error covariance matrix. The SRIF filter's main strength is that it is numerically stable and computationally efficient. It avoids the problem of inverting a large matrix by inverting several small matrices that are sequentially created for each time interval.

To derive this formulation as based on [1], consider the case where the state vector, x, is a constant. Assume that *a priori* information of the state, $\bar{x}$, and information matrix $\bar{\Lambda} = \bar{P}^{-1}$ are provided. This can be added to the

form of a data equation by noting that

$$\bar{x} = x + \eta, \tag{B.62}$$

where η is the error in $\bar{x}$ and is assumed to have the following properties:

$$E[\eta] = 0, E[\eta\eta^{\mathrm{T}}] = \bar{P} = \bar{\Lambda}^{-1}. \tag{B.63}$$

Factoring the information matrix yields

$$\bar{\Lambda} = \bar{R}^{\mathrm{T}}\bar{R}. \tag{B.64}$$

Multiplying Equation B.62 by $\bar{R}$ yields,

$$\bar{R}\bar{x} = \bar{R}x + \bar{R}\eta. \tag{B.65}$$

Defining,

$$\bar{b} = \bar{R}\bar{x}, \bar{\eta} = \bar{R}\eta, \tag{B.66}$$

the standard form of the data equation becomes,

$$\bar{b} = \bar{R}x + \bar{\eta}. \tag{B.67}$$

Note that the error $\bar{\eta}$ still has zero mean, but now has unit variance,

$$E[\bar{\eta}] = \bar{R}E[\eta] = 0, \tag{B.68}$$

$$E[\eta\eta^{\mathrm{T}}] = \bar{R}E[\eta\eta^{\mathrm{T}}]\bar{R}^{\mathrm{T}} = \bar{R}\bar{P}\bar{R}^{\mathrm{T}} = I. \tag{B.69}$$

In order to determine the "best" estimate of x given the *a priori* information in Equation B.67 and observation equation, the performance index becomes:

$$\begin{aligned} J(x) &= \|\epsilon\|^2 + \|\bar{\eta}\|^2, \\ &= \|Hx - y\|^2 + \|\bar{R}x - \bar{b}\|^2, \\ &= \left\| \begin{bmatrix} \bar{R} \\ H \end{bmatrix} x - \begin{bmatrix} \bar{b} \\ y \end{bmatrix} \right\|^2. \end{aligned} \tag{B.70}$$

Applying a series of orthogonal transformations, such that

$$T \begin{bmatrix} \bar{R} & \bar{b} \\ H & y \end{bmatrix} = \begin{bmatrix} R & b \\ 0 & e \end{bmatrix}, \tag{B.71}$$

the performance index becomes

$$J(x) = \left\| \begin{bmatrix} R \\ 0 \end{bmatrix} x - \begin{bmatrix} b \\ e \end{bmatrix} \right\|^2 = \|Rx - b\|^2 + \|e\|^2. \tag{B.72}$$

Therefore, the value of x that minimizes this is simply,

$$\hat{x} = R^{-1}b, \tag{B.73}$$

and is most easily solved by backward substitution [1].

To consider how process noise is included in the SRIF, we start with a more general form of Equation B.56:

$$x_k = \Phi(t_k, t_{k-1})x_{k-1} + \Gamma(t_k, t_{k-1})u_{k-1}. \tag{B.74}$$

The state vector is partitioned into the state and process noise parameters. Bias parameters are neglected in this derivation. There is no loss of generality since row permutations and orthogonal transformations can be used to

de-couple this term from those involving the satellite state and process noise parameters [24]. The process noise parameters can be a combination of dynamic orbit-related parameters, i.e. body-fixed accelerations, or non-dynamic station and satellite parameters such as tropospheric zenith delays and clock offsets [24].

Assuming that at time t_{k-1} there is an *a priori* information array $[\bar{R}_{k-1}\bar{b}_{k-1}]$ from a previous solution, the information available to compute the estimate at t_{k-1} is

$$\bar{b}_{k-1} = \bar{R}_{k-1}\bar{x}_{k-1}, \tag{B.75}$$

but,

$$\bar{x}_{k-1} = x_{k-1} + \eta_{k-1} \tag{B.76}$$

where x_{k-1} is the true value. Additionally,

$$E[\eta_{k-1}] = 0, \tag{B.77}$$

$$E[\eta_{k-1}\eta_{k-1}^{\mathrm{T}}] = I. \tag{B.78}$$

Substituting Equation B.76 into B.75, the data equation for the *a priori* is obtained as:

$$\bar{b}_{k-1} = \bar{R}_{k-1}x_{k-1} + \bar{\eta}_{k-1}, \tag{B.79}$$

where

$$E[\bar{\eta}_{k-1}] = \bar{R}_{k-1}E[\eta_{k-1}] = 0, \tag{B.80}$$

$$E[\bar{\eta}_{k-1}\bar{\eta}_{k-1}^{\mathrm{T}}] = \bar{R}_{k-1}\bar{P}_{k-1}\bar{R}_{k-1}^{\mathrm{T}} = I. \tag{B.81}$$

A scalar observation is given at t_{k-1} as

$$y_{k-1} = H_{k-1}x_{k-1} + \epsilon_{k-1}. \tag{B.82}$$

A priori information on u_{k-1} is given by u_{k-1} (i.e., the mean value of u) and its covariance Q. Generally it is assumed that u is a zero mean process so that the *a priori* value $\bar{u} = 0$ at each stage. This information also may be written in the form of a data equation by nothing that,

$$\bar{u} = \bar{u}_{k-1} = u_{k-1} + \alpha_{k-1}, \tag{B.83}$$

where $\bar{u}_{k-1}$ is the *a priori* value and u_{k-1} is the true value. The error, α_{k-1}, has the properties:

$$E[\alpha_{k-1}] = 0, \tag{B.84}$$

$$E[\alpha_{k-1}\alpha_{k-1}^{\mathrm{T}}] = Q. \tag{B.85}$$

Next, assume that the process noise is uncorrelated in time (i.e. $E[\alpha_i\alpha_j^{\mathrm{T}}] = 0$ for $i \neq j$ and that both u and Q are constant in time. Q can be factored such that

$$R_u^{-1}R_u^{-\mathrm{T}} = Q. \tag{B.86}$$

Pre-multiplying by R_u, the data equation for $\bar{u}_{k-1}$ becomes

$$R_u\bar{u}_{k-1} = \bar{b}_{u_{k-a}} = R_u u_{k-1} + \bar{\alpha}_{k-1}. \tag{B.87}$$

Now, we define a performance index for the measurement update at t_{k-1} based on the previous equations,

$$\hat{J}_{k-1} = \|\bar{\eta}_{k-1}\|^2 + (\epsilon_{k-1})^2 + \|\bar{\alpha}_{k-1}\|^2. \tag{B.88}$$

By substitution and using orthogonal transformations, this is reduced to

$$\hat{J}_{k-1} = (e_{k-1})^2 + \|\hat{R}_{k-1}x_{k-1} - \hat{b}_{k-1}\|^2 + \|R_u u_{k-1} - \bar{b}_{u_{k-1}}\|^2. \tag{B.89}$$

The minimum value of $\hat{J}_{k-1}$ is found by setting

$$\hat{R}_{k-1}\hat{x}_{k-1} = \hat{b}_{k-1}, \tag{B.90}$$

$$R_u \bar{u}_{k-1} = \bar{b}_{u_{k-1}}, \tag{B.91}$$

which results in

$$\hat{J}_{k-1} = (e_{k-1})^2. \tag{B.92}$$

With measurement update at t_{k-1} completed, the time update to t_k is next. In order to update the performance index, Equation B.89 must be rewritten in terms of x_k. Note that because u_{k-1} is not time dependent, u will be updated to t_k in the measurement update. Now, rewriting x_{k-1} in terms of x_k,

$$x_{k-1} = \Phi^{-1}(t_k, t_{k-1})(x_k - \Gamma(t_k, t_{k-1})u_{k-1}). \tag{B.93}$$

Substituting Equation B.93 into B.89 results in

$$\begin{aligned}\bar{J}_k =&(e_k - 1)^2 + \|\hat{R}_{k-1}\Phi^{-1}(t_k, t_{k-1})(x_k - \Gamma(t_k, t_{k-1})u_{k-1}) - \hat{b}_{k-1}\|^2 \\ &+ \|R_u u_{k-1} - \bar{b}_{u_{k-1}}\|^2,\end{aligned} \tag{B.94}$$

which can be rewritten as

$$\bar{J}_k = (e_k - 1)^2 + \left\| \begin{bmatrix} R_u & 0 \\ -\tilde{R}_k\Gamma(t_k, t_{k-1}) & \tilde{R}_k \end{bmatrix} \begin{bmatrix} u_{k-1} \\ x_k \end{bmatrix} - \begin{bmatrix} \bar{b}_{u_{k-1}} \\ \hat{b}_{k-1} \end{bmatrix} \right\|^2, \tag{B.95}$$

where,

$$\tilde{R}_k \equiv \hat{R}_{k-1}\Phi^{-1}(t_k, t_{k-1}).$$

Now, applying a series of q orthogonal transformations to the second term of the previous equation, the explicit dependence of x_k on u_{k-1} can be eliminated

$$\bar{T}_k \begin{bmatrix} R_u & 0 & \bar{b}_{u_{k-1}} \\ -\tilde{R}_k\Gamma(t_k, t_{k-1}) & \tilde{R}_k & \hat{b}_{k-1} \end{bmatrix} = \begin{bmatrix} \bar{R}_{u_k} & \bar{R}_{ux_k} & \tilde{b}_{u_k} \\ 0 & \bar{R}_k & \bar{b}_k \end{bmatrix}. \tag{B.96}$$

The resulting performance index is

$$\bar{J}_k = (e_k - 1)^2 + \left\| \begin{bmatrix} R_{u_k} & \bar{R}_{ux_k} \\ 0 & -\bar{R}_k \end{bmatrix} \begin{bmatrix} u_{k-1} \\ x_k \end{bmatrix} - \begin{bmatrix} \tilde{b}_{u_k} \\ \bar{b}_k \end{bmatrix} \right\|^2, \tag{B.97}$$

or,

$$\bar{J}_k = (e_k - 1)^2 + \|\bar{R}_{u_k}u_{k-1} + \bar{R}_{ux_k}x_k - \tilde{b}_{u_k}\|^2 + \|\bar{R}_k x_k - \bar{b}_k\|^2. \tag{B.98}$$

The minimum value of J is obtained by solving

$$\bar{R}_{u_k}u_{k-1} + \bar{R}_{ux_k}x_k = \tilde{b}_{u_k}, \tag{B.99}$$

$$\bar{R}_k x_k = \bar{b}_k. \tag{B.100}$$

to obtain

$$\bar{x}_k = \bar{R}_k^{-1}\bar{b}_k. \tag{B.101}$$

Because R_{u_k} is nonsingular we can find a value of u_{k-1} that satisfies Equation B.99 for any value of x_k. The resulting value from Equation B.101 of $\bar{x}_k$ is:

$$\bar{x}_k = \Phi(t_k, t_{k-1})\hat{x}_{k-1} + \Gamma(t_k, t_{k-1})\bar{u}_{k-1}, \tag{B.102}$$

where $\bar{u}_{k-1}$ is the *a priori* value.

We may now do the measurement update at t_k. The least squares performance index for the measurement update is

$$\begin{aligned}\hat{J}_k &= \bar{J}_k + (\epsilon_k)^2 + \|\bar{\alpha}_k\|^2, \\ &= \bar{J}_k + (H_k x_k - y_k)^2 + \|\bar{\alpha}_k\|^2,\end{aligned} \tag{B.103}$$

This may be written as

$$\begin{aligned}\hat{J}_k =&(e_k - 1)^2 + \|\bar{R}_{u_k} u_{k-1} + \bar{R}_{ux_k} x_k - \tilde{b}_{u_k}\|^2 \\ &+ \left\| \begin{bmatrix} \bar{R}_k \\ H_k \end{bmatrix} x_k - \begin{bmatrix} \bar{b}_k \\ y_k \end{bmatrix} \right\|^2 + \|R_u u_k - \bar{b}_{u_k}\|^2.\end{aligned} \tag{B.104}$$

Applying orthogonal transformations to the third term:

$$\begin{aligned}\hat{J}_k =&(e_k - 1)^2 + \|\bar{R}_{u_k} u_{k-1} + \bar{R}_{ux_k} x_k - \tilde{b}_{u_k}\|^2 \\ &+ \|\hat{R}_k x_k - \hat{b}_k\|^2 + (e_k)^2 + \|R_u u_k - \bar{b}_{u_k}\|^2.\end{aligned} \tag{B.105}$$

Similarly to before, the $\hat{J}_k$ is minimized by setting u_{k+1}, u_k, and x_k to zero. This eliminates all but the $(e)^2$ terms, resulting in

$$\hat{J}_k = (e_{k-1})^2 + (e_k)^2. \tag{B.106}$$

The time update to obtain $\bar{J}_{k+1}$ may now be obtained by substituting

$$x_k = \Phi^{-1}(t_{k+1}, t_k)(x_{k+1} - \Gamma(t_{k+1}, t_k) u_k), \tag{B.107}$$

for x_k in the third term of Equation B.105. Therefore, the general expression for the time update at t_m after processing $m-1$ observations is

$$\bar{J}_m = \sum_{i=1}^{m-1} (e_i)^2 + \sum_{i=1}^{m-1} \|\bar{R}_{u_i} u_{i-1} + \bar{R}_{ux_i} - \tilde{b}_{u_i}\|^2 \tag{B.108}$$

$$\left\| \begin{bmatrix} \bar{R}_m \\ H_m \end{bmatrix} x_m - \begin{bmatrix} \bar{b}_m \\ y_m \end{bmatrix} \right\|^2. \tag{B.109}$$

The measurement update for processing m observations is obtained by adding data equations for the mth observation, upper triangularizing the third term of the previous equation, and then applying an orthogonal transformation:

$$\hat{J}_m = \sum_{i=1}^{m} (e_i)^2 + \sum_{i=1}^{m} \| \bar{R}_{u_i} u_{i-1} + \bar{R}_{ux_i} x_i - \tilde{b}_{u_i} \|^2 \tag{B.110}$$

$$+ \| R_u u_m - \bar{b}_{u_m} \|^2 + \| \hat{R}_m x_m - \hat{b}_m \|^2. \tag{B.111}$$

From observation, $\hat{J}_m$ is minimzed by choosing

$$\hat{x}_m = \hat{R}_m^{-1} \hat{b}_m, \tag{B.112}$$

and

$$\bar{R}_{u_i} \hat{u}_{i-1} = \tilde{b}_{u_i} - \bar{R}_{ux_i} \hat{x}_i; \quad i = m, m-1, \ldots 1. \tag{B.113}$$

Note that the third term in the performance index is simply the addition of *a priori* information on u_m and does not affect the performance index until we perform a time and measurement update at t_{m+1}. Finally, it should be noted that while only $\hat{u}$ is needed for filtering, the quantities $\bar{R}_u$, $\bar{b}_u$, and $\bar{R}_{ux}$ are needed in order to perform smoothing. To see how this is implemented, please refer to [1] or [24].

B.2.5.1 Process Noise Parameter Filtering Using a SRIF

In the reduced-dynamic method several parameters are included in filtering the satellite data to improve the solution. Consider a more general form of the state equations such that

$$x_{k+1} = \Phi_x(t_{k+1}, t_k) t_k + \Phi_p(t_{k+1}, t_k) p_k + \Phi_c(t_{k+1}, t_k) c \tag{B.114}$$

The state vector is partitioned into the spacecraft state, correlated process noise parameters, and the vector of bias parameters, x, p, and c, respectively. The process noise parameters can be a combination of dynamic orbit-related parameters, such as body-fixed accelerations or radiation pressure scaling coefficients, as well as kinematic parameters such as tropospheric zenith delays and clock offsets. The SRIF formulation can be modified to handle bias parameters and first-order exponentially correlated noise. The state propagation equations can be expressed as

$$\begin{bmatrix} p \\ x \\ c \end{bmatrix}_{k+1} = \begin{bmatrix} M & 0 & 0 \\ \Phi_p & \Phi_x & \Phi_c \\ 0 & 0 & I \end{bmatrix}_{k+1} \begin{bmatrix} p \\ x \\ c \end{bmatrix}_k + \begin{bmatrix} w_k \\ 0 \\ 0 \end{bmatrix}, \tag{B.115}$$

where Φ_p, Φ_x, and Φ_c are the state transition matrices that map p, x, and c, respectively, at t_k to t_{k+1}. Defining,

$$X_{k+1} \equiv \begin{bmatrix} p \\ x \\ c \end{bmatrix}_{k+1}, \Phi(t_{k+1}, t_k) \equiv \begin{bmatrix} M & 0 & 0 \\ \Phi_p & \Phi_x & \Phi_c \\ 0 & 0 & I \end{bmatrix}_{k+1}, \Gamma(t_{k+1}, t_k) \equiv \begin{bmatrix} I \\ 0 \\ 0 \end{bmatrix}, \tag{B.116}$$

Equation B.114 can be written as

$$X_{k+1} = \Phi(t_{k+1}, t_k) X_k + \Gamma(t_{k+1}, t_k) w_k, \tag{B.117}$$

meaning that all of the previously derived equations for the SRIF are still valid.

The most frequently used models for propagating the state noise and covariance are first-order Gauss-Markov (i.e., white noise) and random walk. The first-order Gauss-Markov process provides for an exponentially decaying

correlation. The recursive equation for mapping a discrete first order exponentially correlated process is [1]:

$$p_{k+1} = M_{k+1} p_j k + w_k, \tag{B.118}$$

where M is a diagonal process noise mapping matrix, with the diagonal entries, m, given by

$$m = e^{-(t_{k+1}-t_k)/\tau} \tag{B.119}$$

where τ, the time constant of the process, represents how correlated a process noise parameter is from one time step to the next. Note that w in Equation B.118 is called the process noise with the property that $E[w_j] = \bar{w}_j$. The *a priori* estimate of $\bar{w}_j$ is typically assumed to be zero. Next,

$$E[(w_j - \bar{w}_j)(w_k - \bar{w}_k)^{\mathrm{T}}] = Q\delta_{jk}, \tag{B.120}$$

and

$$Q = R_w^{-1} R_w^{-\mathrm{T}}, \tag{B.121}$$

where Q is the process noise covariance. The corresponding diagonal entries of Q are given by,

$$q_i = (1 - m_i^2)\sigma_i^2. \tag{B.122}$$

Note that σ_i is the steady-state uncertainty of the process noise, i.e., the variance corresponding to the particular process noise parameter p_i. This is the level of noise that would be reached if the system were left undisturbed for a time much greater than τ, the correlation time.

The models for the white noise and random walk processes can be considered limiting cases of the Gauss-Markov model for appropriate values of τ and σ_i. This allows the use of a single process noise model to represent several different aspects of unmodeled or mismodeled forces. For example, white process noise is obtained by setting $\tau = 0$, which yields $m = 0$ and resets the covariance to the steady-state variance. This is typically used to model the satellite clocks, but it can also be used for drag or radiation pressure scaling coefficients.

The other case is random walk. In this case, both τ and σ_i are unbounded and a steady-state is never reached. M is the identity matrix and it is the rate of change of the process noise covariance, $\dot{q} = \mathrm{d}q/\mathrm{d}t = \Delta q/\Delta t$, which characterizes the process. Here, Δt is the batch time interval and Δq is the amount of noise added per batch which can be related to the Allan variance, $\sigma_A^2(\Delta t) = \dot{q}/\Delta t$. Random walk is used to model the wet zenith delays at the tracking stations.

When the correlation time is set to zero, the accelerations are uncorrelated from one time step to the next, resulting in the white noise model. If the steady-state variance is made large, the corrections at each measurement time are unconstrained by the dynamics and are determined by the GPS data, i.e., $Q \to \infty$ causes $\bar{P} \to \infty$ such that contribution of the data to the estimate greatly outweighs that dynamic model. The resulting position solution is therefore largely geometric and is minimally affected by the dynamic model. On the other hand, when the steady-state variance is set to zero, then $Q \to 0$

causes $\bar{P} \to 0$ and the dynamic reference orbit is retained. This is the key concept of reduced-dynamic orbit determination. The steady-state variance of the process noise is adjusted to give the optimal relative weight between the dynamic information from the reference orbit and the geometric information from the GPS data. The integrated effect of the process noise parameters results in local, point-by-point geometric corrections to the dynamic orbit. In theory, this optimal weighting procedure balances dynamic, geometric, and measurement errors to yield an orbit that surpasses the dynamic solution [24].

B.2.6 Pseudo-Epoch State Formulation

The formulation of the sequential SRIF given in the previous section was in terms of the current state. However, the implementation in GIPSY-OASIS is in terms of the pseudo-epoch state. Since the batch filter is referenced to the epoch state and the sequential filter is formulated in terms of the current state and requires transition matrices from each measurement epoch to the next, the pseudo-epoch state was introduced so that process noise can be included while preserving the epoch state formulation.

The derive the pseudo-epoch state formulation, we rewrite the dynamics of the satellite state as

$$x(t_{j+1}) = \Phi(t_{j+1}, t_j)x(t_j) + \Phi(t_{j+1}, t_j)p + \Phi(t_{j+1}, t_j)c \tag{B.123}$$

The time t_k has been replaced with t_{j+1} and the subscripts of p and c have been dropped since these parameters are assumed to be constant over the

batch interval. The batch interval is the length of time over which data is used to obtain the satellite ephemerides.

Now the current state, $x(t_j)$, and the pseudo-epoch state, x_j, are defined at time t_j as

$$x(t_j) = \Phi_x(t_j, t_0)x_j + \Phi_c(t_j, t_0)c \tag{B.124}$$

or equivalently,

$$x_j = \Phi_x^{-1}(t_j, t_0)[x(t_j) - \Phi_c(t_j, t_0)c] \tag{B.125}$$

where $\Phi_x(t_j, t_0)$ and $\Phi_c(t_j, t_0)$ are the state and consider transition matrices referenced to the epoch time t_0, respectively. If there are no process noise parameters, the x_j is the satellite state at the epoch time t_0 and the pseudo-epoch state estimate becomes the epoch state estimate associated with the classical batch filter.

The pseudo-epoch state formulation is essentially a coordinate transformation of the current state that simplifies the propagation of the state from one batch to the next. The equations for propagating the pseudo-epoch state from one time to the next are given by [24]:

$$\begin{bmatrix} x \\ p \\ c \end{bmatrix}_{j+1} = \begin{bmatrix} I_x & \Phi_p(j) & 0 \\ 0 & M_j & 0 \\ 0 & 0 & I_y \end{bmatrix} \begin{bmatrix} x \\ p \\ c \end{bmatrix}_j + \begin{bmatrix} 0 \\ w \\ 0 \end{bmatrix}_j . \tag{B.126}$$

The time update given by Equation B.126 consists of a deterministic update associated with $\Phi_p(j)$ and a stochastic update associated with M_j. Note that this formulation results in most of the mapping matrix populated with ones and zeros since the transition matrix associated with the state is now the identity matrix.

Appendix C

Study of Numerical Methods

C.1 Iteration scheme for Hermite Interpolation

Table C.1: Hermite Interpolation using Iterations

	RMS of Residual [mm/s]		
No. of Iterations	Central Diff	Smoothing Splines	SG Filter
Zero Iterations	1358	0.5995	0.4977
5	1017	0.6422	2.462
10	761.8	0.7188	3.412
50	7.532	1.258	1.875
100	4.567	1.252	1.874
250	1.874	1.258	1.874
500	1.874	1.258	1.874
1000	1.595	1.258	1.874

C.2 Optimal Scale Factor for Cubic Smoothing Splines

Table C.2: Optimal Scale Factor for Smoothing Parameter

Scale Factor	RMS of Position [mm]	RMS of Velocity [mm/s]
10	0.132349×10^{-3}	0.5694178169
40	0.264893×10^{-3}	0.5694177566
60	0.324536×10^{-3}	0.5694177295
100	0.418839×10^{-3}	0.5694176866
150	0.513161×10^{-3}	0.5694176436
200	0.591956×10^{-3}	0.5694176083

C.3 Time Window Selection for CRN Filter

Table C.3: CRN Filter Results

Number of Coefficients	Time Window [sec]	RMS of Velocity [mm/s]
30	1800	3.4583
45	2700	0.5676
60	3600	0.5634
75	4500	0.5618
85	5100	0.4947
90	5400	0.3795
95	5700	0.3738
100	6000	0.3771
120	7200	0.3907

Appendix D

Quality Assessment of GPS Data

D.1 IGS Satellite Ephemerides

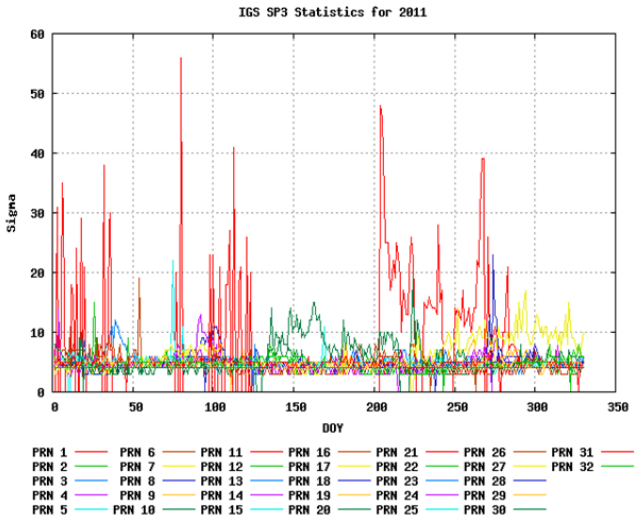

Figure D.1: GPS Satellite Sigmas from IGS Solution

D.2 GDOP Analysis

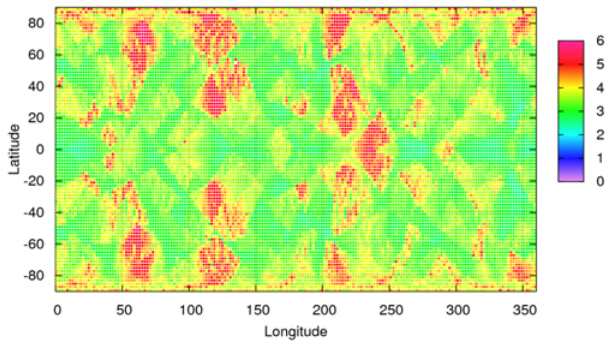

Figure D.2: Monthly GDOP Map Based on Satellite Position

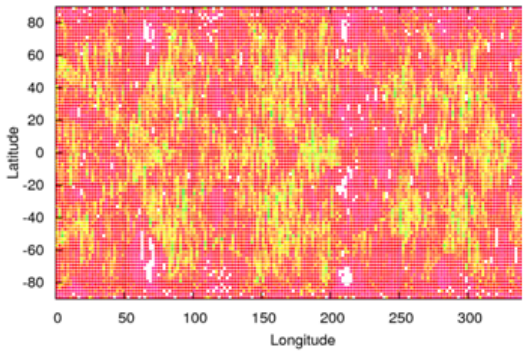

Figure D.3: Monthly GDOP Map from DDOBS

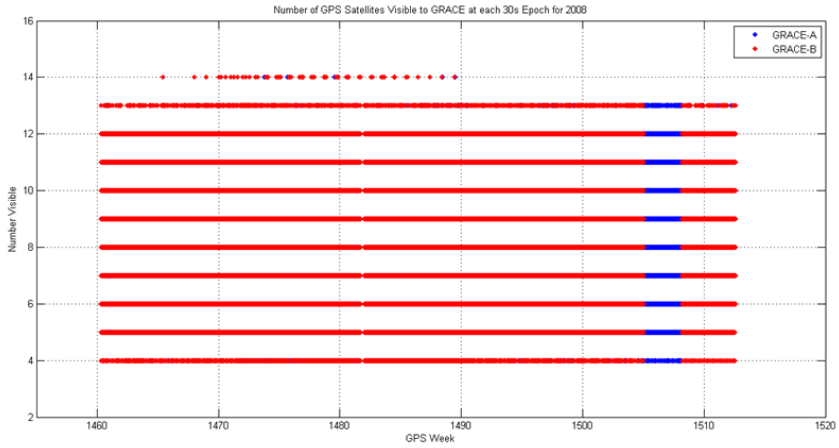

Figure D.4: GPS Satellite Visibility based on Satellite Position for One Month

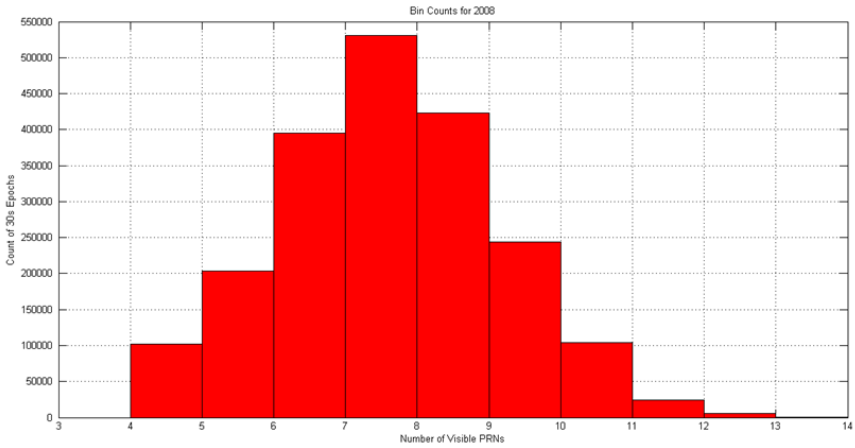

Figure D.5: Visible GPS Satellite Histogram for One Month

Appendix E

Filtered KBR Range-Rate Residuals

Note that the range-rate results can be filtered by fitting it to a mixed polynomial, sinusoidal function. This function has the form:

$$y = A\cos U + B\sin U + C + Dt + \frac{1}{2}Qt^2 + \frac{1}{6}Rt^3 + Et\cos U + Ft\sin U. \quad \text{(E.1)}$$

This curve fit model is subtracted from the range-rate residuals in order to account for the least squares solution.

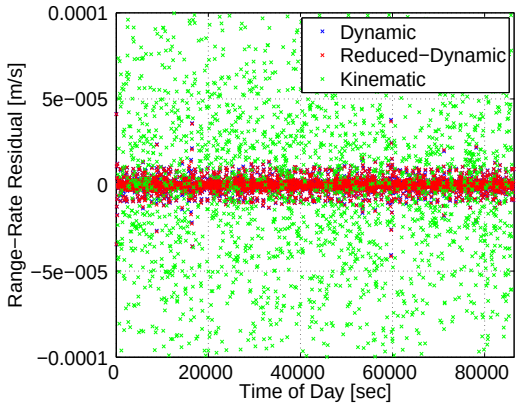

Figure E.1: Filtered KBR Range-Rate Residuals - 30 second Case

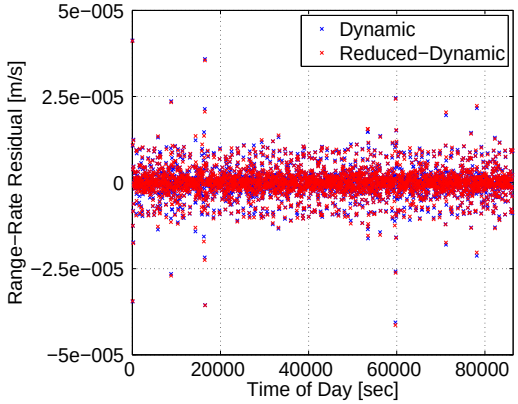

Figure E.2: Filtered KBR Range-Rate Residuals (Zoomed In) - 30 second Case

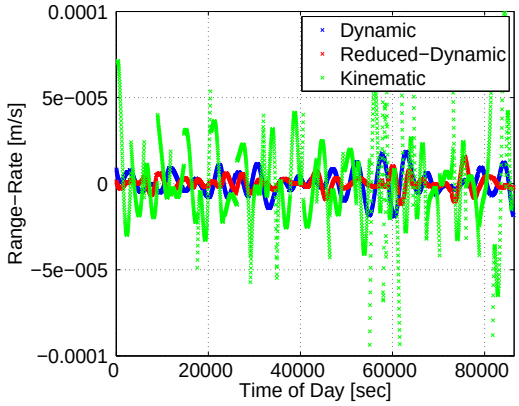

Figure E.3: KBR Range-Rate Filter Model - 30 second Case

Bibliography

[1] Tapley, B., Schutz, B., and Born, G., *Statistical Orbit Determination*, Elsevier Academic Press, 2004.

[2] Melbourne, W., Davis, E., Yunck, T., and Tapley, B., "The GPS flight experiment on TOPEX/POSEIDON," *Journal of Geophysical Research*, Vol. 21, No. 19, Sept. 1994, pp. 2171–2174.

[3] Rim, H. and Schutz, B., "Geoscience Laser Altimeter System (GLAS) Precise Orbit Determination (POD)," Algorithm Theoretical Basis Document v 2.2, Center for Space Research, The University of Texas at Austin, Oct. 2002.

[4] Zumberge, J., Heflin, M., Jefferson, D., Watkins, M., and Webb, F., "Precise point positioning for the efficient and robust analysis of GPS data from large networks," *Journal of Geophysical Research*, Vol. 102, No. B3, March 1997, pp. 5005–5017.

[5] Bertiger, W., Bar-Sever, Y., Christensen, E., Davis, E., Guinn, J., Haines, B., Ibanez-Meier, R., Jee, J., Lichten, S., Melbourne, W. G., Muellerschoen, R., Munson, T., Vigue, Y., Wu, S., Yunck, T., Schutz, B., Abusali, P., Rim, H., Watkins, M., and Willis, P., "GPS precise tracking of TOPEX/POSEIDON:

Results and implications," *Journal of Geophysical a priori*, Vol. 99, No. C12, Dec. 1994, pp. 449–464.

[6] Lerch, F., Klosko, S., and Patel, G., "A Geopotential Model from Satellite Tracking, Altimeter and Surface Gravity Data: GEMT3," *Journal of Geophysical Research*, Vol. 99, No. B2, Sept. 1994, pp. 2815–2839.

[7] Tapley, B., Shum, C., Ries, J., Poole, S., Abusali, P., Eanes, R., Kim, M., Rim, H., and Schutz, B., "The TEG-3 Earth Geopotential Model," *Gravity Geoid and Marine Geodesy*, edited by J. Seagwa, H. Fujimoto, and S. Okubo, Vol. 117, International Association of Geodesy Symposia, Springer Verlag, Tokyo, Japan, 1996, pp. 453–460.

[8] Kim, J., *Simulation Study of A Low-Low Satellite-to-Satellite Tracking Mission*, Ph.D. thesis, The University of Texas at Austin, Department of Aerospace Engineering and Engineering Mechanics, May 2000.

[9] Balmino, G., "The GOCE dedicated gravity mission: expectation and preparation," *Journees Luxembourgeoises de Geodynamique*, Vol. JLG89, European Center for Geodynamics and Seismology, 2001.

[10] Dunn, C., Bertiger, W., Bar-Sever, Y., Desai, S., Haines, B., Kuang, D., Franklin, G., Harris, I., Kruizinga, G., Meehan, T., Nandi, S., Nguyen, D., Rogstad, T., Thomas, J. B., Tien, J., Romans, L., Watkins, M., Wu, S., Bettadpur, S., and Kim, J., "Instruments of GRACE: GPS Augments Gravity Measurements," *GPS World*, Vol. 14, No. 2, Feb. 2003,

pp. 16–28, http://www.csr.utexas.edu/grace/publications/press/03-02-01-GRACE_gpsworld.pdf Accessed: May 2012.

[11] Tapley, B., Bettadpur, S., Ries, J., Thompson, P., and Watkins, M., "GRACE Measurements of Mass Variability in the Earth System," *Science*, Vol. 305, No. 5683, 2004, pp. 503–505.

[12] Stanton, R., *Gravity Recovery and Climate Experiment Science and Mission Requirements Document*, Jet Propulsion Laboratory, Aug. 2000.

[13] Visser, P., "Gravity field determination with GOCE and GRACE," *Advances in Space Research*, Vol. 23, No. 4, 1999, pp. 771 – 776.

[14] Gerlach, C., Foldvary, L., Svehla, D., Gruber, T., Wermuth, M., Sneeuw, N., Frommknecht, B., Oberndorfer, H., Peters, T., Rothacher, M., Rummel, R., and Steigenberger, P., "A CHAMP-only gravity field model from kinematic orbits using the energy integral," *Geophysical Research Letters*, Vol. 30, No. 20, Oct. 2003.

[15] Reubelt, T., Sneeuw, N., and Grafarend, E., "Comparison of Kinematic Orbit Analysis Methods for Gravity Field Recovery," *Hotine-Marussi Symposium on Mathematical Geodesy*, Vol. 137 of *International Association of Geodesy Symposia*, Springer Berlin Heidelberg, 2012, pp. 259–265.

[16] Austen, G. and Grafarend, E., "Gravitational field recovery from GRACE data of type high-low and low-low SST," *Advances in Geosciences*, 2005.

[17] Foldvary, L., "Spectral analysis of CHAMP kinematic velocities determined by applying smoothing cubic splines," *Periodica Polytechnica Civil Engineering*, Vol. 52, No. 1, 2008, pp. 29.

[18] Kang, Z., Tapley, B., Bettadpur, S., Ries, J., Nagel, P., and Pastor, R., "Precise orbit determination for the GRACE mission using only GPS data," *Journal of Geodesy*, Vol. 80, No. 6, July 2006, pp. 322–331.

[19] Bettadpur, S., "Gravity Recovery and Climate Experiment UT/CSR Level-2 Processing Standards," Tech. rep., May 2012, Rev 4.0 `ftp://podaac.jpl.nasa.gov/allData/grace/docs/L2-CSR0005_ProcStd_v4.0.pdf` Accessed: Aug. 2012.

[20] Webb, C., *Radiation Force Modeling for ICESat Precision Orbit Determination*, Ph.D. thesis, The University of Texas at Austin, Department of Aerospace Engineering and Engineering Mechanics, May 2007.

[21] Rim, H., Webb, C., and Schutz, B., "Effect of GPS Orbit Errors on ICESat Precision Orbit Determination," *Proceedings of AIAA/AAS Astrodynamics Specialist Conference*, AIAA, Denver, Colorado, Aug. 2000.

[22] Choi, K., *Jason-1 Precise Orbit Determination Using GPS Combined with SLR and DORIS Tracking Data*, Ph.D. thesis, The University of Texas at Austin, Department of Aerospace Engineering and Engineering Mechanics, Dec. 2003.

[23] Rim, H., Davis, G., and Schutz, B., "Dynamic orbit determination for the EOS laser altimeter satellite (EOS ALT/GLAS) using GPS measurements," *Astronautical Sciences*, Vol. 44, No. 3, 1993, pp. 409–424.

[24] Davis, G., *GPS-Based Precision Orbit Determination for Low Altitude Geodetic Satellites*, Ph.D. thesis, The University of Texas at Austin, Department of Aerospace Engineering and Engineering Mechanics, Aug. 1996.

[25] Bertiger, W., Desai, S., Haines, B., Harvey, N., Moore, A., Owen, S., and Weiss, J., "Single receiver phase ambiguity resolution with GPS data," *Journal of Geodesy*, Vol. 84, No. 5, May 2010, pp. 327–337.

[26] Watkins, M. and Yuan, D., "Gravity Recovery and Climate Experiment JPL Level-2 Processing Standards For Level-2 Product Release 05," Tech. Rep. Rev 5.0, Jet Propulsion Laboratory, March 2012, `ftp://podaac.jpl.nasa.gov/allData/grace/docs/L2-JPL_ProcStds_v5.pdf` Accessed: Aug. 2012.

[27] Bock, H., Beutler, G., Springer, T., and Rothacher, M., "Processing aspects related to permanent GPS arrays," *Earth Planets Space*, Vol. 52, May 2000, pp. 657–662.

[28] Bock, H., Hugentobler, U., Springer, T., and Beutler, G., "Efficient precise orbit determination of LEO satellites using GPS," *Advances in Space Research*, Vol. 30, No. 2, 2002, pp. 295–300.

[29] Ditmar, P., Kuznetsov, V., van Eck van der Slujs, A., Schrama, E., and Klees, R., "DEOS CHAMP-01C 70: a model of the Earth's gravity field computed from accelerations of the CHAMP satellite," *Journal of Geodesy*, Vol. 79, No. 19, Dec. 2005, pp. 586–601.

[30] Svehla, D. and Rothacher, M., "Kinematic Precise Orbit Determination for Gravity Field Determination," *A Window on the Future of Geodesy*, Vol. 128 of *International Association of Geodesy Symposia*, Springer Berlin Heidelberg, 2005, pp. 181–188.

[31] Liu, X., *Global gravity field recovery from satellite-to-satellite tracking data*, Ph.D. thesis, Delft University of Technology, 2008.

[32] Foldvary, L., "Analysis of numerical differentiation methods applied for determination of kinematic velocities for LEOs," *Periodica Polytechnica Civil Engineering*, Vol. 51, No. 1, 2007, pp. 17–24.

[33] Seago, J., *Orbit Accuracy and Quality Assessment Techniques for the ERS-1 Altimetric Satellite*, Ph.D. thesis, The University of Texas at Austin, Department of Aerospace Engineering and Engineering Mechanics, Dec. 1997.

[34] Press, W., Teukolsky, S., Vetterling, W., and Flannery, B., *Numerical Recipes 3rd Edition: The Art of Scientific Computing*, Cambridge University Press, 2007.

[35] Reubelt, T., Goetzelmann, M., and Grafarend, E. W., "Harmonic Analysis of the Earths Gravitational Field from Kinematic CHAMP Orbits based on Numerically Derived Satellite Accelerations," *Observation of the Earth System from Space*, Springer Berlin Heidelberg, 2006, pp. 27–42.

[36] Boor, C. D., *A Practical Guide to Splines*, Springer, 2001.

[37] Thomas, J., "An Analysis of Gravity-Field Estimation Based on Intersatellite Dual-1-Way Biased Ranging," Publication 98-15, Jet Propulsion Laboratory, May 1999.

[38] National Coordination Office for Space-Based Positioning, N. and Timing, "GPS Image Library," `http://www.gps.gov/multimedia/images/constellation.gif`, Accessed: May 2012.

[39] Misra, P. and Enge, P., *Global Positioning System: Signals, Measurements and Performance*, Ganga-Jamuna Press, 2001.

[40] Dow, J., Neilan, R., and Rizos, C., "The International GNSS Service in a changing landscape of Global Navigation Satellite Systems," *Journal of Geodesy*, Vol. 83, No. 3-4, Jan. 2009, pp. 191–198.

[41] Moyer, T., "Transformation from proper time on Earth to coordinate time in solar system barycentric space-time frame of reference," *Celestial Mechanics and Dynamical Astronomy*, Vol. 23, 1981, pp. 33–56.

[42] Petit, G. and Luzum, B., "IERS Technical Note No.36, IERS Conventions," Tech. rep., International Earth Rotation and Reference Systems Service, Frankfurt, Germany, 2010.

[43] Vallado, D., *Fundamentals of Astrodynamics and Applications*, Microcosm Press/Springer, 2nd ed., 2007.

[44] Standish, E., "JPL Planetary and Lunar Ephemerides DE405/LE405," Interoffice memorandum 312.f-98-408, Jet Propulsion Laboratory, Aug. 1998, `http://iau-comm4.jpl.nasa.gov/de405iom/de405iom.pdf` Accessed: May 2012.

[45] Gelb, A., *Applied Optimal Estimation*, The MIT Press, 1974.